論文 / 著書情報
Article / Book Information

題目(和文)	
Title(English)	Study of Waveguide Slot Array Antennas in Non-far Region Transmission
著者(和文)	RUCKKWAENTuchjuta
Author(English)	Tuchjuta Ruckkwaen
出典(和文)	学位:博士(学術), 学位授与機関:東京工業大学, 報告番号:甲第11839号, 授与年月日:2022年3月26日, 学位の種別:課程博士, 審査員:廣川 二郎,阪口 啓,西方 敦博,青柳 貴洋,TRAN GIA KHANH,長敬三
Citation(English)	Degree:Doctor (Academic), Conferring organization: Tokyo Institute of Technology, Report number:甲第11839号, Conferred date:2022/3/26, Degree Type:Course doctor, Examiner:,,,,,
学位種別(和文)	博士論文
Type(English)	Doctoral Thesis

Doctoral Dissertation

Study of Waveguide Slot Array Antennas in Non-far Region Transmission

January 2022

Presented by
Ruckkwaen Tuchjuta

Under supervision of
Professor Hirokawa Jiro

Department of Electrical and Electronic Engineering
Tokyo Institute of Technology

Acknowledgements

I would like to express my sincere gratitude to Prof. Jiro Hirokawa and Asst. Prof. Takashi Tomura for their continued guidance and support not only in academic but also in daily life since I enrolled in the master's program. Without their help I would not have been able to perform well while living in Japan.

I would like to thank Prof. Kei Sakaguchi, Prof. Atsuhiro Nishikata, Prof. Takahiro Aoyagi, Prof. Keizo Cho, and Assoc. Prof. Gia Khanh Tran for their constructive comments toward this dissertation. Their valuable comments help elevate the content of this dissertation significantly.

I am also very grateful to Prof. Makoto Ando for giving me this wonderful opportunity to study here at Tokyo Tech. Although it was only less than 2 years under your supervision, I had learned a lot of scientific and engineering aspects. I would like to thank both past and current lab members who are always willing to extend their helping hands. My special thanks go to Mr. Keisuke Ejiri and Mr. Masahiro Wakasa for their earnest support during several experiments.

Once again I would like to express my utmost gratitude for all the members of Ando and Hirokawa Lab for creating a hospitable and comfortable environment in the lab which allow me to enjoy a fulfilling student life. Lastly, I would like to thank my family and friends for their supporting and encouraging me even when we have been far apart.

Contents

Chapter 1

Introduction

1.1 Waveguide Slot Antennas

Waveguide slot antennas have been investigated in various applications ranging from wireless body area network (WBAN) [1], [2], multiple-input multiple-output (MIMO) system [3], [4], [5], [6], satellite communication (SATCOM) [7], radar systems [8], [9], radio-frequency identification (RFID) reader [6], and etc., because of its low-loss, robustness, low-profile, and size miniaturization at high frequencies. In addition, the high-power capability of waveguide slot antennas attracts their usage in wireless power transmission (WPT) and high-power microwave (HPM) applications [10].

Fig. 1.1 shows examples of waveguide slot antennas developed for similar applications at Tokyo Tech [11]:

1. (a) radial line slot antenna (RLSA) for direct broadcast from a satellite (DBS) [12].
2. (b) alternating-phase-feed single-mode waveguide slot array antenna for fixed wireless access (FWA) system [13].
3. (c) parallel-plate slot array antenna for synthetic aperture radar (SAR) [14].
4. (d) post-wall waveguide slot array antenna for millimeter wave applications [15].
5. (e) plate-laminated hollow-waveguide slot array antenna for millimeter wave applications [16].

The aforementioned works investigated mainly the far-field applications, at which the target distances are approximately larger than $\frac{2D^2}{\lambda}$, where D is the largest dimension of the antenna and λ is the free space wavelength. In this study, however, we are interested in the applications in non-far region in which some interesting features can be utilized.

1.2 Non-far Region Applications

In near-field region, electromagnetic field does not fall off as $1/r$ where r is the propagation distance from a radiating element in consideration. Arranging radiating elements of a waveguide slot antenna in array configuration and exciting them in a certain fashion can control antenna directivity which indicates sharpness of an antenna beam. A common technique utilized in non-far region applications is near-field focusing. Near-field focusing is a well-known technique which focuses electromagnetic field at a point in the antenna near-field region to increase the electromagnetic power density in a size-limited region close to the antenna aperture [17]. Such a technique has been adopted in various applications such as electromagnetic imaging, radio frequency identification, and etc. Fig. 1.2 shows a slotted waveguide sparse array antenna proposed by [18] for near-field focusing applications. In [18], array configuration (the excited magnetic current and position of each slot) was determined using the particle swarm optimization (PSO) to achieve the desired near-field pattern. In the same manner, in WPT A same concept as the near-field focusing so called the beam-typed technique has been used, in which the divergence of the beam is limited and focused the radiating energy on the receiving antenna (rectanna) to realize a high transmission efficiency [19]. In fact, the study [20] suggests that the Gaussian beam is required to achieve approximately 100% transmission efficiency. One of the very first demonstration using this technique was done in [21] where the microwave beam was used to power and position a helicopter. One common feature related to the near-field focusing is the quasi-plane behavior in the near-field region; this allows the potential for stable wireless communication links [22]. Similarly, [23] utilizes the quasi-plane wave to conduct small antenna pattern measurements. In addition, the antenna in [24] was proposed for to set up a stable, high data-rate ultra-short-range 3×3 multiple-input multiple-output (MIMO) wireless communication link using such a feature. Another example that shows an aspect retaining in the electromagnetic near-field is

the orbital angular momentum (OAM) multiplexing; the OAM modes are efficiently transmitted within short distances while these mode cannot be maintained in the far-field region owing to the divergence of the beam [25].It should be emphasized that transmission in near-field applications is line-of-sight propagation. The multi-path effect from the surroundings is negligible in the near-field region because the transmitted energy is normally concentrated in the volume over the radiating surface of an antenna. In such a scenario shadowing effects are a dominant cause of degradation over multi-path effects [26]. In addition, multiple reflections between the Tx and Rx antennas might become a serious issue in a certain scenario. In particular, if the distance between Tx and Rx antennas is very short and the size of the Rx antenna is comparable to that of the Tx antenna, the effect of multiple reflections will be large. In some applications such as WPT [27], they might pose a problem. The complete suppression of multiple reflections between the Tx and Rx is difficult. They however can be alleviated to a certain extent, see [28].

Near-field transmission can be classified by their applications into two major categories: 1) wireless data communication and 2) wireless power transfer. The following are some of the works developed at Tokyo Tech for non-far region applications.

- **wireless data communication** : Fig. 1.3 shows an illustration of A 60 GHz-band compact-range gigabit Wireless access system developed in [22]. A large array antenna was adopted in the system to realize a stable communication zone in the non-far region of the array. As mentioned previously, a dominant cause of degradation which is common in most of near-field applications is shadowing effects. However it will be pointed out in the next chapter that the multi-path effect from the size of the large array antenna of the a compact-range system similar to that in [22] contribute to significant level of intersymbol interference (ISI) especially at the distances close to the array. The studies [29], [30] demonstrates a potential system for high speed data communication in non-far region. Fig. 1.4 show an illustration of a rectangular orthogonal multiplexing (ROM) antenna system. Four orthogonal modes can be transmitted and received simultaneously. Each mode is generated by controlling the array phase excitation owing to monopulse circuits. The demonstrations confirmed the possibility of mode multiplexing; Therefore, channel capacity can be increased in such a system. The

efficiency of ROM transmission is limited by the collapse of the orthogonal modes due to the beam divergence. In other words, the quality of each mode can be efficiently maintained in the non-far region of the Tx antenna.

- **wireless power transfer** : An example of an antenna system for short-distance wireless power transfer is given in [31]. The study proposed a novel 8-port microstrip fed RLSA as a receiving (RX) antenna. The antenna was design based on the characteristics of the RF-to-dc conversion circuit to which high conversion efficiency is achieved by a certain amount of the input RF power. This amount of the input RF power is lower than the total receiving power at the RX antenna; this lead to the design of 8-port way divider using the microstrip line structure. The transmission scheme is given in Fig. 1.5. The Tx antenna is a one-port RLSA which will be discussed in detailed in chapter 3. Based on the beam-typed technique, the transmission distance is in the near-field region of the Tx antenna to concentrate the radiating energy within the beam to the Rx antenna. The Rx antenna was fabricated by print circuit board (PCB) technology without the need of an additional metal encasement; This results in a light-weighted antenna which is suitable for installing in electric vehicles (EV)

It should be emphasized that the amplitude and phase excitation control of an array is crucial especially for non-far region applications as some of examples was already given in [17], [18] and will be emphasized again in chapter 3. On the contrary, the amplitude and phase excitation control for far-field region applications is not so sensitive as that for non-far region applications. Precisely speaking, a desired field pattern or characteristics in the near-field region is more susceptible to any deviation from the ideal antenna field excitation while a desired field pattern in the far-field region is likely to be less effected due the divergence of the propagating electromagnetic field. To this end, the maximum transmission distance and transmission efficiency of both near field wireless communication and WPT systems is generally limited by the beam divergence. A straightforward way to enhance the maximum transmission distance as well as transmission efficiency is to increase the transmitting antenna size. In near-field communication systems, a signal processing technique could be an alternative to improve the maximum transmission distance without enlarging the antenna size. On the contrary,

only applying a signal processing technique to a WPT system would not efficiently improve the maximum distance or transmission efficiency. Though increasing the transmitting power might be able to increase the maximum transmission distance, it does not contribute to any improvement in transmission efficiency.

Other types of antennas which are widely adopted in non-far region applications are reflector antennas and microstrip antennas. Reflector antennas among other antenna configurations provide the highest gain, widest bandwidth. The primary role of a reflector antenna is to confine or radiate most of the electromagnetic energy over its aperture into a focal plane or far field for communication or energy transfer [32]. Therefore, reflector antennas are often found their applications in near-field focusing [33] and WPT [21] since beam/energy focusing can be efficiently synthesized by this type of antenna. One of their disadvantages however is their bulkiness which makes reflector antennas not popular in short-range wireless communications. On the other hand, microstrip antennas are comparatively lightweight, miniature, and easy to integrate with chip devices. As a result, microstrip antennas have been adopted in several short-range wireless communication systems. Since microstrip antennas have higher loss and lower power capability compared to waveguide slot antennas or reflector antennas, their usage on WPT tends to be for small power consumption devices [34]. In the comparative point of view, one could say that waveguide slot antennas are a trade-off between reflector antennas and microstrip antenna.

1.3 Outlines of this Study

The objective of this dissertation is investigate candidate antennas and possibilities for their improvements as well as the performance evaluation for these applications. Our objectives is to study transmission issues for a given antenna system. Precisely speaking, our aim is to quantitatively estimate bit error rate (BER) as well as intersymbol interference (ISI) given a compact range communication using a large array antenna which is presented in chapter 2. The main degradation issue of this system is BER degradation due to ISI in the proximity of the Tx antenna and the direct measurement of BER is troublesome and time-consuming; Therefore, we initiate a method to evaluate ISI which leads to BER using only the measured aperture field distribution of an actual antenna. As for the short range WPT systems

discussed in chapter 3 and 4, our objective is to improve the transmission level and reduce transmission ripples. One of the issues in short range WPT application is the transmission ripples which result in the fluctuation in the transmission efficiency; the main cause of the transmission ripples is multiple reflection between Tx and Rx antennas. Furthermore, the reduction in transmission efficiency is attributable to the performance of the design antenna excitation. We improve the transmission by using a better feeding design which can realize better antenna aperture excitation. The flow chart in Fig. 1.6 shows the summary of this dissertation. It is mainly divided into two part based on their applications.

Chapter 2 discusses the BER issue in a 60 GHz-band compact-range gigabit wireless access system using large array antennas [22]. The ISI mechanism which is the main cause of the BER degradation from the adoption of a large array antenna is indicated and the method to quantitatively estimate ISI using the antenna near-field distribution was proposed. The validity of the proposed method was confirmed experimentally.

Chapter 3 deals with the transmission between RLSAs in short distance [27]. The simulation result indicates large transmission ripples caused by multiple reflections between the transmitting (Tx) and the receiving (Rx) antennas, which is not a desired quality for WPT applications. The aim is to enhance the transmission and reduce the transmission ripples by improving the uniformity in the aperture field excitation. The dog-bone cross-slot was adopted for such a purpose. The design of the dog-bone cross-slot using the eigenmode analysis is given. The improvement of the transmission using the design antennas was verified by simulation and experiment.

Chapter 4 proposed a circular-polarized parallel-plate slot array antenna as a promising candidate for wireless communication and WPT applications. The target is to design a candidate antenna for short-range transmission applications which has a better transmission performance, i.e. transmission efficiency and its characteristics up to a distance of 30 cm. The design of the whole antenna structure using electromagnetic simulator software HFSS is given. The antenna fabrication is detailed. Finally, the performances of the design antenna were confirmed by simulation.

Chapter 5 summarizes the results of this study and the future considerations and improvements are pointed out.

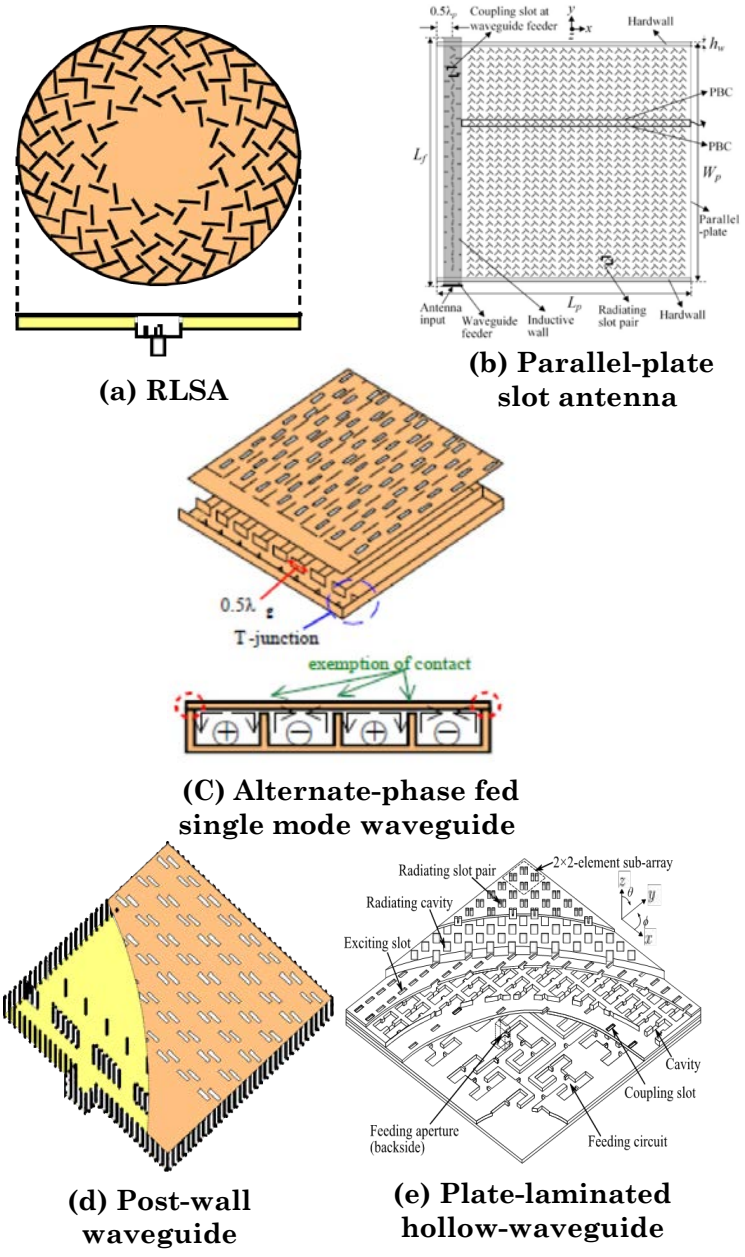

(a) RLSA

(b) Parallel-plate slot antenna

(C) Alternate-phase fed single mode waveguide

(d) Post-wall waveguide

(e) Plate-laminated hollow-waveguide

Figure 1.1: Waveguide slot antennas

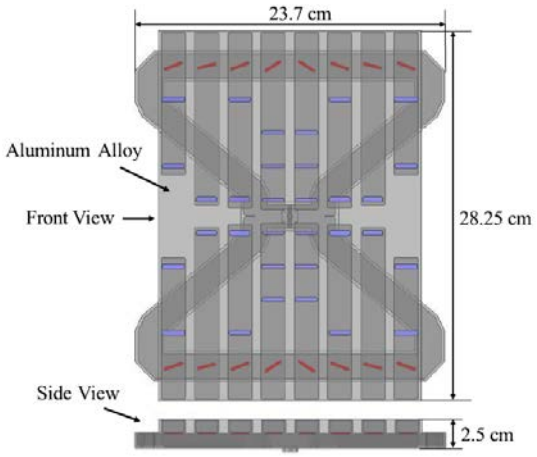

Figure 1.2: Slot waveguide array antenna for near-field focusing

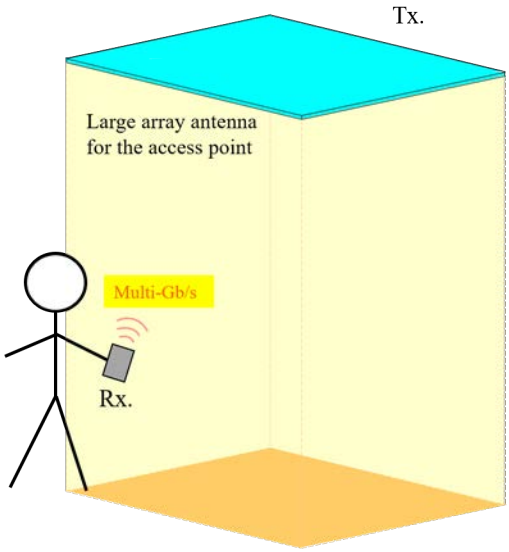

Figure 1.3: Compact range communication system

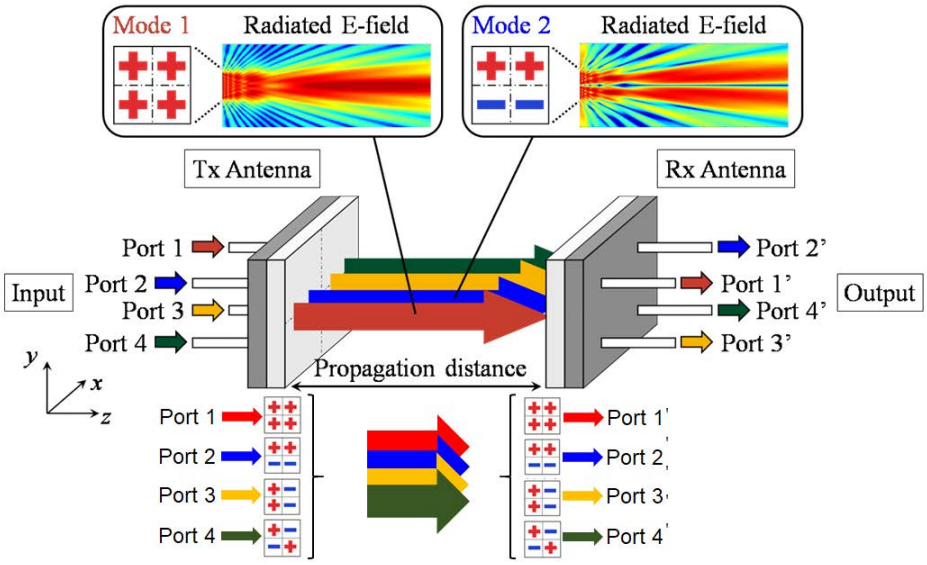

Figure 1.4: Rectangular orthogonal mode transmission system

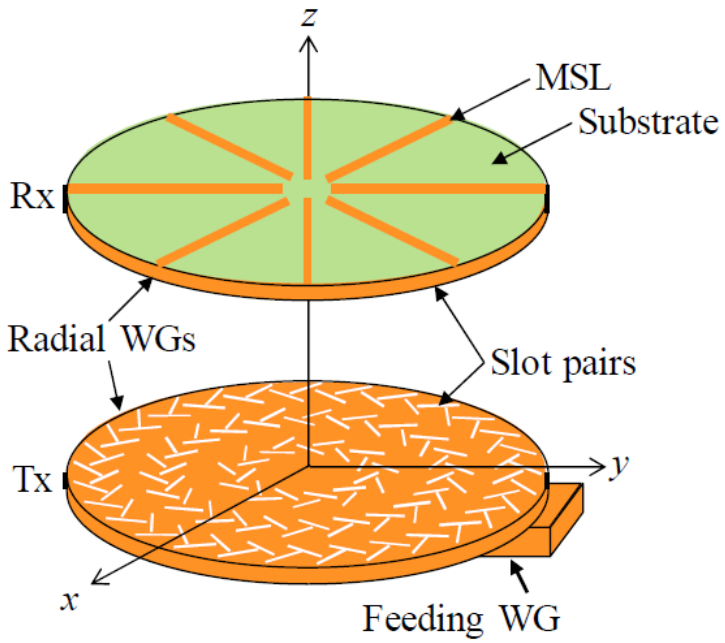

Figure 1.5: Wireless power transfer using RLSAs

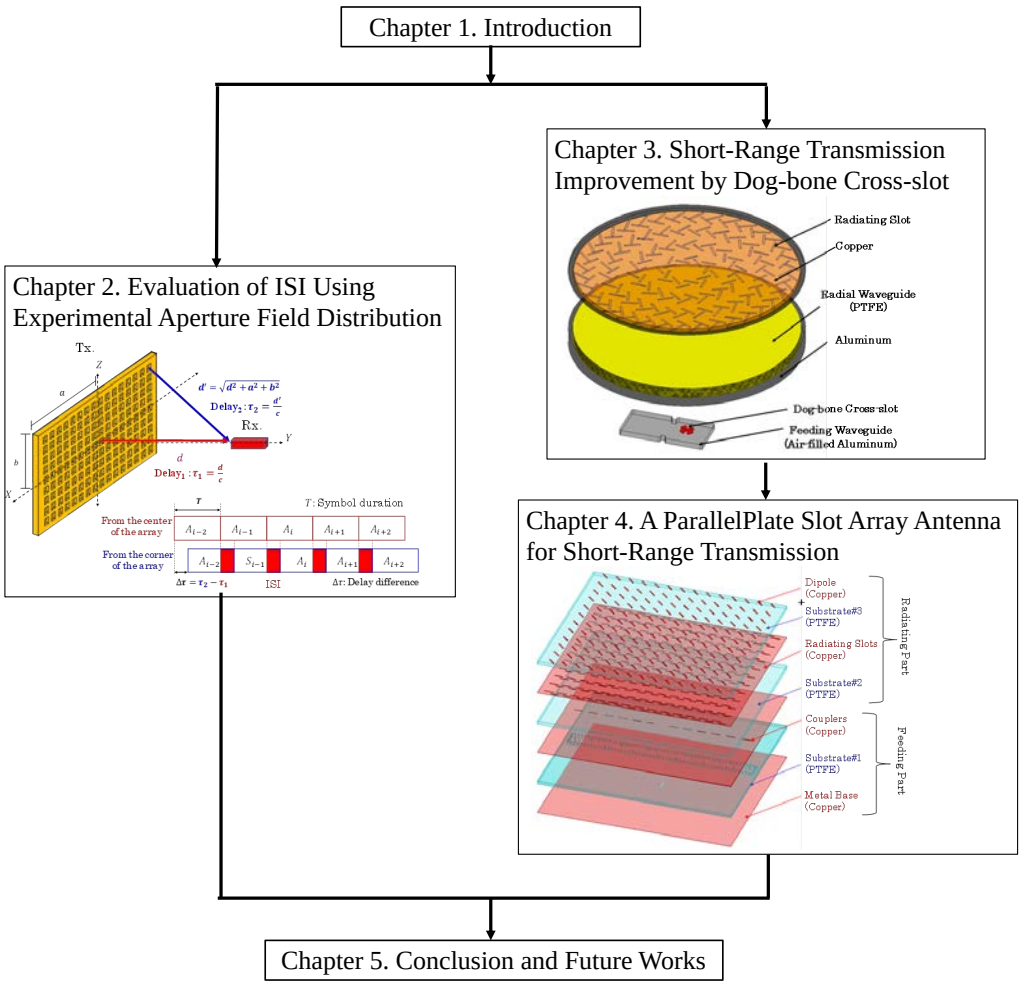

Figure 1.6: Flow chart of this dissertation

References

[1] K. Wong, H. Chang, C. Wang, and S. Wang, "Very-low-profile grounded coplanar waveguide-fed dual-band wlan slot antenna for on-body antenna application," *IEEE Antennas and Wireless Propagation Letters*, vol. 19, no. 1, pp. 213–217, Jan. 2020.

[2] Y. Hong, J. Tak, and J. Choi, "An all-textile siw cavity-backed circular ring-slot antenna for wban applications," *IEEE Antennas and Wireless Propagation Letters*, vol. 15, pp. 1995–1999, Apr. 2016.

[3] T. Li, H. Meng, and W. Dou, "Design and implementation of dual-frequency dual-polarization slotted waveguide antenna array for ka-band application," *IEEE Antennas and Wireless Propagation Letters*, vol. 13, pp. 1317–1320, Jul. 2014.

[4] I. R. R. Barani, K. Wong, Y. Zhang, and W. Li, "Low-profile wideband conjoined open-slot antennas fed by grounded coplanar waveguides for 4×4 5g mimo operation," *IEEE Transactions on Antennas and Propagation*, vol. 68, no. 4, pp. 2646–2657, Apr. 2020.

[5] P. Gao, S. He, X. Wei, Z. Xu, N. Wang, and Y. Zheng, "Compact printed uwb diversity slot antenna with 5.5-ghz band-notched characteristics," *IEEE Antennas and Wireless Propagation Letters*, vol. 13, pp. 376–379, Feb. 2014.

[6] R. Cao and S. Yu, "Wideband compact cpw-fed circularly polarized antenna for universal uhf rfid reader," *IEEE Transactions on Antennas and Propagation*, vol. 63, no. 9, pp. 4148–4151, Jun. 2015.

[7] W. Yuan, X. Liang, L. Zhang, J. Geng, W. Zhu, and R. Jin, "Rectangular grating waveguide slot array antenna for satcom applications," *IEEE Transactions on Antennas and Propagation*, vol. 67, no. 6, pp. 3869–3880, Jun. 2019.

[8] F. Bauer and W. Menzel, "A 79-ghz resonant laminated waveguide slotted array antenna using novel shaped slots in ltcc," *IEEE Antennas and Wireless Propagation Letters*, vol. 12, pp. 296–299, Feb. 2013.

[9] N. Aboserwal, J. L. Salazar-Cerreno, and Z. Qamar, "An ultra-compact x-band dual-polarized slotted waveguide array unit cell for large e-scanning radar systems," *IEEE Access*, vol. 8, pp. 210 651–210 662, Nov. 2020.

[10] S. Peng, C. Yuan, T. Shu, J. Ju, and Q. Zhang, "Design of a concentric array radial line slot antenna for high-power microwave application," *IEEE Transactions on Plasma Science*, vol. 43, no. 10, pp. 3527–3529, Jan. 2015.

[11] X. Xu, "Study of Functional-Circuit Integration to Waveguide Slot Array Antennas in the Millimeter-Wave Band," Ph.D. dissertation, Department of Electrical and Electronic Engineering, Tokyo Institute of Technology, 2017.

[12] M. Ando, K. Sakurai, N. Goto, K. Arimura, and Y. Ito, "A radial line slot antenna for 12 ghz satellite tv reception," *IEEE Transactions on Antennas and Propagation*, vol. 13, no. 12, pp. 1347–1353, Dec. 1985.

[13] Y. Kimura, Y. Miura, T. Shirosaki, T. Taniguchi, Y. Kazama, J. Hirokawa, M. Ando, and T. Shirouzu, "A low-cost and very compact wireless terminal integrated on the back of a waveguide planar array for 26 ghz band fixed wireless access (fwa) systems," *IEEE Transactions on Antennas and Propagation*, vol. 53, no. 8, pp. 2456–2463, Aug. 2005.

[14] P. R. Akbar, H. Saito, M. Zhang, J. Hirokawa, and M. Ando, "Parallel-plate slot array antenna for deployable sar antenna onboard small satellite," *IEEE Transactions on Antennas and Propagation*, vol. 64, no. 5, pp. 1661–1671, May 2016.

[15] J. Hirokawa and M. Ando, "Single-layer feed waveguide consisting of posts for plane tem wave excitation in parallel plates," *IEEE Transactions on Antennas and Propagation*, vol. 46, no. 5, pp. 625–630, May 1998.

[16] T. Tomura, J. Hirokawa, T. Hirano, and M. Ando, "45° linearly polarized hollow-waveguide 16×16-slot array antenna covering 71–86 ghz band," *IEEE Transactions on Antennas and Propagation*, vol. 62, no. 10, pp. 5061–5067, Oct. 2014.

[17] Y. F. Wu, Y. J. Cheng, S. S. Yao, and Y. Fan, "Millimeter-wave near-field-focused full 2-d frequency scanning antenna array with height-modulated-ridge waveguide," *IEEE Transactions on Antennas and Propagation*, vol. 69, no. 5, pp. 2595–2604, May 2021.

[18] Y. Wu, B. Jiang, M. Zhang, J. Hirokawa, and Q. H. Liu, "A four-corner-fed slotted waveguide sparse array for near-field focusing," *IEEE Access*, vol. 8, pp. 203 048–203 057, Nov. 2020.

[19] W. C. Brown, "The history of wireless power transmission," *Solar Energy*, vol. 56, no. 1, pp. 3–21, Jan. 1996.

[20] G. Goubau and F. Schwering, "On the guided propagation of electromagnetic wave beams," *IRE Transactions Antennas and Propagation*, vol. 9, no. 3, pp. 248–256, May 1961.

[21] W. C. Brown, "Experiments involving a microwave beam to power and position a helicopter," *IEEE Transactions on Aerospace Electronic Systems*, vol. AES-5, no. 5, pp. 692–702, Sep. 1969.

[22] M. Zhang, K. Toyosaki, J. Hirokawa, M. Ando, T. Taniguchi, and M. Noda, "A 60 ghz-band compact-range gigabit wireless access system using large array antennas," *IEEE Transactions on Antennas and Propagation*, vol. 63, no. 8, pp. 3423–3440, Aug. 2015.

[23] K. Miyata, "A 12 ghz-band planar waveguide array antenna for compact range application-a preliminary study," *IEEE Transactions on Antennas and Propagation*, vol. 44, no. 4, pp. 588–589, Apr. 1996.

[24] S. Lemey, T. Castel, P. V. Torre, T. Vervust, J. Vanfleteren, P. Demeester, D. V. Ginste, and H. Rogier, "Threefold rotationally symmetric siw antenna array for ultra-short-range mimo communication," *IEEE Transactions on Antennas and Propagation*, vol. 64, no. 5, pp. 1689–1699, Feb. 2016.

[25] X. Xu, A. Mazzinghi, A. Freni, and J. Hirokawa, "Simultaneous generation of three oam modes by using a rlsa fed by a waveguide circuit for 60 ghz-band radiative near-field region oam multiplexing," *IEEE Transactions on Antennas and Propagation*, vol. 69, no. 3, pp. 1249–1259, Mar. 2021.

[26] M. Ali and M. Ando, "Fast estimation of shadowing effects in millimeter-wave short range communication by modified edge representation," *IEICE Transactions on Communications*, vol. E98-B, no. 9, pp. 1873–1881, Sep. 2015.

[27] T. Tomura, J. Hirokawa, M. Furukawa, and T. Fujiwara, "Radial line slot array antenna for 5.8-ghz-band beam-type wireless power transmission," *Proceedings of European Conference on Antennas and Propagation (EuCAP)*, T02-A10.2, Mar. 2020.

[28] T. Ruckkwaen, T. Tomura, and J. Hirokawa, "Short-range transmission improvement by dog-bone cross-slot feed in radial line slot antenna," *IEICE Communications Express*, To be published in Jun. 2022.

[29] K. Tekkouk, J. Hirokawa, and M. Ando, "Multiplexing antenna system in the non-far region exploiting two-dimensional beam mode orthogonality in the rectangular coordinate system," *IEEE Transactions on Antennas and Propagation*, vol. 66, no. 3, pp. 1507–1515, Mar. 2018.

[30] K. Wada, T. Tomura, and J. Hirokawa, "Dual-polarized 2-d beam mode orthogonal multiplexing antenna system for the non-far region," *IEEE Transactions on Antennas and Propagation*, vol. 68, no. 9, pp. 6614–6623, Sep. 2020.

[31] T. Tomura, J. Hirokawa, M. Furukawa, T. Fujiwara, and N. Shinohara, "Eight-port feed radial line slot antenna for wireless power transmission," *IEEE Open Journal of Antennas and Propagation*, vol. 2, pp. 170–180, Jan. 2021.

[32] Y. Rahmat-Samii and R. Haupt, "Reflector antenna developments: A perspective on the past, present and future," *IEEE Antennas and Propagation Magazine*, vol. 57, no. 2, pp. 85–95, Apr. 2015.

[33] H. T. Chou, "Near-field finite-zone focused radiation from reflector antenna with continuously tapered ellipsoidal surface curvatures," *IEEE Transactions on Antennas and Propagation*, vol. 67, no. 10, pp. 6344–6352, Oct. 2019.

[34] P. D. H. Re, S. K. Podilchak, S. A. Rotenberg, G. Goussetis, and J. Lee, "Circularly polarized retrodirective antenna array for wireless power transmission," *IEEE Transactions on Antennas and Propagation*, vol. 68, no. 4, pp. 2743–2752, Apr. 2020.

[35] H. Aissat, L. Cirio, M. Grzeskowiak, J. M. Laheurte, and O. Picon, "Reconfigurable circularly polarized antenna for short-range communication systems," *IEEE Transactions on Microwave Theory and Techniques*, vol. 54, no. 6, pp. 2856–2863, Jun. 2006.

[36] M. Zhang, M. Wakasa, K.Araki, J. Hirokawa, and M. Ando, "Analysis of intersymbol interference in a 60 ghz-band compact-range wireless access system using various large array antennas," *International Symposium on Antennas and Propagation (ISAP)*, S3.3.4, Nov. 2015.

[37] T. Ishikawa and N. Shinohara, "Flat-topped beam forming experiment for microwave power transfer system to a vehicle roof," *Wireless Power Transfer*, vol. 2, no. 1, pp. 15–21, Mar. 2015.

Chapter 2

Intersymbol Interference Evaluation in Non Far Region Transmission using a Large Array Antenna

2.1 Introductory Remarks

The compact range communication proposed in [1] is considered to be a promising candidate for high speed, short range communication systems. In the same context as general line of sight communication, the system suffers from shadowing effects. The adoption of a large array antenna offers important features, including multipath free from the transmission not obstructed by surroundings [1], [2], as channel conditions like fading, are not expected to be severe. Therefore, a single carrier system will be sufficient for a system. Table 2.1 give a quantitative comparison with a similar 60-GHz wireless communication system [3]. The system proposed in [3] utilized a smaller antenna for a far-field region application. Fig. 2.1 show plots of measured bit error rate (BER) performance versus transmission distances for various array sizes. The significant BER degradation can be observed at the distances close to the Tx antenna. In addition, BER degradation becomes even worse for lager array sizes. The findings in [4], [5] point out that the BER degradation is attributable to intersymbol interference (ISI). The main cause of ISI in [1] is path delay differences among the elements of an array antenna. Due to the

adoption of a large array antenna, this path delay difference is large. As a result, the ISI level value also becomes significant.

Reproducing and accurately predicting BER performance as shown in Fig. 2.1 would benefit the system planning. Though the prediction of BER is of utmost interest, the existence of several signal processing components, e.g., equalizer and automatic gain control (AGC), increases the complexity of the problem. To simplify the problem, we aim to evaluate ISI which is the dominant cause of the BER degradation while disregarding the signal processing components.

Estimating the ISI level is of vital importance in evaluating overall system performance. For this, the use of commercial electromagnetic simulation software is limited by memory storage issues due to the large size of the simulation model (in this case the antenna size). In addition, the direct measurement of ISI and related quantities is difficult because of many physical limitations, including cable length, measurement space, and others.

This chapter discuss an ISI estimation method based on the near field distribution of the array antenna as an alternative method to evaluate the ISI for different transmission distances. The method is more convenient than direct measurements as will be indicated in the following sections and also has certain advantages over electromagnetic software simulations as the obtained results closely represent the actual array excitation because the near field distribution demonstrates defects arising from antenna fabrication. These defects are, however, not easy to measure or predict, so reflecting these imperfections in the antenna modelling for simulation purpose is not practical.

Here, despite the ISI issue arising with a large array antenna, the utilization of equalizer and LDPC (low-density parity-check code) mitigates the interference issue and bit error rate lower than 10^{-12} can be achieved. However, the adoption of OFDM may increase the complexity of in both transmitting and receiving circuits and OFDM always suffers from PAPR (peak-to-average ratio) problem in transmitter amplifiers.

Overall in this Chapter, section 2.2 presents details of the non-far region communication system that is proposed. Here, an evaluation model is derived based on the scenario of the system and will be referred to during the rest of the chapter. In section 2.3, a definition of ISI and the equivalent baseband communication system, from which the ISI formula is derived, are given. The channel transfer function, which is vital to the ISI analysis, is indicated and will be investigated in detail in the following sections. Section

2.4 elaborates the ISI estimation method using the near-field distribution: each subsection presents steps in estimating the ISI. Section 2.5 interprets and validates the results obtained by the proposed method. A comparison to direct measurements is provided and discrepancies between the ISI estimated by our proposed method and estimated from direct measurements are discussed. At the end of the section, an application of the ISI in evaluating the signal to noise plus interference ratio (SINR) is given. Finally, we conclude with a discussion of the significance of the proposed method in section 2.6.

2.2 Non-Far Region Communication System

In the study here, we focus on the communication scenario shown in Fig. 2.2, Non-far region communication system. Table 2.1 provides the system specification though in the current study these signal processing components will not be taken into account. The main transceiver device adopts a large array antenna, within the near-field region of antenna. The transmitting (Tx) antenna is a large array antenna with uniform excitation design and the receiving (Rx) antenna is in a mobile terminal. The important feature of adopting a large array antenna is that it generates an approximately uniform volume (quasi-plane wave) over the cross section of the antenna in the non-far region. The rectangular volume forms the reception zone of this system. The distance from the Rx antenna to the Tx antenna is in the near-field region (shorter than D^2/λ, where D is the maximum dimension of the transmitting antenna and λ is the wavelength) [6]. A user within the reception zone experiences multi-gigabit data access. Fig. 2.3 demonstrates the criterion of the field region of an antenna in terms of wavelength (λ) and the maximum dimension of the antenna (D). Based on the foregoing criterion, the non-far (near-field) region is defined as the region from the antenna front up to R_2. while most of conventional wireless communication systems, however, operates in the far-field region.

Fig. 2.4 shows the evaluation model of the system in Fig. 2.2, in which the Tx antenna is placed at the origin of the rectangular coordinate system. The Rx antenna is represented by a waveguide probe. The coordinate system mentioned hereafter refers to the configuration in Fig. 2.4.

The actual system is proposed for a 60 GHz-band wireless system at 57-66 GHz. Unfortunately, however, the fabrication of the Tx antenna for the 60 GHz-band has not been successfully achieved at present. A 30 GHz-band

64x32-slot array antenna [7] is used for the Tx antenna with corporate feed structure as the feeding circuit. The band discussed in this paper is about a half of the 60 GHz-band. The antenna dimensions are 583.2×301.6 mm2, directivity 42 dBi, and the aperture efficiency 75%. A WR-28 waveguide probe is used for the Rx antenna.

It should be noted that the frequency scaling (from 60 GHz to 30 GHz) poses no issue of concern for the proposed method. This paper discusses the ISI in the RF band. From the theoretical point of view, the ISI analysis model and method, though frequency-dependent, are the same for all frequencies when the electrical size of the antenna is normalized by the wavelength.

2.3 Intersymbol Interference Analysis

Before dealing with ISI analysis, it is important that we should be familiar with a communication system model and its basic components. Fig. 2.5 demonstrates simple building blocks of a communication system. In particular, this section explains how the optimum filters (and $g_r(t)$) are designed in order to mitigate the effects of additive white noise and ISI. In subsection 2.3.1, we explain how to determine the filter which minimize the effect of additive white noise at the receiving end, namely Matched Filter and in subsection 2.3.2, we explain the interference-free condition and give an example of a widely-used filter which satisfies the condition.

2.3.1 Matched Filter

Let us assume in Fig. 2.5 that output signal just directly after Channel $h(t)$ and frequency response of the receiving filter are $s_h(t)$ and $G_r(f)$ respectively. The input to the receiving filter $r(t)$ and the output of the receiving filter $y(t)$ are given as follows,

$$r(t) = s_h(t) + w(t) \tag{2.1}$$

$$y(t) = s_0(t) + n(t). \tag{2.2}$$

Provided that $s_0(t)$ and $n(t)$ are the response of the receiving filter to the input signal $s_h(t)$ and the white Gaussian noise $w(t)$ respectively. Their

formulas are given below,

$$s_0(t) = \int_{-\infty}^{\infty} g(\tau) s_h(t-\tau)\, d\tau \tag{2.3}$$

$$s_0(t) = \int_{-\infty}^{\infty} G_r(f) S_h(f) \exp(j2\pi ft)\, df \tag{2.4}$$

$$n(t) = \int_{-\infty}^{\infty} g_r(\tau) w(t-\tau)\ \ d\tau \tag{2.5}$$

$$n(t) = \int_{-\infty}^{\infty} G_r(f) W(f) \exp(j2\pi ft)\, df. \tag{2.6}$$

Here, $S_h(f)$ and $W(f)$ are the Fourier transform of $s_h(t)$ and $w(t)$ respectively. The receiving signal power at arbitrary time instant t is expressed as $\mid s_0(t) \mid^2$ and average noise power is expressed as $\mathrm{E}[n^2(t)]$. Therefore, signal to noise ratio (SNR) can be expressed as follows,

$$\mathrm{SNR} = \frac{\mid s_0(t) \mid^2}{\mathrm{E}[n^2(t)]}. \tag{2.7}$$

In order to find a receiving filter which maximize SNR, we first examine the autocorrelation function of $n(t)$ which is given as follows, [8],

$$\begin{aligned} R_n(t) &= \mathrm{E}[\int_{-\infty}^{\infty} g_r(\tau_1) w(t-\tau_1)\, d\tau_1 \int_{-\infty}^{\infty} g_r(\tau_2) w(t-\tau_2)\, d\tau_2] \\ &= \int_{-\infty}^{\infty} g_r(\tau_1)\, d\tau_1 \int_{-\infty}^{\infty} g_r(\tau_2)\, d\tau_2 \mathrm{E}[w(t-\tau_1) w(t-\tau_2)] \\ &= \int_{-\infty}^{\infty} g_r(\tau_1)\, d\tau_1 \int_{-\infty}^{\infty} g_r(\tau_2)\, d\tau_2 R_w(t-\tau_1, u-\tau_2), \end{aligned} \tag{2.8}$$

given that $R_w(t)$ is autocorrelation of white Gaussian noise $w(t)$. Let $\tau = t - u$. From equation 2.8, we have,

$$R_w(t) = \int_{-\infty}^{\infty} g_r(\tau_1)\, d\tau_1 \int_{-\infty}^{\infty} g_r(\tau_2)\, d\tau_2 R_w(\tau - \tau_1 + \tau_2). \tag{2.9}$$

Average noise power $\mathrm{E}[n^2(t)]$ is equal to the autocorrelation of $n(t)$ at $\tau = 0$. Furthermore, we can express equation 2.9 in term of $G_r(f)$ as follows,

$$\begin{aligned} R_n(t) &= \int_{-\infty}^{\infty}\int_{-\infty}^{\infty}[\int_{-\infty}^{\infty} G_r(f)\exp(j2\pi f\tau_1)\,df]g_r(\tau_2)R_w(\tau_2-\tau_1)\,d\tau_1\,d\tau_2 \\ &= \int_{-\infty}^{\infty} G_r(f)\,df\int_{-\infty}^{\infty} g_r(\tau_2)\,d\tau_2\int_{-\infty}^{\infty} R_w(\tau_2-\tau_1)\exp(j2\pi f\tau_1)\,d\tau_1. \end{aligned} \tag{2.10}$$

Let $\tau = \tau_2 - \tau_1$. Equation 2.10 can be expressed as follows,

$$\begin{aligned} R_n(t) &= \int_{-\infty}^{\infty} G_r(f)\,df\int_{-\infty}^{\infty} g_r(\tau_2)\exp(j2\pi f\tau_2)\,d\tau_2\int_{-\infty}^{\infty} R_w(\tau)\exp(j2\pi f\tau)\,d\tau \\ &= \int_{-\infty}^{\infty} \mid G_r(f)\mid^2\ df\int_{-\infty}^{\infty} R_w(\tau)\exp(j2\pi f\tau)\,d\tau \\ &= \int_{-\infty}^{\infty} \mid G_r(f)\mid^2 S_w(f)\,df, \end{aligned} \tag{2.11}$$

provided that $S_w(f)$ is the power spectrum density function of $w(t) : S_w(f) = \frac{N_0}{2}$. Therefore, average noise power is simply given below,

$$\mathrm{E}[n^2(t)] = \frac{N_0}{2}\int_{-\infty}^{\infty} \mid G_r(f)\mid^2\ df, \tag{2.12}$$

From equation 2.4 and 2.12, SNR in equation 2.7 can be expressed as follows,

$$\mathrm{SNR} = \frac{\mid \int_{-\infty}^{\infty} \mid G_r(f)\mid^2 S_h(f)\exp(j2\pi ft)\,df\mid^2}{\frac{N_0}{2}\int_{-\infty}^{\infty} \mid G_r(f)\mid^2\ df}. \tag{2.13}$$

Here, if $S_h(f)$ and $G_r(f)$ are integrable in $[-\infty,\infty]$, we invoke Schwarz's inequality. Then,

$$\begin{aligned} &\mid \int_{-\infty}^{\infty} \mid G_r(f)\mid^2 S_h(f)\exp(j2\pi ft)\,df\mid^2 \\ &\leq \int_{-\infty}^{\infty} \mid G_r(f)\mid^2\ df\int_{-\infty}^{\infty} \mid S_h(f)\mid^2\ df. \end{aligned} \tag{2.14}$$

Therefore,

$$\mathrm{SNR} \leq \frac{2}{N_0}\int_{-\infty}^{\infty} \mid S_h(f)\mid^2\ df. \tag{2.15}$$

SNR is maximized when inequality 2.14 becomes equation. As a result, our desired receiving filter which maximizes SNR must satisfy the following condition,

$$G_r(f) = \alpha S_h^*(f). \tag{2.16}$$

We call this Matched filter

2.3.2 Nyquist Filter

First we assume the transmitted signal $s_i(t)$ is a pulse train of discreet information-bearing sequence I_n which can be represented in term of delta function:

$$s_i(t) = \sum_{-\infty}^{\infty} I_n \delta(t - nT). \tag{2.17}$$

T is a symbol period. After passing through the transmit filter, the equivalent low pass transmitted signal $x(t)$ is given by,

$$x(t) = \sum_{-\infty}^{\infty} I_n g_t(t - nT). \tag{2.18}$$

In practice, $g_r(t)$ is a pulse that has a band-limited frequency response characteristics $G_r(f)$, i.e. $G_r(f) = 0$ for $f > \mid W \mid$, for some positive number W. the signal $x(t)$ is transmitted over a channel having a frequency response $H(f)$. Consequently, the received signal can be represented as,

$$s_h(t) = \sum_{-\infty}^{\infty} I_n c(t - nT) + w(t), \tag{2.19}$$

where

$$c(t) = \int_{-\infty}^{\infty} g_r(\tau) h(t - \tau)\, d\tau. \tag{2.20}$$

Subsequently, the received signal is passed through the receiving filter $g_r(t)$ then sampled at a rate $\frac{1}{T}$ sample/s. The output of the receiving filter is denoted as,

$$y(t) = \sum_{-\infty}^{\infty} I_n d(t - nT) + n(t), \tag{2.21}$$

where $d(t)$ is the response of the receiving filter to the input signal $c(t)$ and $n(t)$ is the response of the receiving filter to the input noise process $w(t)$.

Next, $y(t)$ is sampled as at times $t = kT + \tau_0, k = 1, 2, 3...$ where τ_0 is the time of flight through the channel. We have,

$$y(t) = y(kT + \tau_0) = \sum_{-\infty}^{\infty} I_n d(kT - nT + \tau_0) + n(kT + \tau_0), \tag{2.22}$$

or, equivalently,

$$y_k = \sum_{-\infty}^{\infty} I_n d_{k-n} + n_k, \tag{2.23}$$

where $d_{k-n} = d(kT - nT + \tau_0)$ and $n_k = n(kT - nT + \tau_0)$. The term $d_0 I_k$ represents the desired information symbol at the kth sampling instant. On the other hand, the term $\sum_{-\infty, n\neq k}^{\infty} I_n d_{k-n}$ represents the intersymbol interference (ISI) and is the Gaussian noise random variable at the kth sampling instant. For simplicity, we assume that the band-limited channel has the ideal frequency response characteristics, i.e., $H(f)$ for $\mid f \mid \leq W$ and $H(f) = 0$ for $\mid f \mid > W$. Then, the signal $d(t)$ has frequency characteristic $D(f) = G_t(f)G_r(f)$, where

$$d(t) = \int_{-w}^{w} D(f) \exp(j2\pi ft)\, df. \tag{2.24}$$

We are interested in finding the filters $g_t(t)$ and $g_r(t)$ that result in no intersymbol interference. We know from equation 2.23 that

$$y_k = d_0 I_k + \sum_{-\infty, k\neq n}^{\infty} I_n d_{k-n} + n_k. \tag{2.25}$$

The condition for intersymbol interference free is as follows,

$$d_k = \begin{cases} 1, & k = 0 \\ 0, & k \neq 0 \end{cases} \tag{2.26}$$

This condition is known as Nyquist condition for zero ISI. Based on equation 2.26, we can develop the condition on $D(f)$ for $d(t)$ to satisfy the above condition as follows,

$$d(t) \sum_{k=-\infty}^{\infty} \delta(t - kT) = \sum_{k=-\infty}^{\infty} d(kT) = 1. \tag{2.27}$$

In equation 2.27, we use the fact that multiplying a function by a sum of Dirac delta function (impulses) is equivalent to sampling of that function. Fourier transform of equation 2.27 is given by,

$$D(f) * \frac{1}{T} \sum_{k=-\infty}^{\infty} \delta(f - \frac{k}{T}) = 1, \tag{2.28}$$

and

$$\sum_{k=-\infty}^{\infty} D(f - \frac{k}{T}) = T. \tag{2.29}$$

In order to find $d(t)$ that satisfy equation 2.29, we distinguish three cases.

1. When $T < \frac{1}{2W}$ or, equivalently, $\frac{1}{T} > 2W$, $\sum_{k=-\infty}^{\infty} D(f - \frac{k}{T})$ consist of non-overlapping replicas of $D(f)$. Therefore, there is no $D(f)$ to ensure the summation is equal to T and it is not possible to design a system with no ISI.

2. When $T = \frac{1}{2W}$ or, equivalently, $\frac{1}{T} = 2W$, it is clear that in this case there exists only one $D(f)$ that result in $\sum_{k=-\infty}^{\infty} D(f - \frac{k}{T}) = T$, namely,

$$D(f) = \begin{cases} T, & \mid f \mid \leq W \\ 0, & \mid f \mid > W \end{cases} \tag{2.30}$$

   which corresponds to the time domain function

$$\frac{\sin(\pi t/T)}{\pi t/T} = \text{sinc}(\pi t/T). \tag{2.31}$$

   This is the smallest value of T for which transmission with zero ISI is possible and for this value $d(t)$ has to be sinc function. The difficulty of this choice of $d(t)$ is that it is non-casual and therefore non-realizable. As a result, this case of T is not preferable for designing filters that could result in zero ISI.

3. When $T > \frac{1}{2W}$ or, equivalently, $\frac{1}{T} < 2W$, $\sum_{k=-\infty}^{\infty} D(f - \frac{k}{T})$ consist of overlapping replicas of $D(f)$. In this case, there exist a numerous choices for $D(f)$ such that $\sum_{k=-\infty}^{\infty} D(f - \frac{k}{T}) = T$. The particular function that satisfies the condition, for $T > \frac{1}{2W}$ case, and has been

widely used is the raised-cosine function. The frequency characteristics of the raised-cosine function is given in equation 2.32,

$$d_{rc}(t) = \begin{cases} 1, & \mid f \mid \leq \frac{1-\beta}{2T} \\ \frac{1}{2}[1 + \cos(\frac{\pi T}{\beta}[\mid f \mid -(\frac{1-\beta}{2T})])], & \frac{1-\beta}{2T} \leq \mid f \mid \leq \frac{1+\beta}{2T} \\ 0, & \text{otherwise,} \end{cases} \tag{2.32}$$

Where β is the roll-off factor which takes value in the range $0 < \beta < 1$. The roll-off factor, β, is a measure of the excess bandwidth, i.e., the bandwidth occupied beyond the Nyquist bandwidth of $\frac{1}{2T}$. The excess bandwidth is usually expressed as a percentage of the Nyquist frequency. For example, when $\beta = \frac{1}{2}$, the excess bandwidth is 50% and when $\beta = 1$, the excess bandwidth is 100%. The time domain function, $d(t)$, having the raised-cosine spectrum is

$$d_{rc}(t) = \begin{cases} \frac{\pi}{4T}\text{sinc}(\frac{1}{2\beta}), & t = \\ 0, & \text{otherwise.} \end{cases} \tag{2.33}$$

Due to the smooth characteristics of the raised-cosine spectrum, it is possible to design practical filters for the transmitter and receiver in the special case where the channel is ideal: $H(f) = 1, \mid f \mid \leq W$. Therefore, the condition which the transmitter and receiver must satisfy in order to obtain zero ISI is

$$G_t(f)G_r(f) = D_{rc}(f) \tag{2.34}$$

2.3.3 Optimal Filter

From the subsection 2.3.1 and 2.3.2, we are furnished with the condition on how to design the transmit and receiving filters that maximize SNR and erase ISI. Taking into account of the channel with additive white Gaussian noise and ISI, we combine the two conditions to design an optimal filter as follows,

- matched filter condition

$$G_r(f) = G_t^*(f) \tag{2.35}$$

- zero ISI condition

$$G_t(f)G_r(f) = D_{rc}(f) \tag{2.36}$$

Therefore, we have $\mid G_t(f) \mid^2 = D_{rc}(f)$ and then

$$G_t(f) = \sqrt{D_{rc}(f)}\exp(-j2\pi f t_0), \tag{2.37}$$

where t_0 is some nominal delay that is required to ensure the physical realizability of the filters. Thus, the raised-cosine characteristics is split between the transmit and receiving filters.

2.3.4 ISI Formula

This section presents the mathematical derivation of ISI formula based on the equivalent baseband model as shown in Fig. 2.6. For typical communication system model, the transmitted signal after passing through the pulse-shaping Tx filter ($s(t)$) will undergo up-conversion (mathematically, multiply the signal by $\exp(j2\pi f_c t)$) to make it suitable for transmission through a channel and later after passing through the channel, it will be down-converted (mathematically, multiply the signal by $\exp(-j2\pi f_c t)$) to ensure its suitability for sampling. Taking into account of this process, the equivalent baseband model removes the up-conversion and down-conversion parts and instead shifts the frequency characteristics of the channel to the lower frequency part by the amount of f_c: the carrier frequency or the center frequency of the channel. Let us begin the derivation of ISI formula by first considering the symbol sequence of random variables A_n being transmitted at the instant of time nT after passing through the Tx filter. The output signal $s(t)$ is given by,

$$\begin{aligned} s(t) &= (\sum_{n=-\infty}^{\infty} A_n \delta(t-nT)) * g_t(t) \\ &= \int_{-\infty}^{\infty} \sum_{n=-\infty}^{\infty} A_n \delta(\tau - nT)) * g_t(t-\tau)\, d\tau \\ &= \sum_{n=-\infty}^{\infty} A_n g_r(t-nT) \end{aligned} \tag{2.38}$$

where $*$ denotes convolution integral operator. Next, the signal $s(t)$ is transmitted through the channel $h(t)$, the output of which, namely $s_h(t)$, is given by

$$s_h(t) = \sum_{n=-\infty}^{\infty} A_n x(t-nT), \tag{2.39}$$

provided that $x(t) = g_r(t) * h(t)$. In the same manner, the output signal $r(t)$ of the Rx filter is given by

$$s_h(t) = \sum_{n=-\infty}^{\infty} A_n y(t - nT), \tag{2.40}$$

where $y(t) = x(t) * g_r(t)$. However, for calculation purpose, we might as well express $y(t)$ in terms of spectral functions as follows,

$$\begin{aligned} y(t) &= \mathcal{F}^{-1}\{G_t(f)H(f + f_c)G_r(f)\} \\ &= \int_{-\infty}^{\infty} G_t(f)H(f + f_c)G_r(f) \exp(j2\pi ft)\, df, \end{aligned} \tag{2.41}$$

Where $\mathcal{F}^{-1}$ denotes the inverse Fourier transform operation and $G_t(f)$, $H(f + f_c)$, and $G_r(f)$ are the Fourier transform of $g_t(t)$, $h(t)$, and $g_r(t)$ respectively. Subsequently, the received signal $r(t)$ is sampled at the rate of $kT + \tau_0$ for $k = 1, 2, 3, ...$ τ represents the transmission delay through the channel, sometimes referred to as the time of flight. The output to the sampling process is the discreet information-bearing $\{Y_k\}$ which is expressed below,

$$\begin{aligned} Y_k &= y(kT - nT + \tau_0) \\ &= \sum_{n=-\infty}^{\infty} A_{k-n}\Gamma_n, \end{aligned} \tag{2.42}$$

and

$$\begin{aligned} \Gamma_m &= \int_{-\infty}^{\infty} G_t(f)H(f + f_c)G_r(f) \exp(j2\pi f(mT + \tau_0))\, df \\ &= \int_{-\infty}^{\infty} D_{rc}(f)H(f + f_c) \exp(j2\pi f(mT + \tau_0))\, df. \end{aligned} \tag{2.43}$$

From equation 2.42, we can distinguish the sampled sequence into two parts:

$$y_k = A_k\Gamma_0 + \sum_{n=-\infty, n\neq k}^{\infty} A_n\Gamma_{k-n}. \tag{2.44}$$

The first term of RHS of equation 2.44 is the desired information symbol and the rest of the terms is interference. Intersymbol interference is defined as the ratio of interference power over the desired symbol power:

$$\text{SNR} = \frac{|\sum_{n=-\infty, n\neq k}^{\infty} A_n\Gamma_{k-n}|^2}{|A_k\Gamma_0|^2} \tag{2.45}$$

Because we are interested in the average value of ISI, we suppose that the random symbol A_n has the following properties:

1. The average value of the random symbol is zero, i.e., $\mathrm{E}[A_n] = 0$.
2. The average power of the random symbol is P, i.e., $\mathrm{E}[\mid A_n \mid^2] = P$.
3. Two different random symbols are independent, i.e., $\mathrm{E}[A_m A_n^*] = \mathrm{E}[A_m]\mathrm{E}[A_n]^* = 0$ for $m \neq n$.

In addition, the transmit filter $g_t(f)$ and the receiving filter $g_r(f)$ constitute the raised-cosine filter. Hence, the average desired symbol power is

$$\mathrm{E}[\mid A_n \Gamma_0 \mid^2] = \Gamma_0^2 \mathrm{E}[\mid A_n \mid^2] = \Gamma_0^2 P, \tag{2.46}$$

and average interference power is

$$\begin{aligned} &\mathrm{E}[(\sum_{m=-\infty, m\neq k}^{\infty} A_m \Gamma_{k-m})(\sum_{n=-\infty, n\neq k}^{\infty} A_n \Gamma_{k-n})^*] \\ &= \sum_{m=-\infty, m\neq k}^{\infty} \sum_{n=-\infty, n\neq k}^{\infty} \Gamma_{m-k} \Gamma_{n-k}^* \mathrm{E}[A_m A_n^*] \\ &= \sum_{n=-\infty, n\neq k}^{\infty} \mid \Gamma_{n-k} \mid^2 \mathrm{E}[\mid A_n \mid^2] \\ &= P \sum_{n=-\infty, n\neq k}^{\infty} \mid \Gamma_{n-k} \mid^2 \end{aligned} \tag{2.47}$$

Therefore, we arrive at

$$\mathrm{ISI} = \frac{\sum_{n=-\infty, n\neq k}^{\infty} \mid \Gamma_{k-n} \mid^2}{\mid \Gamma_0 \mid^2} \tag{2.48}$$

In practice, the limit of summation in equation 2.47 need not go to infinity because the interference level of the symbols far from the symbols of interest is negligible: for example, if the desired symbol is A_0, interference effect resulting from the symbols A_m :$\mid m \mid > 5$ is insignificantly small. Moreover, the limit of integration in equation 2.43 is determined by the raised-cosine filter: as the matter of facts, $D_{rc} = 0$ for $\mid f \mid > \frac{1+\beta}{2T}$. The inverse proportion of ISI is referred to as signal to interference ration (SIR).

2.4 ISI Estimation Using Near-Field Distribution

In the previous section, the important parameters and expressions required to compute ISI are presented and as mentioned there, the unknown parameter is the channel transfer function. Depending on the wireless channel components (the Tx antenna, the Rx antenna, and the propagation environment), the estimation of its characteristic function might be very complicated even with the help of simulation software. To get around this problem, we limit our consideration to the situation shown in Fig. 2.4. Also, the evaluation model is appropriate for our system because this system preference is line of sight and multi-path effects from the surroundings, [1], [2], which are suppressed due to the adoption of a large array antenna (such as the 64x32-slotted array antenna here) to make a uniform field in a rectangular volume in the non-far region. Unfortunately, even for the case of this model, the antenna size however prevents using electromagnetic simulation software. In this section, we introduce the method to evaluate the channel transfer function and ISI in detail using the near-field distribution of the array antenna in consideration here.

2.4.1 Measurement of the Near-field distribution

The first step in evaluating the channel transfer function is the near-field measurement of an antenna in consideration. In this study, the near-field measurement is conducted on a 64x32-slot array antenna. The measurement details are as follows,

1. Measured area: 600×320 mm^2.
2. Sampling interval: 4 mm.
3. Frequency range: 29.06-30.14 GHz.
4. Number of the measured frequencies: 37.

The measurement area has to be sufficiently much larger than the size of the array antenna being tested. However, the larger the measurement area, the longer the measurement time, as the sampling interval has to be smaller than one half of the wavelength of the lowest measured frequency. The

frequency range is scaled down to half of the transmission bandwidth (2.16 GHz) of the channel in the 60 GHz-band system. As for the number of the measured frequencies, it is preferable to measure as many frequency points as possible to obtain accurate details of the frequency characteristics across the whole band (29.6-30.14 GHz). More measured frequencies result in a longer measurement stage however, and a trade-off has to be considered. Fig. 2.7a-2.7f show the amplitude and the phase of the near-field distributions at the edge and center of the band, showing that the amplitude and phase varied within 3 dB and 60 degrees over almost all of the array aperture. The non-uniformity in the field distribution of the array antenna is clearly reflected through these results of the near field measurements and results are difficult to predict using simulation software as we have no way of knowing how much and where errors occur in the antenna after fabrication.

2.4.2 Estimation of Channel Transfer Function

With the near-field distributions for various frequencies in subsection 2.4.1, the fields at the Rx antenna can be estimated. This can be achieved by mean of dipole approximation as illustrated in Fig. 2.8. The amplitude and the phase values of each sampling represent those of magnetic current dipoles at the corresponding position. As a result, the slot array antenna can be replaced by the array of infinitesimal magnetic current dipoles, the amplitude and the phase of which are determined by those of the near-field distribution. By summing the total contribution from each dipole, the fields at the Rx antenna radiated from the Tx antenna are obtained for each measured frequency. Assuming that the receiving frequency characteristics of the Rx antenna are approximately uniform (which is true for the case of a waveguide probe WR-28), the channel transfer function $H(f + f_c)$ can be represented by the field radiated by the Tx antenna, see equation (A6). This makes it possible to obtain a discreet channel transfer function (37 points) using the near-field distribution.

To extend this procedure to a continuous function, interpolation is required, and here spline interpolation is applied to create a smoothly continuous function [9]. A discreet channel transfer function composed of the 37 frequency points is determined from the fields at the corresponding measured frequencies. Then, with a continuous channel transfer function interpolated from the discreet channel transfer function (37 points) using spline interpolation, Fig. 2.9a-2.9b show examples of the channel transfer function

($H(f + f_c)$) estimated from the near-field distribution (blue line). The red line shows the directly measured $H(f + f_c)$. The $H(f + f_c)$ estimated from the near-field distribution shows a similar appearance as that of the direct measurement except in the 30 GHz to 30.14 GHz frequency range. This disagreement is likely caused by the shift of the Rx antenna position from the center of the Tx antenna. In the non-far region, a slight shift can significantly change S_{21} (this effect over ISI will be discussed further in Section 2.5). Also, the rate of change in the fields increases with the frequency increases, probably leading to the disagreements at the high frequency range.

2.4.3 ISI Calculation

The above suggests a way to determine the channel transfer function is available. The ISI can be computed using equation 2.43 and 2.48. First, the channel coefficient Γ_0 is computed using the integral expression in equation 2.43 performed using numerical integration (Simpson's rule). Concurrently, the time of flight τ_0 has to be searched for, numerically, to maximize Γ_0. In the case of ideally uniform excitation, τ_0 is equal to t_{min}: the propagation time from the center of the array to the observation point on the Z axis according to Fig. 2.4. For the general case, τ_0 is determined from the interval $[t_{min} - 5T, t_{min} + 5T]$ where T is the symbol period. This interval is specified based on the time of flight having to be around t_{min} as our desired symbol first arrives at the receiver at t_{min}, the slowest desired symbol should arrive within T seconds after the first. Taking into account the characteristics of an inverse raised cosine function, the peak value would lie within $[t_{min} - 2T, t_{min} + 2T]$ after total interference. Here, $5T$ is used to ensure that error due to the approximate prediction of the position of the peak value is compensated for. After τ_0 is determined, all the channel coefficients Γ_n (including Γ_0) can be computed using τ_0. The parameters required to calculate equation 2.43 are given as follows,

1. Center frequency: $f_c = 29.6$ GHz.
2. Symbol period: $T = 1.17$ ns.
3. Bandwidth: BW = 1.08 GHz.
4. Roll-off filter: $\beta = 0.25$ (see subsection 2.3.2).

At this point all the channel coefficients Γ_n are known, and ISI can be computed via equation 2.43. Though the limit of summation in equation 2.43 is infinite, the computation of such terms is possible through truncation. In fact, here the truncation is justified because of the characteristics of the inverse raised-cosine that is a one-side decreasing function. This ensures that Γ_n decreases as $\mid n \mid$ increases. The results given in the following section were estimated assuming that A_k (Γ_0) is the desired signal and interference terms are truncated to 10 terms:

$$\begin{aligned}\{&A_{k-5}(\Gamma_5), A_{k-4}(\Gamma_4), A_{k-3}(\Gamma_3), A_{k-2}(\Gamma_2), A_{k-1}(\Gamma_1), A_k(\Gamma_0),\\ &A_{k+1}(\Gamma_{-1}), A_{k+2}(\Gamma_{-2}), A_{k+3}(\Gamma_{-3}), A_{k+4}(\Gamma_{-4}), A_{k+5}(\Gamma_{-5})\}\end{aligned} \tag{2.49}$$

2.5 Results

This section presents a discussion of results of the discussion developing the method proposed here as well as experiment based results are included. Direct measurements of ISI are difficult and the determine ISI experimentally, we measured a related quantity, $H(f + f_c)$. The quantity $(H(f + f_c))$, is directly related to ISI and determine a value for severity of ISI for a communication system. In this way, an experiment based ISI can be obtained from the directly measured $H(f + f_c)$ by following the method detailed in the previous section.

Before considering the results of the discussion of the proposed method and the experimentally determined ISI, it is useful to recall the physical interpretation of ISI for a large array antenna. The situation giving rise to an ISI is that signals follow different paths resulting in differences in delays, and as the result signals arrive at the receiver at different times and symbols then interfere with each other. In the case here with a large array antenna, signals travel from different elements to a receiver and undergo different path delay (the adoption of a corporate feed circuit in the Tx antenna makes the internal delay negligible) due to the large size of the array, the effect on signals traveling from the center of the array and the corner of the array is different, as suggested in Fig. 2.10. The delay difference is large when the receiver is close to the array and a large value of ISI can be expected. In this case, the differences in the delay decrease for the receiver farther away from the array and result in smaller ISI value, put generally, ISI decreases as the transmission distance increases.

2.5.1 ISI Comparison with the Direct Measurement

Fig. 2.11 illustrates the ISI results. The red line represents the ISI estimated from the near field distribution. The black star-like dots show the ISI values obtained by the directly measured $H(f + f_c)$. Comparing these values, the ISI results estimated by the proposed method and the directly measured ones are similar but not in complete agreement. The discrepancy may be attributed to shifts in the Tx and Rx antennas as will be demonstrated below. One of difficulties in the direct $H(f + f_c)$ measurement is the alignment between the Tx and the Rx antennas. Even with a 3D scanner, it is still not straightforward to align the Tx and the Rx antennas. As the Rx antenna is in the non-far region where fields change very much, a small shift would cause a change in the $H(f + f_c)$ prediction as well as in the ISI. In consideration of this, the effect of a shift can be quantified, and the blue curves in Fig. 2.11 show the upper and lower boundaries of possible ISI values evaluated by assuming that the Rx antenna is shifted within ± 3 cm horizontally and ± 1 cm vertically. The region within these boundaries show the possible ISI values when the shift is included. It is clear that all the ISI results estimated from directly measured $H(f + f_c)$ lie within this region, strongly suggesting that the shift of the Rx antenna from the Tx antenna can account for the discrepancies between the ISI results. Note that the shift range of 3 cm is acceptable in practice as, at a distance of 2 m, a 1-degree horizontal (or vertical) deviation by the probe corresponds to a 3.5 cm shift horizontally (or vertically) in the probe position.

The reasons why this study is able to conclude that the shift in the position of the Rx antenna is dominant in our proposed ISI analysis method are:

1. The Rx antenna is in the near field region where a slight change in position may result in a significant change in the receiving field. The effect detailed above also reflects the results in Figs. 2.11 where the ISI discrepancy, both between the ISI results estimated from the measured results and near-field at the center of the Tx antenna, and also between the ISI results estimated from the measured results and near-field including the shift, decrease as the transmission distance increases because the receiving field at the Rx antenna increasingly behaves as a field in the far-field region with increasing distance between the Tx and the Rx antennas; also substantiating that a shift in the Rx antenna position in the Tx antenna plane has an insignificant effect on the ISI

level (value) far from the Tx antenna. When the transmission distance is shorter, the shift in the Rx position would cause a larger change in the ISI level, as in Figs. 2.12a-2.12b, 11. For the experiments, a 3D scanner was not available and the alignment between the Tx and the Rx antennas was performed manually, making the alignment between the Tx and Rx antennas susceptible to error.

2. The coverage of the compact range communication system is in the non-far region and within the cross-sectional area of a Tx antenna (a large array antenna). For such a situation, it is suitable that the ISI value is estimated within an area (or more specifically a rectangular volume) rather than based on a point-wise estimation and that the possible values of the ISI are indicated in that particular area. Conclusively, the estimation of ISI including the effect of any shift is practical and acceptable.

Still, it should be borne in mind that this study simplifies the analysis (Section 2.3) of the ISI value by assuming that the Rx antenna receives the field radiated by the Tx antenna without disturbance of the Tx antenna or the system itself. This implies that theoretically multiple reflection effects between the Tx and the Rx antennas are disregarded. For a validation of the method proposed here, a measurement result free of multiple reflections is desirable. However, in actual measurements this effect cannot be avoided. The multiple reflection effect increases as the transmission distance shortens, especially in the near-field region as is clearly shown in the case of this study. In turn, this may unavoidably have affected the measurement results and it is difficult to calculate how large an effect this has had on the experiments here. In future study, we will include modifications of the analysis by taking the multiple reflection effects into account bearing in mind that this will increase the complexity of the method of the analysis.

To discriminate the influence of the horizontal and vertical shifts, the ISI boundaries were calculated separately for the horizontal and vertical shifts within ± 2 cm as shown in Figs. 2.12a and 2.12b. Here the shift along the horizontal axis affects ISI especially at distances far from the antenna more than it affects that along the vertical axis. The physical reason for this difference in the behavior can be explained by the near field distribution. The ISI variation by the horizontal shift is affected by differences in the near-field distribution between the left and right sides of the array aperture, while that by the vertical shift is affected by the differences between the upper- and

lower-half sides. Looking at the near-field distributions in Fig. 2.7, we can see that the difference between the left and the right sides is larger than that between the upper-half and the lower-half sides. This difference is certain to affect $H(f + f_c)$. It may be concluded that ISI is affected more strongly by the shift along the horizontal axis than that along the vertical axis at distances far from the Tx antenna.

2.5.2 Application to the Signal to Noise plus Interference Ratio (SINR)

In this subsection, the signal to noise plus ratio (SINR) is estimated using the estimated ISI from the previous subsection and, at the end of the present subsection, the effect of ISI and noise on the communication quality is discussed. For this, first, the received power has to be determined. The received power can be expressed as a function of $H(f + f_c)$ and the input power in P_{in}, as in equation (A1) in the Appendix. Assuming the input power to the array 1 in $P_{in} = 1$ (mW). The received power at various distances can be readily determined as shown in Fig. 2.13. Noise is one degradation factor which is caused by the electronics devices and by the ambience. Thermal noise N_{T} is commonly considered, and assuming a noise figure (NF) value of the system as 10 dB [8], the noise temperature T is 300 K and the receiver bandwidth B equal to 1.08 GHz. Then the thermal noise power is given by

$$\begin{aligned} P_{N_{\mathrm{T}}} &= \mathrm{NF} - 168.6 + 10\log_{10}(B) + 10\log_{10}(\mathrm{T}) \\ &= -73.5 \quad \mathrm{dBm} \end{aligned} \tag{2.50}$$

As detailed further in equation (A2) in the appendix. This makes it possible for SNR to be evaluated, and the distribution of interference from each element to the receiver becomes $I_i : i = 1, 2, 3, ..., 64 \times 32$ with the total interference at the receiver $I_{re} = I_1 + I_2 + I_3 + ... + I_{64\times32}$. From the central limit theorem [10], [11], the distribution of I_{re} can be approximated by a Gaussian distribution, as the number of elements, 64×32, is large. Finally, SINR can be calculated using equation (A3) in the appendix and the results of SINR and SNR are shown in Fig. 2.14. It can be seen that SINR is larger than SNR. Given the fact that the intended transmission distance for the system is normally up to 10 m it may be concluded that ISI is the dominant factor for the system.

2.6 Concluding Remarks

A method for estimating ISI from the near-field distribution is proposed as a promising alternative to predict ISI in a non-far region system using large array antennas and would be later incorporated in predicting BER performance. The ISI estimation by means of the proposed method is demonstrated. The ISI estimated from the near-field distribution is compared with the ISI estimated from directly measured $H(f + f_c)$ values. The results are in good agreement, though some discrepancies are observed. The shifting of the Rx antenna from the Tx antenna is shown to account for the discrepancy. The ISI boundary is estimated by taking the shift into account. Finally, SINR, as well as SNR, are estimated from the ISI results obtained for both, and the ISI is shown to be the dominating factor over noise for the current situation. This implication strongly suggests that ISI estimation is important in designing communication systems like that considered here. To achieve the ultimate target, i.e., accurately predicting the BER performance of the system, the further modifications to the ISI estimation method are needed. More precisely, the accurate prediction of the BER performance of the actual system would involve the effect of signal processing components. A related study could be found in [12].

It should be emphasized that the proposed method suggests a procedure to estimate ISI. It, however, does not provide a implementable mean to alleviate ISI. Incidentally, it is more pragmatic to adopt signal processing techniques to deal with the ISI problem. As a matter of fact, the actual system was equipped with the equalizer on the receiving end and LDPC was utilized to improve the system performance as already mentioned in the introduction.

Specification	[3]	This work
Antenna size	9×9 mm^2	251×251 mm^2
Coverage	5.1 m	10 m
Field-region	Far	Near
Data rate	3.5 Gb/s	3.5-6 Gb/s
Bandwidth	2.16 GHz	2.16 GHz
Modulation	QPSK	QPSK
Coding scheme	LDPC	LDPC
Multiplexing	Single carrier	Single carrier

Table 2.1: 60 GHz short-range wireless communication systems

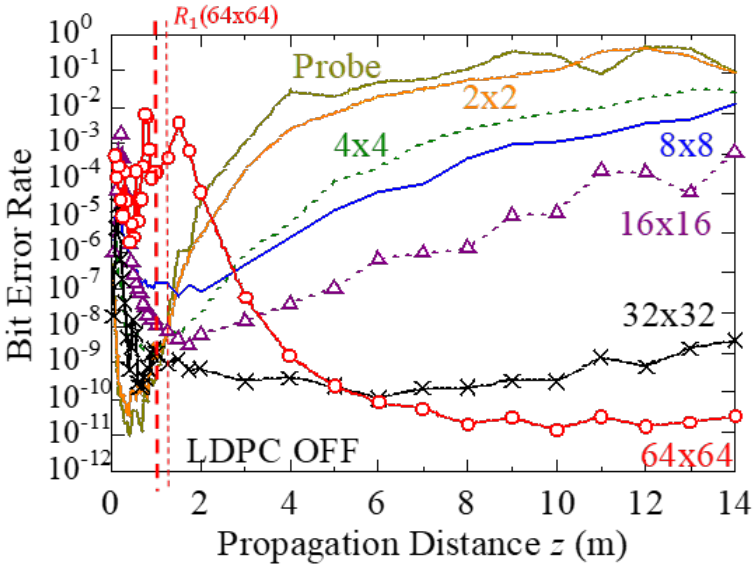

Figure 2.1: BER measurement

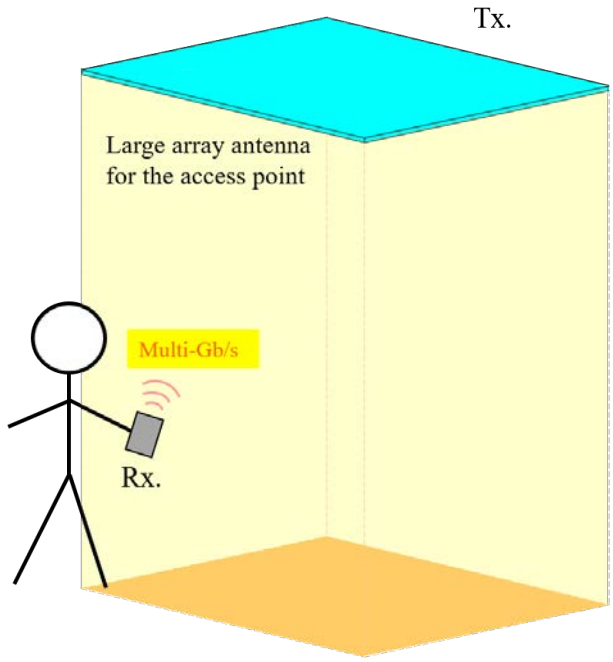

Figure 2.2: Non-far region communication system

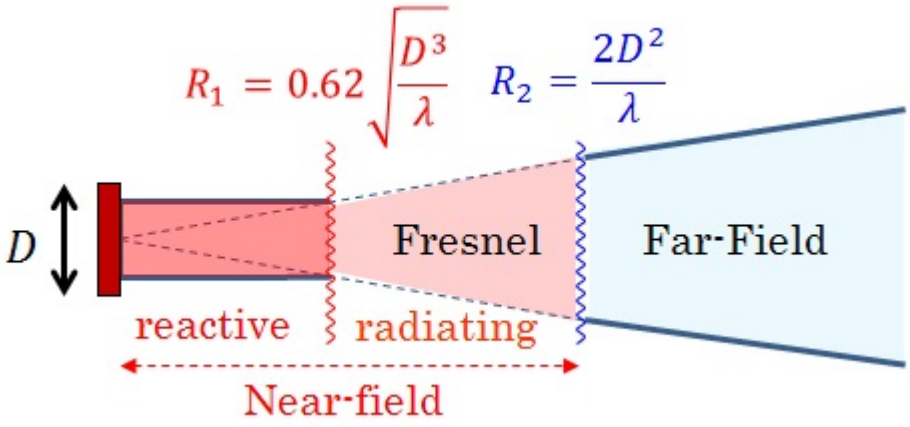

Figure 2.3: Field regions

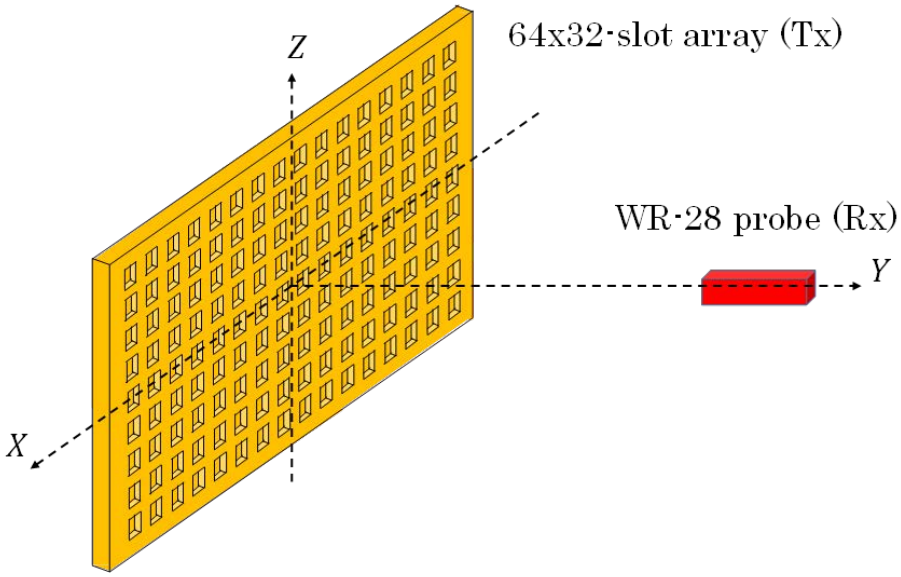

Figure 2.4: Evaluation model

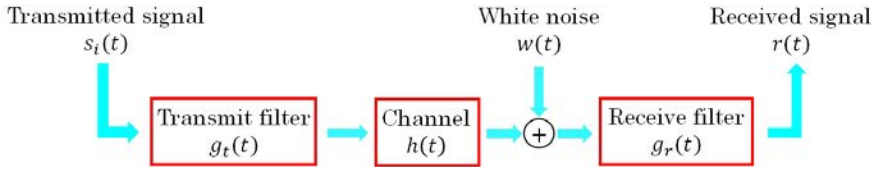

Figure 2.5: Communication system model

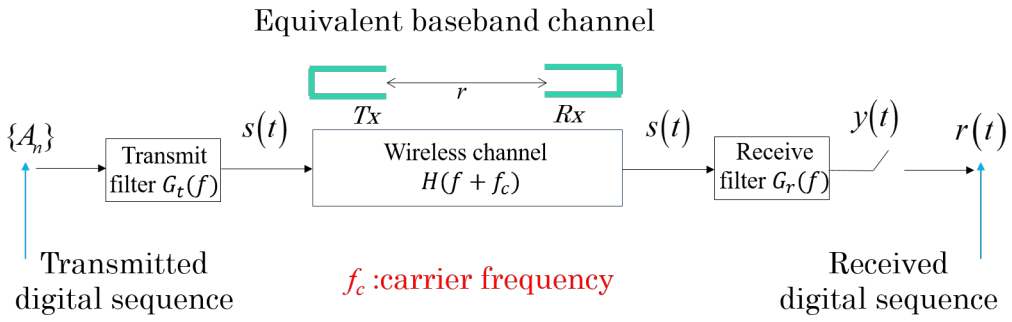

Figure 2.6: Equivalent baseband model

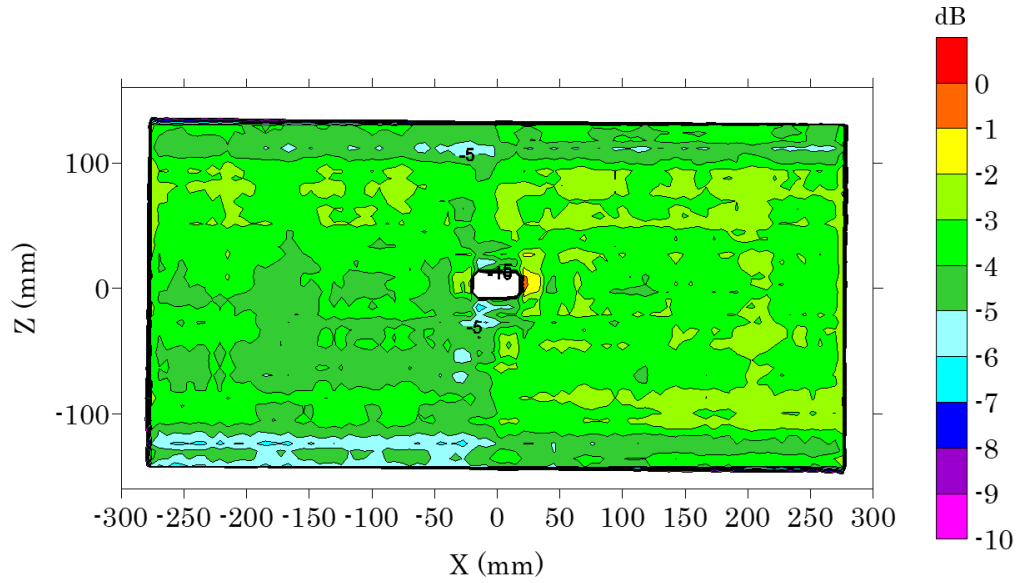

(a) Relative amplitude at 29.06 GHz

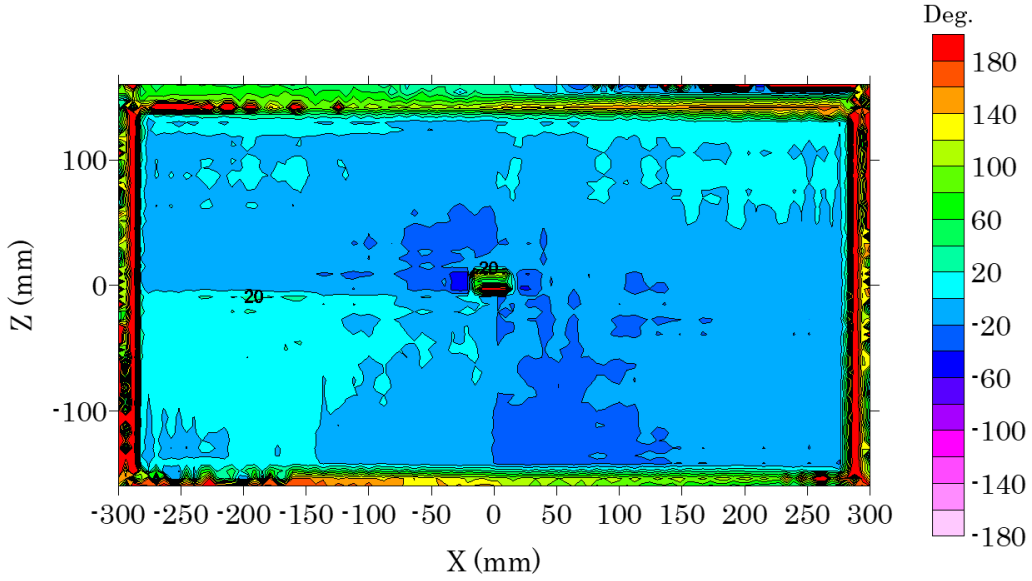

(b) Relative Phase at 29.06 GHz

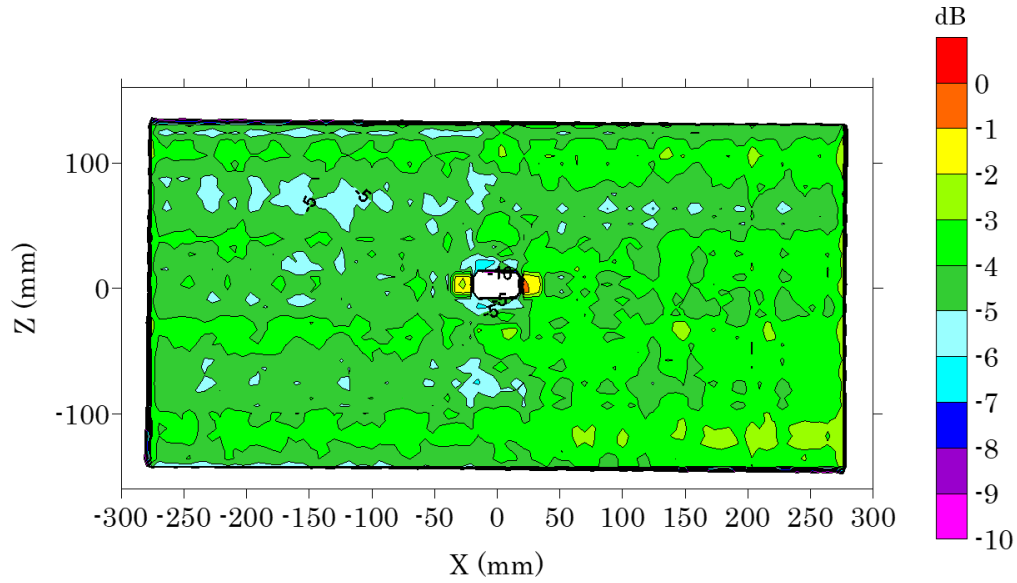

(c) Relative amplitude at 29.60 GHz

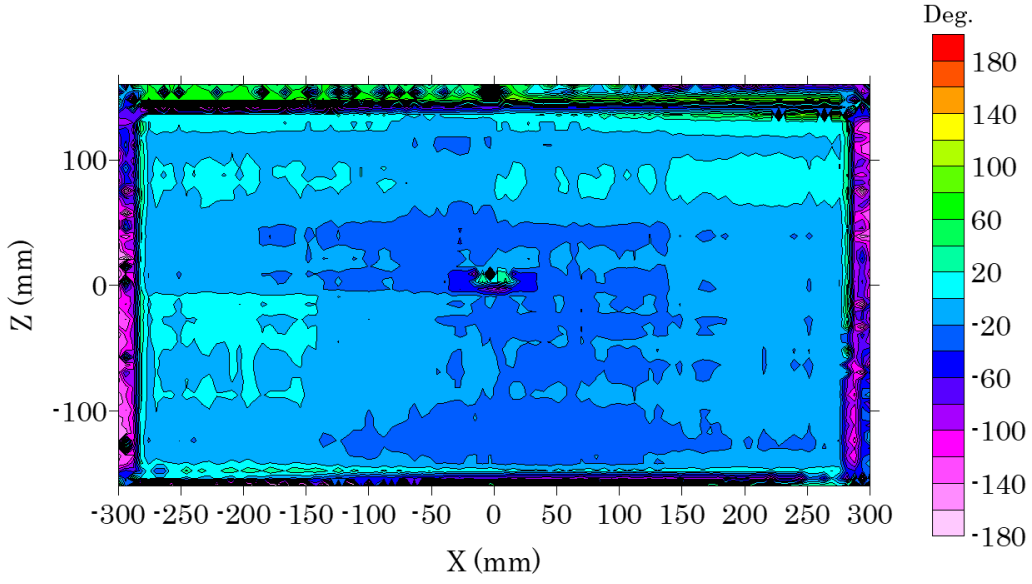

(d) Relative Phase at 29.60 GHz

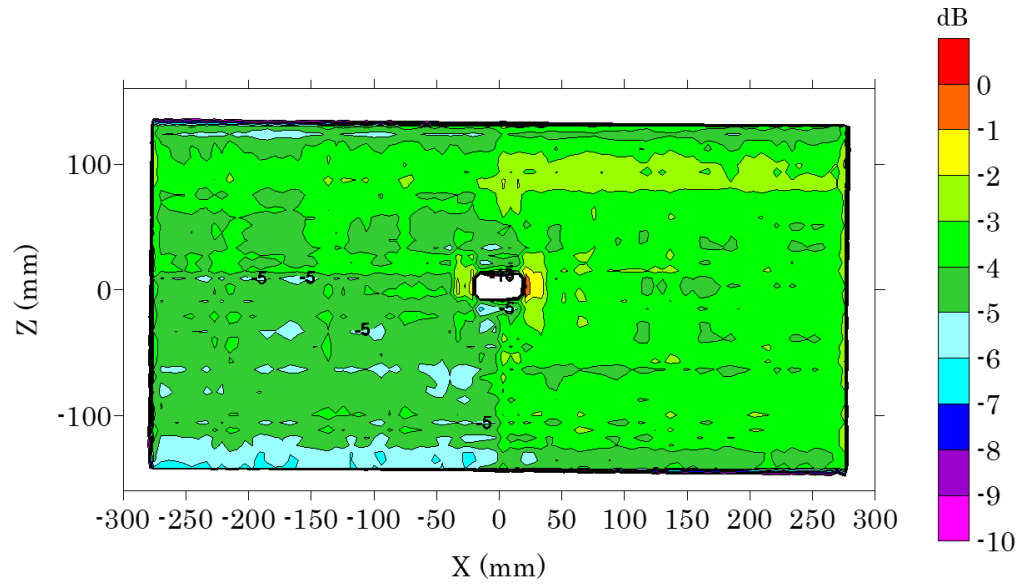

(e) Relative amplitude at 30.14 GHz

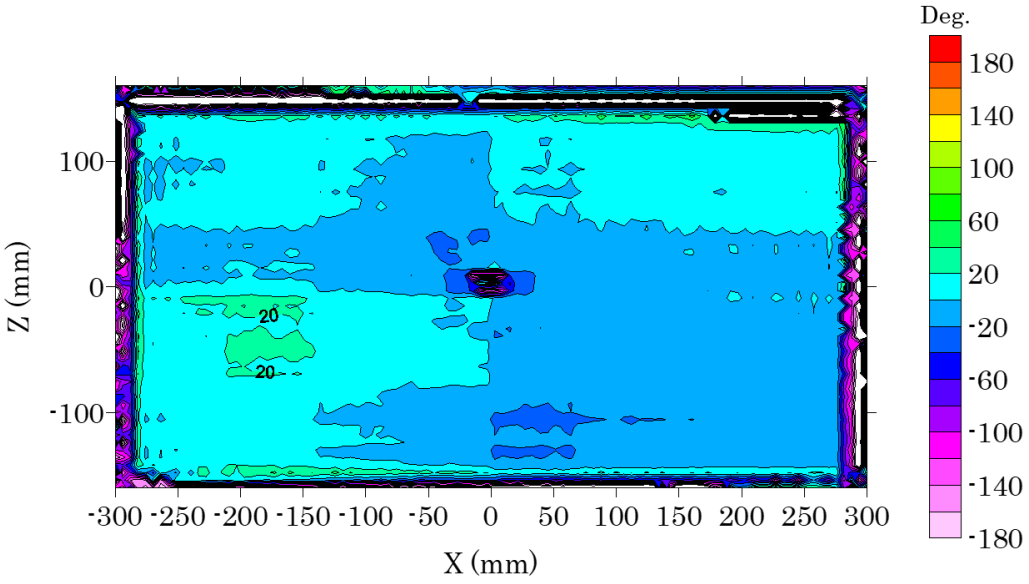

(f) Relative Phase at 30.14 GHz

Figure 2.7: Near-field distribution

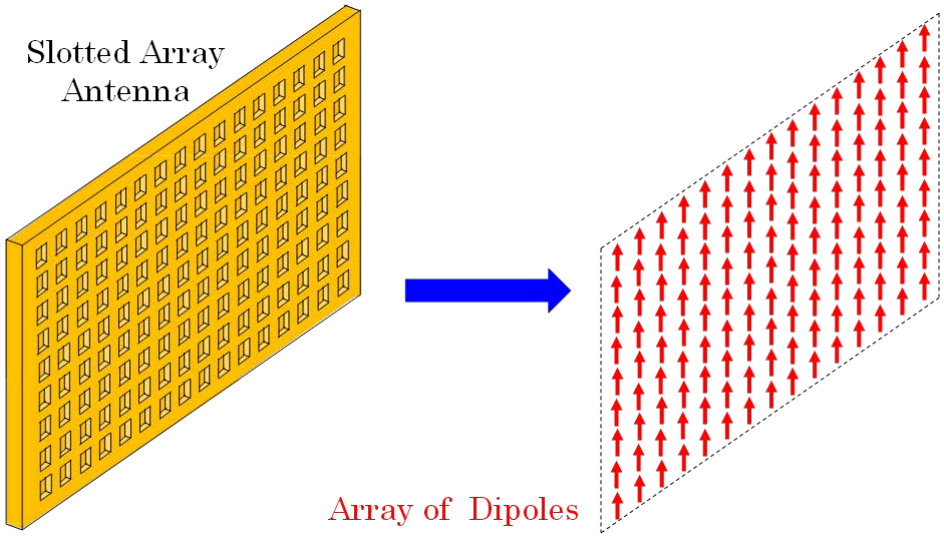

Figure 2.8: Infinitesimal dipole approximation

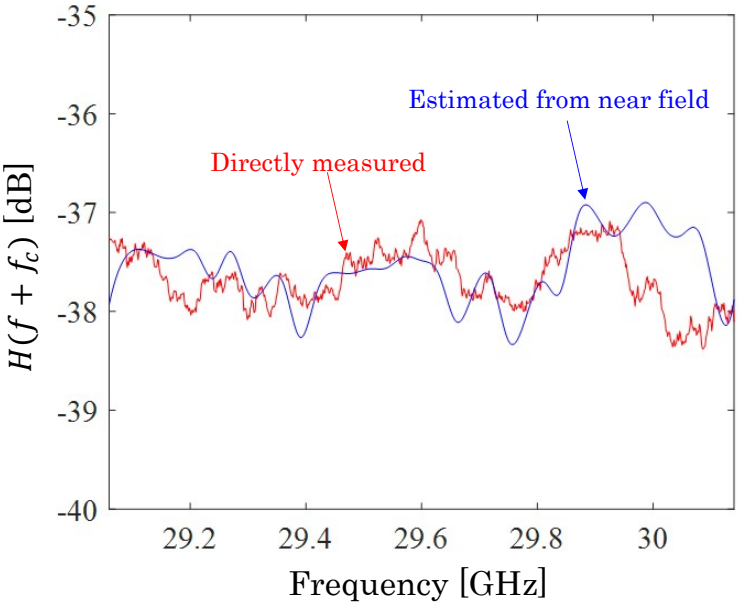

(a) 2 m

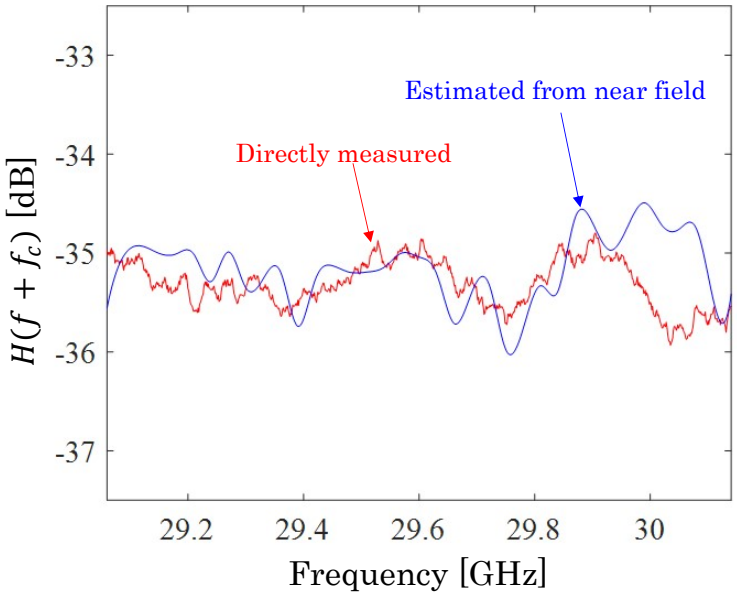

(b) 3 m

Figure 2.9: Estimated channel transfer function

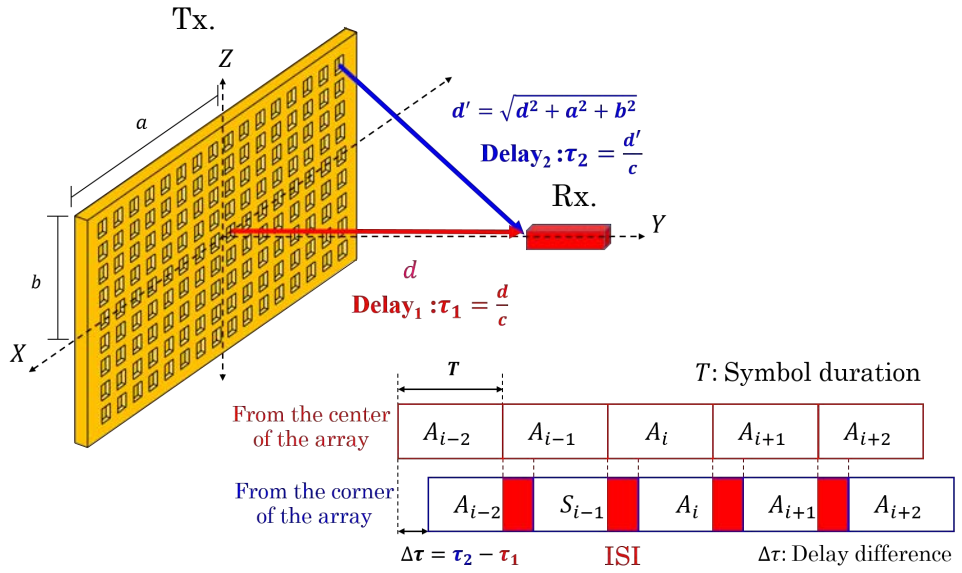

Figure 2.10: Graphical visualization of the ISI arising in a large array antenna

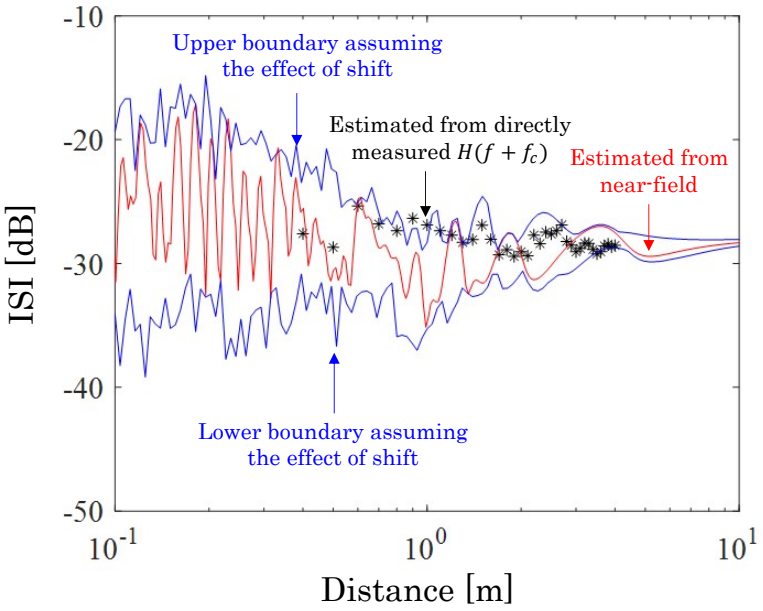

Figure 2.11: ISI variation due to shifts in the Rx antenna

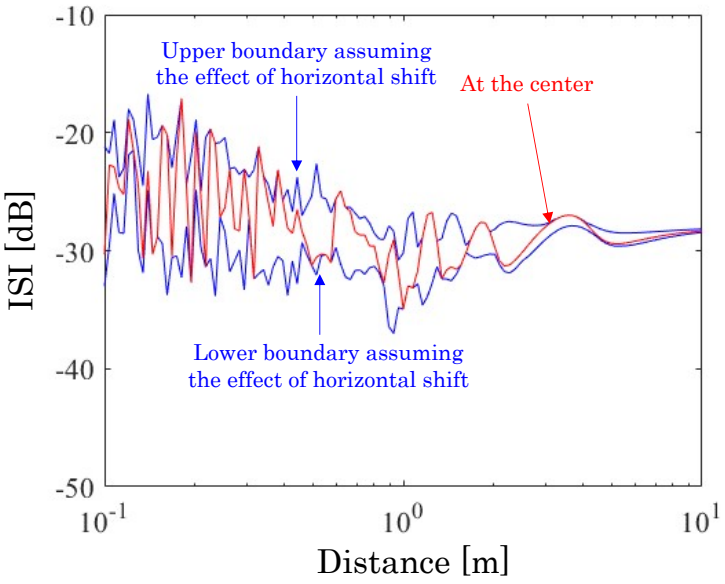

(a) Horizontal

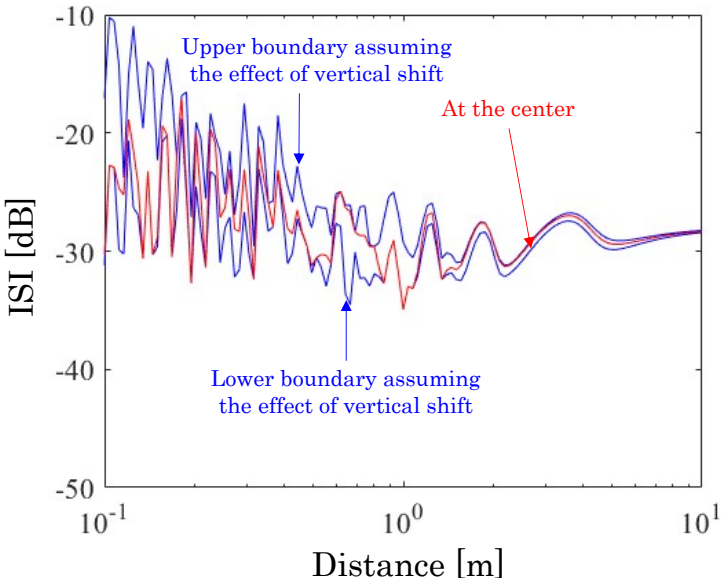

(b) Vertical

Figure 2.12: Influence of antenna shifts on the ISI

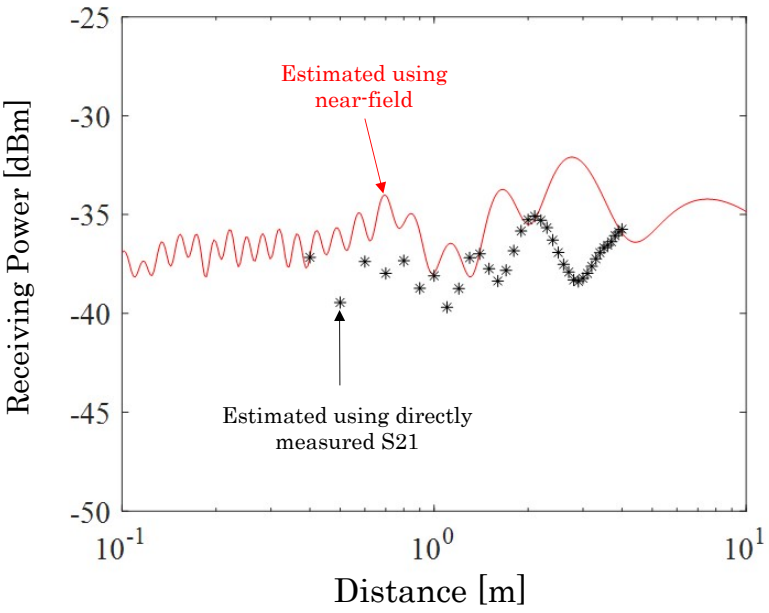

Figure 2.13: Receiving power comparison

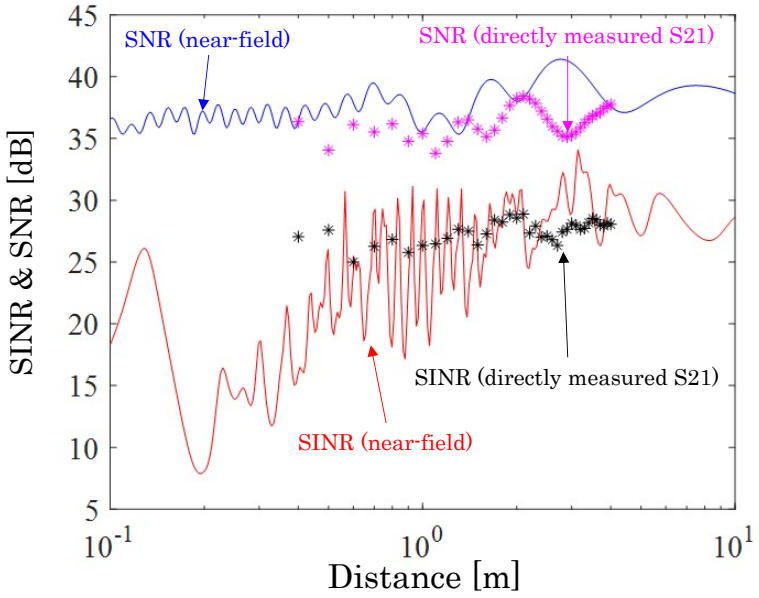

Figure 2.14: SINR and SNR comparison

References

[1] M. Zhang, K. Toyosaki, J. Hirokawa, M. Ando, T. Taniguchi, and M. Noda, "A 60 ghz-band compact-range gigabit wireless access system using large array antennas," *IEEE Transactions on Antennas and Propagation*, vol. 63, no. 8, pp. 3423–3440, Aug. 2015.

[2] M. Ali and M. Ando, "Fast estimation of shadowing effects in millimeter-wave short range communication by modified edge representation," *IEICE Transactions on Communications*, vol. E98-B, no. 9, pp. 1873–1881, Sep. 2015.

[3] G. Yue, Z. Wang, L. Chen, L. Cheng, J. Tang, X. Zou, Y. Zeng, and L. Li, "Demonstration of 60 ghz millimeter-wave short-range wireless communication system at 3.5 gbps over 5 m range," *Science China on Information Science*, vol. 60, no. 12, Aug. 2017.

[4] M. Zhang, M. Wakasa, K.Araki, J. Hirokawa, and M. Ando, "Analysis of intersymbol interference in a 60 ghz-band compact-range wireless access system using various large array antennas," *International Symposium on Antennas and Propagation (ISAP)*, S3.3.4, Nov. 2015.

[5] M. Wakasa, M. Zhang, J. Hirokawa, K.Araki, and M. Ando, "Intersymbol interference analysis of a compact-range highspeed wireless communication system using travelling-wavefed slot arrays," *IEICE Technical Report.*, AP2015-45, Jun. 2015.

[6] C. A. Balanis, *Advanced Engineering Electromagnetics*. New York: John Wiley & Sons, 1989.

[7] D. Kim, J. Hirokawa, M. Ando, J. Takeuchi, and A. Hirata, "64x64-element and 32x32-element slot array antennas using double-layer hollow-waveguide corporate-feed in the 120 ghz band," *IEEE Transactions on Antennas and Propagation*, vol. 62, no. 3, pp. 1507–1512, Mar. 2014.

[8] J. G. Proakis, *Digital Communications, Fourth Edition*. New York: McGraw-Hill, 2001.

[9] M. Hazewinkel, *Encyclopaedia of Mathematics, vol.3*. Kluwer, 2008.

[10] A. L. Garcia, *Probability, Statistic, and Random Processes for Electrical Engineering*. New Jersey: Pearson Prentice Hall, 2008.

[11] S. S. Haykin, *Communication Systems*. New York: John Wiley & Sons, 2011.

[12] M. Zhang, M. Wakasa, K. Toyosaki, K. Araki, J. Hirokawa, and M. Ando, "Analysis of intersymbol interference characterized by the large array antennas adopted in a 60-ghz-band gigabit compact-range wireless access system," *IEEE Access*, vol. 9, pp. 80 077–80 087, May 2021.

[13] K. F. Riley, M. P. Hobson, and S. J. Bence, *Mathematical Methods for Physics and Engineering*. Cambridge: Cambridge Univ. Press, 2006.

[14] T. Zhang, L. Li, M. Xie, H. Xia, X. Ma, and T. J. Cui, "Low-cost aperture-coupled 60-ghz-phased array antenna package with compact matching network," *IEEE Transactions on Antennas and Propagation*, vol. 65, no. 12, pp. 6355–6362, Dec. 2017.

Chapter 3

Short-Range Transmission Improvement by Dog-bone Cross-slot Feed in Radial Line Slot Antenna

3.1 Introductory Remarks

Wireless power transmission has received an attention from an industry for charging electric vehicles and drones [1], [2], [3]. There are mainly two types of wireless power transmission: the non-radiative type in which the power is transferred over short distances using techniques, e.g., magnetic/electric couplings [4], [5], magnetic/electric resonances [6], [7], and the radiative type in which power is transferred by beams of electromagnetic radiation over longer distances using microwaves or laser [1], [8]. However, the efficiency of the radiative type is often limited by the divergences of beams (radiated fields). On the contrary, the several techniques of the non-radiative type are generally applicable over short distances. Taking the trade-off between transmission efficiency and distance into consideration, a beam-typed technique was introduced [1]. With a electrically large aperture/array antenna and their non-far region, high efficiency power transfer over longer distances can be realized [1], [9]. In similar fashion to the short range communication, radiated power in non-far region is stored in a volume enclosing the radiating surface of the antenna.

A radial line slot antenna (RLSA) was originally designed for satellite communication [10]. It was also proposed for Solar power satellites in [8]. A following work [11] includes it as a candidate for the compact-range communication system. A recent work [12] proposes the application of RLSAs for wireless power transmission; the Tx antenna is a conventional waveguide-fed RLSA and the Rx antenna is the eight-port-microstrip-line-fed RLSA. RLSA has a simple structure which is easy to fabricate and with its high gain and high-power capability this make it a possible candidate for wireless power transfer.

The uniformity in the aperture field excitation is crucial for general array antennas, including RLSAs. The degradation in the aperture field excitation can contribute to the impairment of signal to interference ratio in short range communication systems as discussed in the previous chapter, as well as a reduction in wireless power transmission [13]. A key to achieve the uniform aperture excitation in the RLSA is the design of the coupling element. Conventionally, a straight cross-slot [9], [12], was used to excite the rotating mode in the radial waveguide of the RLSA. The quality of the uniform excitation is proportional to the amplitude ripples of the excited rotating mode in the ϕ direction. A dog-bone cross-slot was proposed in [14] to reduce the amplitude ripple of field distribution in the ϕ direction in the radial waveguide.

In this chapter, we propose the design methodology of a dog-bone cross slot using eigenmode analysis. We also demonstrate that the adoption of dog-bone cross slot in RLSAs improves the power transmission and amplitude ripples. Our target of this study is to enhance the transmission and reduce the transmission ripples for short-range transmission. The quantitative comparison with other works will be given at the end of this chapter. This study utilizes 5.8 GHz band, the industry science and medical (ISM) band.

3.2 Transmission Power Estimation

In most applications of wireless power transfer, the efficiency of the transmitted power is determined by four major parts [15]: 1) the conversion of d.c. power into microwave power, 2) a Tx antenna to convert the microwave power into a narrow beam, 3) a segment of space in which the microwave power is transmitted, and 4) the absorption and conversion of microwave power back

into d.c. power at the point of reception. The high power transmission was not possible not until the sudden ability to generate substantial amounts of power at microwave frequencies acquired during the World War II. Later on the efficient conversion of d.c. power into microwave power was realized. The reception part resides in a rectanna (rectifying antenna) which is the incorporation of an antenna and conversion circuit. To improve the efficiency of the rectanna, a recent work [12] proposed a Rx antenna to be combined with a microwave-to-d.c. converter. Even though the rectanna has normally been the predominant component limiting the transmission efficiency of the whole system, we will not include the conversion circuit into consideration. Transmission power or efficiency mentioned in this study concerns only the amounts of microwave power fed to the Tx antenna, transmitted through space, and received by the Rx antenna.

The power could theoretically be transmitted over any distance with nearly 100% [16] though less efficiencies were often realized in most applications due to constrains over frequencies, antenna sizes, and distances. Even so the idea to achieve high transmission power is to focus most of the power in the main beam and allow this beam to be fully absorbed by the receiving antenna, which is exactly the same idea as in the beam-type. This can be achieved by using the large size antenna. To prevent the divergence of the beam reception must be in the near-field region. Therefore, if one want to send power over a long distance, it is unavoidable to increase the antenna size. Though the antenna size can be reduced by using higher frequencies, we must keep in mind that high attenuation is to be expected at higher frequencies.

The equation 1 in [17] gives a simple way to estimate the power percentage received by the Rx antenna. By infinitesimal dipole approximation, the transmission percentage between two identical RLSAs directly aligned [13] is shown in Fig. 3.1. It should be emphasized that the transmission result using infinite dipole approximation effectively removes the influence of multiple reflections between Tx and Rx. The blue line represents the rotational excitation in which the phase value varies with in the ϕ direction; This excitation gives a conical beam pattern. The red line indicates the uniform excitation which realizes a pencil beam pattern. For this excitation it can be seen that over 60% of the power can be transmitted up to the distance of 1 m. For this reason, RLSA could be a promising candidate for short-range wireless power transfer.

Fig. 3.2 shows the simulation result of the transmission between two RL-

SAs up to 30 cm. The blue line shows the same result as in the uniform case of Fig. 3.1 while the red line show the simulation result obtained by HFSS. In this case, transmission ripples caused by multiple reflections can be observed. This characteristics, though inevitable and undesirable for the application, can be suppressed to a certain degree by improving the uniformity in the excited aperture field. The design and improvement of the uniformity of the aperture field distribution will be discussed in the following sections.

3.3 Antenna Configuration

In this work, we adopted the dog-bone cross-slot in the feeding part while the previous work used the straight cross-slot. The proposed RLSA is composed of two parts: 1) feeding part 2) radiating part, as shown in Fig. 3.3. The feeding part is composed of an air-filled rectangular feeding waveguide and an air-filled dog-bone cross-slot. The radiating part is composed of a poly tetra fluoro ethylene (PTFE)-filled parallel plate waveguide and an array of radiating slots is etched on the top of it. PTFE has a dielectric constant of 2.16 and a loss tangent of 0.001. The feeding waveguide and the lower layer of the parallel plate waveguide are of aluminum with bulk conductivity of 3.8×10^7 S/m. The upper plate is of copper with bulk conductivity of 5.8×10^7 S/m.These dielectric constant and conductivity are used in the analysis.

A coaxial feeder is used to excite TE_{10} in the rectangular feeding waveguide. Then, TEM in the rotating mode is excited by the dog-bone cross-slot in the radial (parallel plate) waveguide. Coupled with the rotating mode TEM inside the radial waveguide, slot pairs radiate a pencil beam pattern.

The antenna frame including the feeding part was fabricated by metal etching. The radiating part from the PTFE layer to the radiating slots was fabricated by printed circuit board (PCB). The feeding part and the radiating part are stacked and held together using screws.

3.4 Antenna Design

In this section, we address the design methods of this RLSA. The feeding and radiating parts were designed separately in subsection 3.4.1 and 3.4.2 respectively. The complete antenna structure is resulted from the combination

between the feeding part and the radiating part. In this study, we focus on the design of a dog-bone cross-slot in the feeding part.

3.4.1 Design of the Feeding Part

The reason why the dog-bone cross-slot is adopted is that it can realize a better rotating mode than the straight cross-slot with similar dimensions because a dog-bone slot has wider half beamwidth than that of a straight slot. More precisely, two crossed infinitesimal magnetic dipoles with excited phase difference of 90° realize an ideal rotating mode since the half beamwidth of an infinitesimal magnetic dipole is 90°. However an actual crossed magnetic dipole cannot give uniform amplitude distribution in the ϕ direction because the slot length is finite. Two straight slots for a conventional crossed slot can be regarded as half-wavelength dipoles with the half power width of 78°. The magnetic current in the straight slot decays smoothly near its edges. On the other hand, the magnetic current in the dog-bone slot decays rapidly near its edges because the two components flowing in opposite directions in each edge cancel out. Since the effective length of the dog-bone slot is shorter than that of the straight slot, the beamwidth of the dog-bone slot is wider than that of the straight slot. As a result, the performance of the dog-bone cross-slot is closer to that of the two crossed infinitesimal magnetic dipoles with excited phase difference of 90° [14]. Here, the design of the dog-bone cross-slot is based on electromagnetic simulator (HFSS)-based eigenmode analysis.

We start the design with the initial model shown in Fig. 3.4; a single dog-bone slot over a rectangular cavity with prefect electric conductors (PEC) in their walls and an infinite parallel plate waveguide over the dog-bone single-slot (a rectangular terminated by impedance boundaries since all the power to the parallel plate waveguide will be designed to radiate by the radiating slot pairs). The initial dimension of the dog-bone slot is determined in [14] using method of moment (MoM). By properly scaling the length of the dog-bone slot (while keeping the ratio between the length of the center part of the dog-bone slot and the length of the edge parts [14]), the resonant frequency can be controlled.

A dog-bone cross slot will be created by combining two dog-bone slots perpendicularly. Theoretically, the length of one slot has to be shorter and the length of the other slot has to be longer than the resonant length at the design frequency to excite rotating modes. Furthermore, the design of two dog-bone slots is required to satisfy the bandwidth condition as follows,

$$\begin{aligned} \frac{f_1 + f_2}{2} &= f_c \\ f_1 - f_2 &= \frac{1}{2}(\frac{f_1}{\Delta Q_1} + \frac{f_2}{\Delta Q_2}), \end{aligned} \tag{3.1}$$

where f_1 and f_2 are the resonant frequencies resulting from combing two dog-bone slots. ΔQ_1 and ΔQ_2 are the quality factors of the respective frequencies. f_c is the center frequency. Equation 3.1 can be easily derived from the relation between bandwidth and quality factor in a resonant circuit. Fig. 3.5 shows the model of a dog-bone cross-slot by combining two dog-bone slots on the PEC-wall rectangular cavity. The distance from the slot to the right PEC-wall of the rectangular cavity is set to be a quarter guided wavelength to include the effect of the PEC-wall to the slot in the actual antenna. The distance from the slot to the left PEC-wall of the rectangular cavity is set to be a half guided wavelength, so that the resonance of the rectangular cavity should be avoided to achieve only the resonance of the slot. In this model, the dog-bone cross slot has two resonant frequencies at 5.68 and 6.05 GHz with quality factors of 15.23 and 19.26, respectively; these parameters satisfy equation 3.1. The eigenmode is typically a real-valued function in a loss-less case. That at the resonant frequency of 6.05 GHz is demonstrated in Fig. 3.6a-3.6b, which is excited only by the shorter dog-bone slot because the mutual coupling between the two dong-bone slots is negligibly small.

We apply an impedance boundary equal to the wave impedance of TE_{10} mode of the feeding waveguide in the eigenmode analysis as indicated in Fig. 3.5. The propagation from the dog-bone cross-slot to the feeding and parallel plate waveguides is reciprocal to the propagation from the feeding and parallel plate waveguides to the dog-bone cross slot. As a result, the eigenmode becomes a complex-valued function, so the rotating mode is observed in the parallel plate waveguide at 6.05 GHz (the resonant frequency) in Fig. 3.7a-3.7b. Finally, the overall size of the dog-bone cross-slot needs to be adjusted (scaled) so that the operating frequency is shifted to 5.8 GHz. We adjust the angle of the dog-bone cross-slot to minimize the amplitude ripples of E-field in the ϕ direction in the parallel plate (radial) waveguide. The reflection is minimized by adjusting the distance between the dog-bone cross-slot and the shorted end of the feeding waveguide. Almost the adjustments of the parameters are done by the eigenmode analysis while only the small adjustments on the circumferential amplitude ripples and the reflection are done by the

excitation analysis. An advantage of using eigenmode analysis is that we do not need to extract the excited rotating mode field to verify phase differences before and after combining the slots. In the eigenmode analysis, we instead works on eigenfrequencies which are more efficient and less time-consuming.

To this end, we summarize the design procedure of the feeding part as follows,

1. Design two dog-bone slots in eigenmode analysis so that their eigenvalues (frequencies and their corresponding quality factors) satisfy equation 3.1.

2. Combine the two dog-bone slots perpendicularly into a dog-bone cross-slot as shown in Fig. 3.5.

3. Adjust the overall length of the dog-bone cross-slot to achieve the resonant frequency at the center frequency.

4. Optimize the angle of dog-bone cross-slot (initially at 45 deg.) to minimize the amplitude ripples (this step can be done either in eigenmode or excitation mode).

5. Optimize the distance between the dog-bone cross-slot and the short end to the feeding waveguide to minimize reflection.

6. Optimize the height of the feeding waveguide to minimize reflection.

In the final model, we also introduced an iris in the rectangular feeding waveguide to further reduce the reflection.

The parameters of the dog-bone cross-slot are given as follows; the length of the center parts is 10.40 mm and 9.18 mm, the length of the edge parts is 3.88 mm and 3.42 mm, the angle of the slot is determined to be 48 degree, and the slot thickness is 1.50 mm. The distance to the short end of the feeding waveguide is 25.75 mm (approximately a quarter of the feeding guided wavelength), see Fig. 3.8.

According to Fig. 3.9, Fig. 3.10 shows the plots of amplitude ripples of E-field in the ϕ direction in the parallel plate waveguide for the straight and dog-bone cross-slots. By using the dog-bone cross-slot, the maximum of amplitude ripples at 5.8 GHz is 1.8 dB while that using the straight cross slot is 2.5 dB. The plot of amplitude ripples of the dog-bone cross slot for various frequencies is presented in Fig. 3.11. The amplitude ripples are below 6 dB within the frequency band of [5.7, 5.9] GHz

3.4.2 Design of the Radiating Part

Method of Moment (MoM) is used to design slot pairs in the radiating part. Fig. 3.12 shows an equivalent model used in MoM to analyze a radiating element. The slot pairs are arranged in linear fashion. Periodic boundary condition (PBC) includes the coupling effect from the neighboring slot pairs in the full array model. Plane wave incident is excited at port 1. The full array model is the result of adding the element model in radial direction as shown in Fig. 3.13. The key parameters in slot pair design are indicated in Fig. 3.14. the radiation power of each slot pair can be controlled by changing slot length $l_{s,i}$ where i indicates the ordering number of a slot pair;in this case $i = 4$ represents the slot pairs in the most innermost circle and $i = 1$ represents the slot pairs in the outermost circle. The slot spacing $\Delta x_{s,i}$ can control the reflection while axial ratio can be effectively adjusted by the slot spacing $\Delta y_{s,i}$. The distance between the center of each slot in a slot pair ($\sqrt{(\Delta x_{s,i})^2 + (\Delta y_{s,i})^2}$) is approximately a quarter of the guided wavelength. By adjusting $l_{s,i}$, $\Delta x_{s,i}$, and $\Delta y_{s,i}$, the uniform amplitude excitation and reasonable reflection can be realized while the spacing between adjacent slot pairs in Fig.3.14 is approximately a guided wavelength in order to realize the uniform phase excitation. More detailed explanations are provided in [18], [19]. The parameters for radiating slot pair are shown in Table 3.1.

i	$l_{s,i}$ (mm)	$\Delta x_{s,i}$ (mm)	$\Delta y_{s,i}$ (mm)	$\rho_{s,i}$ (mm)	n
1	19.99	8.54	12.46	115.90	36
2	18.47	8.95	11.76	88.70	27
3	17.80	8.96	11.0	57.10	18
4	16.67	8.96	11.0	26.36	8
Note: n is the number of slot pair in circle					

Table 3.1: Designed parameters of the slot pairs

3.5 Results

In this section, we discuss the antenna performance and their transmission which include the results of a standalone RLSA and transmission between two RLSAs. Before proceeding into the details, it is advisable to explain the parameters for benchmarking of performance between competing wireless

power beaming technologies. Selected measurable parameters are shown in Table 2 of [20]. A few examples is the maximum dimension and weight of the Tx or Rx antennas. Calculated parameters of potential interest are also shown in Table 3 of [20]. What dictates the priority of these parameters depend on applications.

3.5.1 Antenna Performance

A Prototype RLSA is shown in Fig. 3.15. The antenna diameter is 270 mm. For the comparison purpose, the RLSA fed by the dog-bone cross-slot and that fed by the straight cross-slot have the same design except for the types of coupling slots in their feeding parts. Fig. 3.16a-3.16b show plots of the reflections. The black lines indicate the simulated reflections. The reflections of both cross-slot types are below -25 dB;in fact, the RLSA using the straight cross-slot can achieve better reflection than that using the dog-bone cross-slot, [14]. The bandwidth of both antennas are approximately 5% of the center frequency as suggested by the simulation. Though 5% bandwidth is considered small for data communication, it is sufficient for power transmission. The red and blue lines are the experimental results of the same design (for Tx and Rx uses). Large reflections in the measured results and significant differences between simulation and measurement are observed in Fig. 3.16a-3.16b. A further investigation using a time-domain technique suggested that the predominant reflection came from the coaxial-to-waveguide connection. Assuming that there is a fabrication error at the length of the inner conductor, we arrived at the plots shown in Fig. 3.17a-3.17b, in which the black-lines represent the simulated reflections given that the length of the inner conductor is 0.4 mm and 0.2 mm shorter than the designed value for the dog-bone and straight cross-slot cases respectively. As a result, the simulation and measurement results are in good agreement. Plots of directivity and realized gain for the RLSA with the dog-bone cross-slot are shown in Fig. 3.18a, 3.18b, and 3.19. Since we are interested in near-field applications, it is preferable to examine the aperture field distribution. Fig. 3.20 shows a near-field distribution comparison between the dog-bone and straight cross-slot cases in which slightly better uniformity for the dog-bone cross-slot feeding is suggested near the center of the RLSA. Comparatively, plots of the measured aperture field distribution of RLSAs with each feeding type are given in Fig. 3.21a-3.30b. the plots confirmed the realization of the right-handed circular polarization and suggested similar performance for

both feeding types in terms of the uniformity of the aperture field excitation. Moreover, the degradation in the uniformity of the field is gradually noticeable as the frequency is shifted from the center frequency. This result is to be expected as the amplitude ripples of the rotating mode excited by a cross-slot become larger in proportion to the amount of the frequency shift, see subsection 3.4.1.

3.5.2 Transmission

As previously mentioned, there are several parameters for benchmarking of performance between competing wireless power beaming technologies; one of these parameters is transmission efficiency in relation to the distance. Undoubtedly, it is more useful to show the overall efficiency which accounts for all efficiencies associated with each system part, see section 3.1. Still our current priority is the efficiency only associated with the transmission and reception of antennas. It should be noted again that a microwave-to-d.c. conversion circuit in the reception part will not be considered. Two different RLSAs were used for reception: 1) a prototype identical to the Tx antenna and 2) a prototype of the 8-port-microstrip-line fed RLSA [12]. Since we are aiming for the short-range application, our designed RLSA might be able to cover approximately up to 2.6 m considering its size. We however discuss transmission distances up to 30 cm due to limitations of the antenna simulation and experiment.

- *Rx antenna is identical to the Tx antenna*

  Fig. 3.31 shows plots of the transmission over distances 50 mm to 100 mm. The red and black dashed lines represent the transmission of the RLSA fed by the dog-bone cross-slot and that fed by the straight cross-slot respectively while the blue and green line represent their corresponding measured transmission. The simulation results suggest the similar average transmission level between both feeding types, but the result of the dog-bone cross-slot has smaller maximum value of the amplitude ripples (about 1.5 dB) than that of the straight cross-slot. the experimental results show a similar behavior. However, the difference between the simulation and measurement results are significant. Plots of the reflection are shown in Fig. 3.32 in which S_{11} and S_{22} are referred to the reflections in the Tx and Rx antennas respectively while

the dashed-lines indicate the simulation results. The measured reflections point out a large degradation in the prototype antennas. Similar to subsection 3.5.1, we assumed an offset value for the length of the coaxial inner conductor. The black lines in Fig. 3.33-3.34 show the simulation results of the RLSA using the dog-bone cross-slot feeding assuming the length of the coaxial inner conductor is 0.4 mm shorter than the designed value. Fig. 3.33 and 3.34 suggest good agreement between the simulated and measured results. In the same manner, Fig.3.35-3.36 provide the simulation results of the RLSA using the straight cross-slot feeding with the introduction of an error offset. Though in the straight cross-slot case we have better agreement between the simulation and measurement, somewhat large differences are indicated especially in the plots of reflection. Finally, a comparison between the dog-bone and straight cross-slots is given in Fig. 3.37. The measurement result suggests about 2 dB and 4 dB maximum amplitude ripples for the RLSA fed by the dog-bone cross-slot and that fed by the straight cross-slot respectively. Furthermore, the RLSA using the dog-bone cross-slot feeding has approximately 2 dB higher in the average transmission level. It is expected that the differences in the transmission characteristics of each feeding type gradually disappear for a larger transmission distance because of the divergence of the radiated fields. The transmission measurement scenario is shown in Fig. 3.38

- *Rx antenna is the 8-port-microstrip-line fed RLSA*

  The 8-port-microstrip-line fed RLSA are designed to operate with a microwave-to-d.c. conversion circuit for reception. By dividing the receiving power and distributing it, the conversion efficiency of the conversion circuit can be improved, [12]. Fig. 3.39a-3.39b show plots of the transmission between the one-port RLSA (Tx) and the 8-port-microstrip-line fed RLSA over distances from 50 mm to 100 mm. The dashed lines represent the measured results while the solid lines show the simulation results. each port of the 8-port-microstrip-line fed RLSA is labelled by number 1 to 9 and port 9 is the input port of the one-port RLSA. It should also be noted the pairs of s-parameter, (S_{19}, S_{59}), (S_{29}, S_{69}), (S_{39}, S_{79}), and (S_{49}, S_{89}), were included in the same figures because they are expected to give the same performance;this is due to the port configuration and their symmetries in the antenna. According to the plots in Fig. 3.39a-3.39b, it is evident that the amplitude

ripples of both simulation and measured result of the RLSA fed by the dog-bone cross-slot are smaller than those of the straight cross-slot fed RLSA while their respective average transmission levels are approximately the same. A plot of the total receiving power, i.e. $\sum_{i=1}^{8} \mid S_{i9} \mid^2$, is given in Fig. 3.40. The red and black dashed lines are the simulation results of the RLSA using the dog-bone cross-slot feeding and the straight cross-slot feeding respectively. Similarly, the blue and green solid lines show the the measured results of the dog-bone cross-slot case and straight cross-slot case. The simulation result in Fig. 3.40 suggests the (2 dB) smaller maximum value of amplitude ripples and a slightly higher average transmission level for the dog-bone feeding type. The measurement is also in agreement with the simulation;however, the difference in the average transmission levels is slight (1 dB) higher in the measurement and the difference in the maximums of amplitude ripples is (1 dB) higher in the simulation. As previously mentioned, the differences in the transmission characteristics of each feeding type become smaller for a larger transmission distance due to the divergence of the radiated fields. The transmission measurement scenario of this case is illustrated in Fig. 3.41

3.6 Concluding Remarks

An RLSA was proposed for short-range microwave power transmission. The transmission configuration is line of sight propagation and features similar RLSAs for transmitting and receiving. The transmission distance is in the near-field region based on the beam-typed technique; this is to prevent the divergence of the beam and therefore the reduction in transmission efficiency. The dog-bone cross-slot was adopted, instead of the conventional straight cross-slot, to reduce the amplitude ripples of the TEM rotating mode excited in the parallel plate (radial) waveguide of the RLSA and hence improve the uniformity of the aperture field distribution. The design method of the dog-bone cross-slot based on the eigenmode analysis was introduced. As a result, improvements of the transmission were confirmed by both simulation and experiment. The simulation result indicates approximately 66% transmission efficiency and 2 dB reduction in the transmission ripples in comparison to the straight cross-slot fed RLSA, while 61% transmission efficiency, which is 15% higher than the RLSA fed by the straight cross-slot, and

1.5 dB reduction in the transmission ripples were achieved in the experiment by the RLSA fed by the dog-bone cross-slot. Similarly, 60% transmission efficiency and 2 dB reduction in the amplitude ripples are suggested in the simulation by the RLSA using the dog-bone cross-slot feeding in the case of using the 8-port-microstrip-line fed RLSA. The measured result of the dog-bone cross-slot case shows approximately 51% transmission efficiency which is about 10% higher than that of the straight cross-slot feeding. The differences in the transmission characteristics of each feeding type become smaller for a larger transmission distance due to the divergence of the radiated fields. In other words, the improvements on the transmission of the RLSA using the dog-bone cross-slot would be insignificant compared to the transmission of the RLSA using the conventional straight cross-slot at a large transmission distance. The efficiency mentioned throughout this chapter only accounts for the transmission between the Tx and Rx antenna without the dc-to-microwave and microwave-to-dc conversion parts. In practical use, it is required to incorporate all the parts [15]; therefore, the design of the antennas, especially the Rx antenna, requires careful considerations on the microwave-to-dc conversion part [12]. Our future work will need to carefully consider the antenna design in response to the microwave-to-dc conversion part, precisely speaking rectanna. To this end, Table 3.2 shows comparisons to related works. Reported results for power beaming systems and demonstrations are historically inconsistent [20]; this makes comparison between different technologies difficult. [21] demonstrated helicopter power beaming using a ϕ3-m ellipsoid reflector antenna at an altitude of 15 m. Though the total transmission efficiency or Tx-Rx transmission efficiency are not clearly indicated, the efficiency of the rectanna was 55%. A similar demonstration was conducted in [22] using a ϕ4.5-m parabolic reflector antenna to power an airplane at an altitude of 150 m. In this work, the estimated beam efficiency [20] was 90%;therefore, the transmission efficiency should be lower than 90%. An ground-to-ground microwave power beaming experiment [23] using a similar antenna type with smaller size achieved 74% beam efficiency, i.e., the transmission efficiency was lower than 74%. [24] designed a 5.8-GHz patch array antenna for short distance WPT; 39.4% transmission efficiency at a distance of 40 cm was recorded in measurement. A study in [25] using a beam optimization technique to devise a 5.8-GHz active patch array antenna for the purpose of EV charging. The calculated and measured transmission results are 73% and 23% respectively. A similar technique was adopted in [26] for a 2.45-GHz patch array antenna. The simulation suggests about 79%

transmission efficiency.

Ref.	Antenna Type	Size [m^2]	Distance [m]	Efficiency [%]	Application
[21]	2.45-GHz ellipsoid reflector	$\pi(1.5)^2$	15	55(Exp. rectanna)	Helicopter powering
[22]	2.45-GHz parabolic reflector	$\pi(2.25)^2$	150	< 90(Cal.)	Airplane powering
[23]	2.45-GHz parabolic reflector	$\pi(1.5)^2$	42	<74(Exp.)	Power beaming
[24]	5.8-GHz patch array	$(0.21)^2$	0.4	39.4(Exp.)	Microwave power transfer
[25]	5.8-GHz patch array	$(1.4)^2$	2-10	73(Cal.) 23(Exp.)	EV charging
[27]	2.46-GHz RLSA	$\pi(0.36)^2$	-	-	Power beaming from airship
[26]	2.45-GHz patch array	$(0.5)^2$	1.2	79(Sim.)	Charging using drone
This work	5.8-GHz RLSA	$\pi(0.13)^2$	≤ 0.3	77(Cal.) 66(Sim.) 61(Exp.)	EV charging

Table 3.2: List of related works

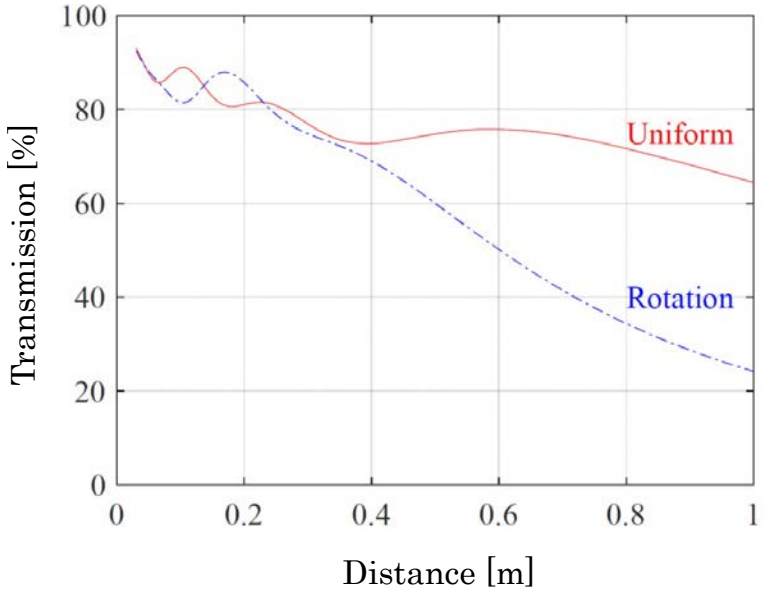

Figure 3.1: Plots of the calculated transmission between two identical RLSAs for various excitation modes

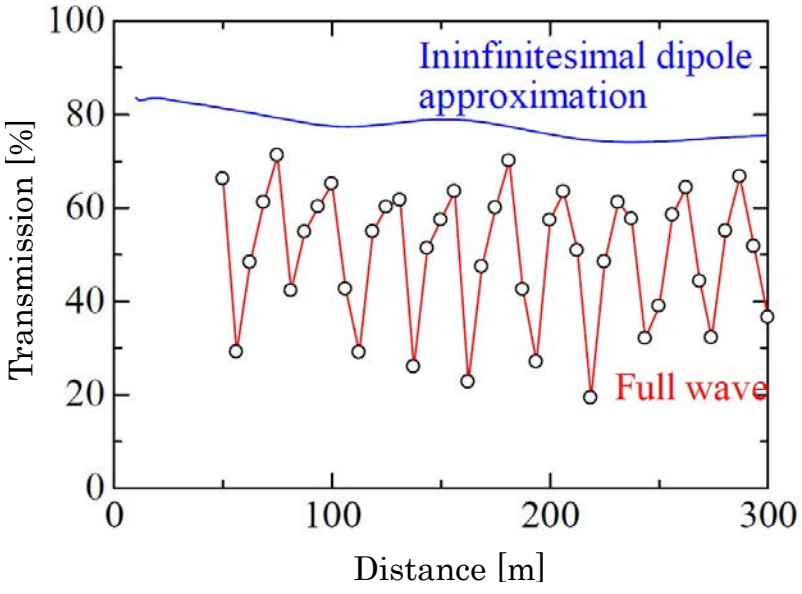

Figure 3.2: Plot of the calculated transmission between two identical RLSAs for various distance

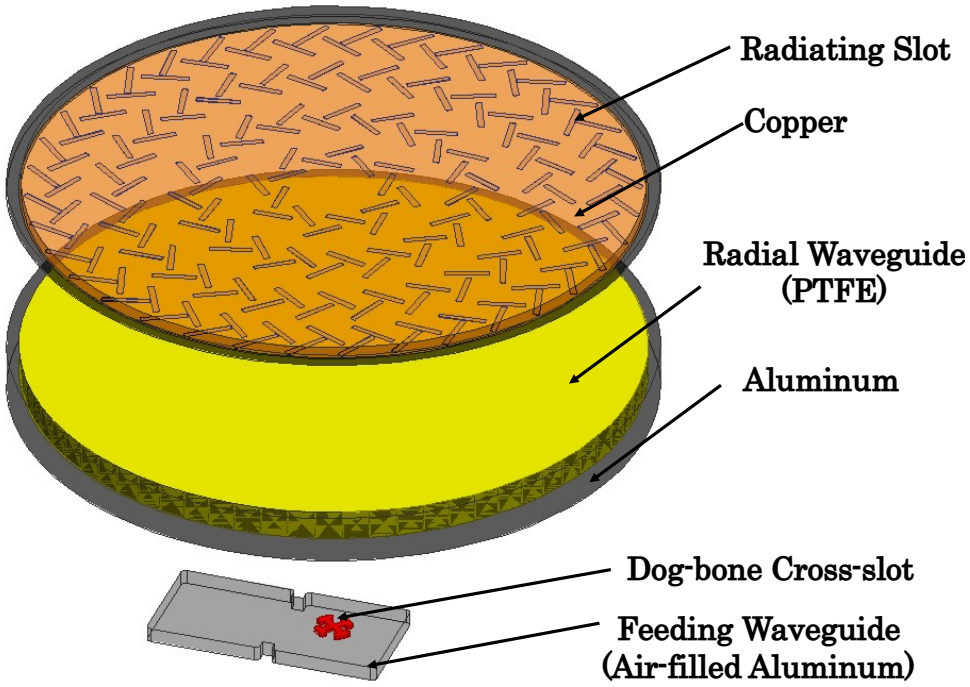

Figure 3.3: Antenna structure

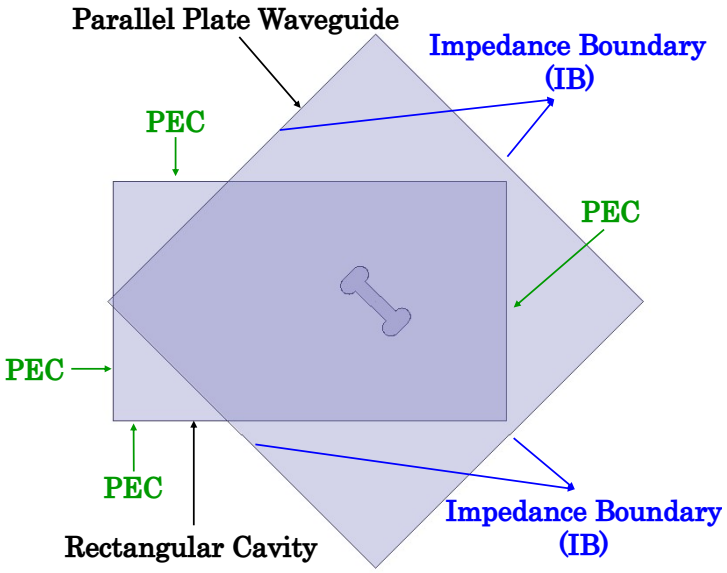

Figure 3.4: Single dog-bone slot model for eigenmode analysis

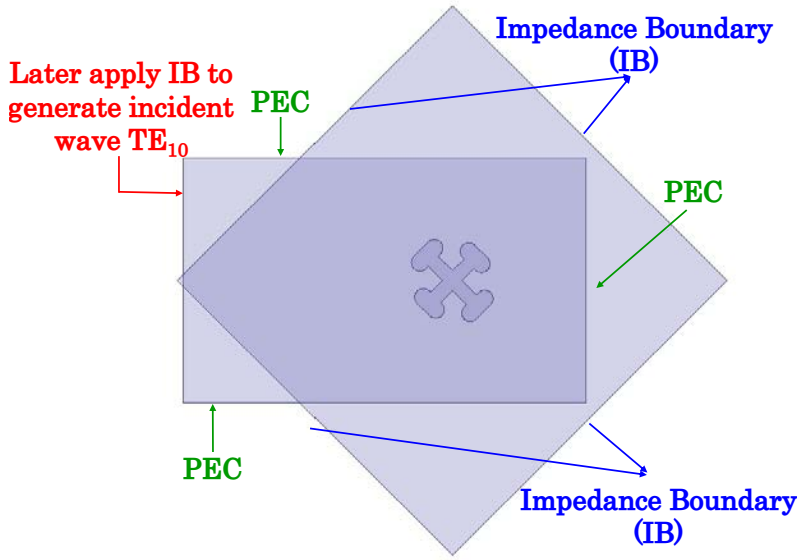

Figure 3.5: Dog-bone cross-slot model for eigenmode analysis

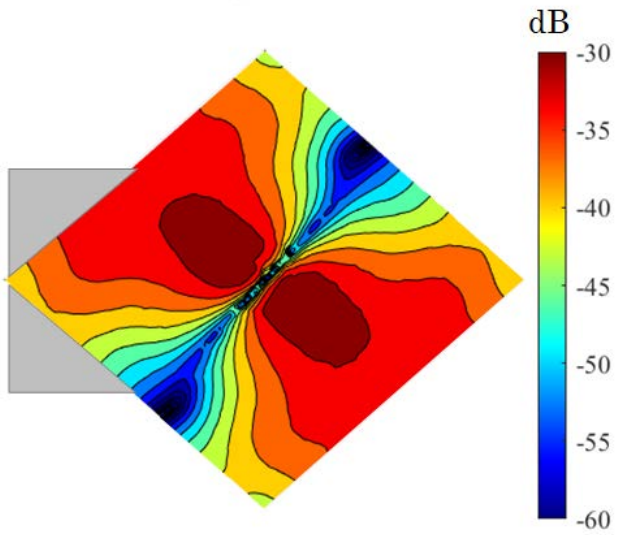

(a) Amplitude distribution

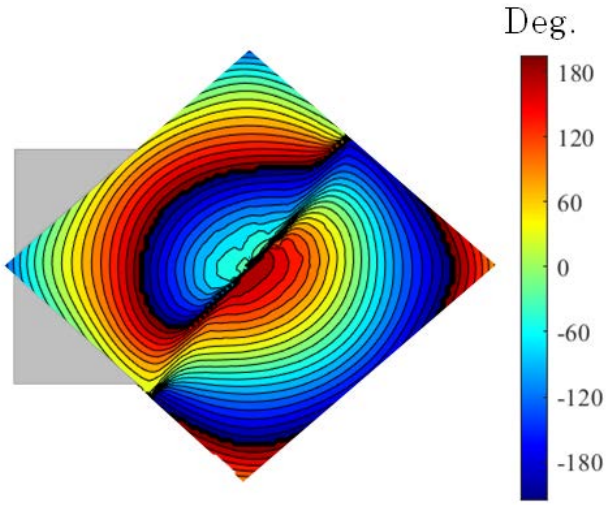

(b) Phase distribution

Figure 3.6: Field distribution inside the parallel plate waveguide in Fig. 3.4

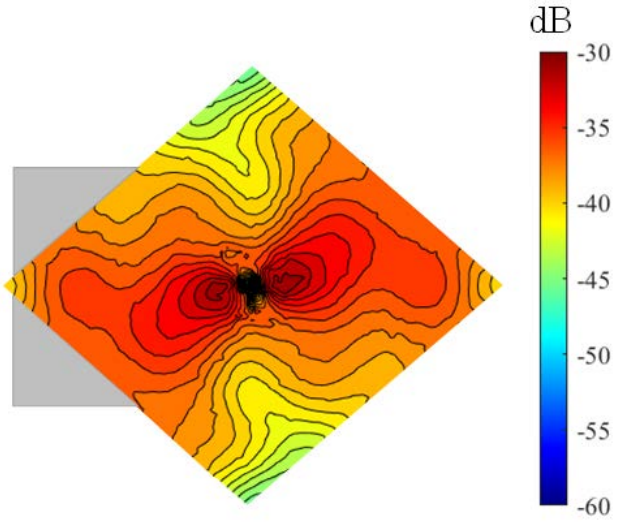

(a) Amplitude distribution

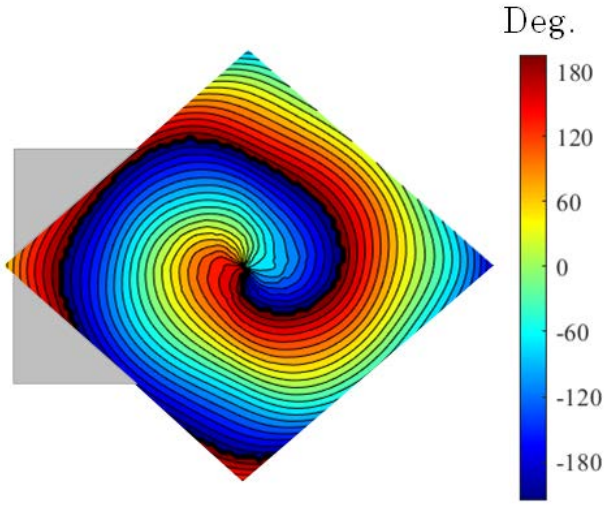

(b) Phase distribution

Figure 3.7: Field distribution inside the parallel plate waveguide in Fig. 3.5

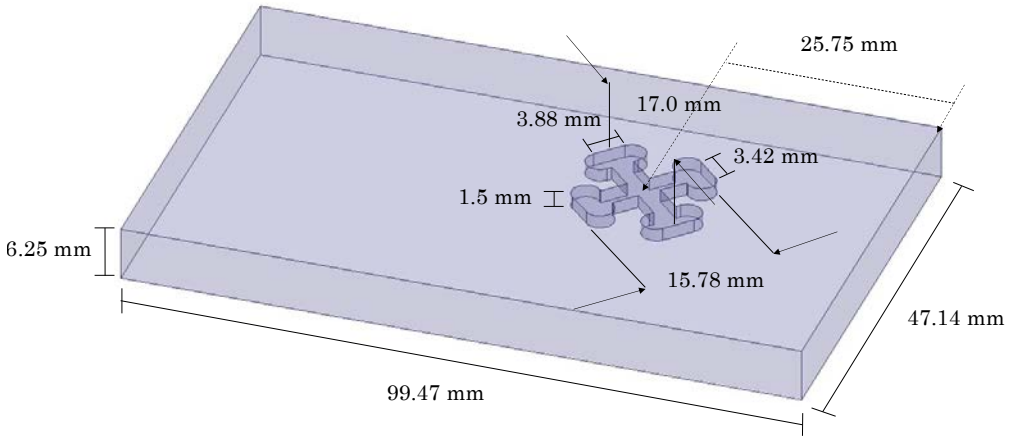

Figure 3.8: Dimension of the feeding part

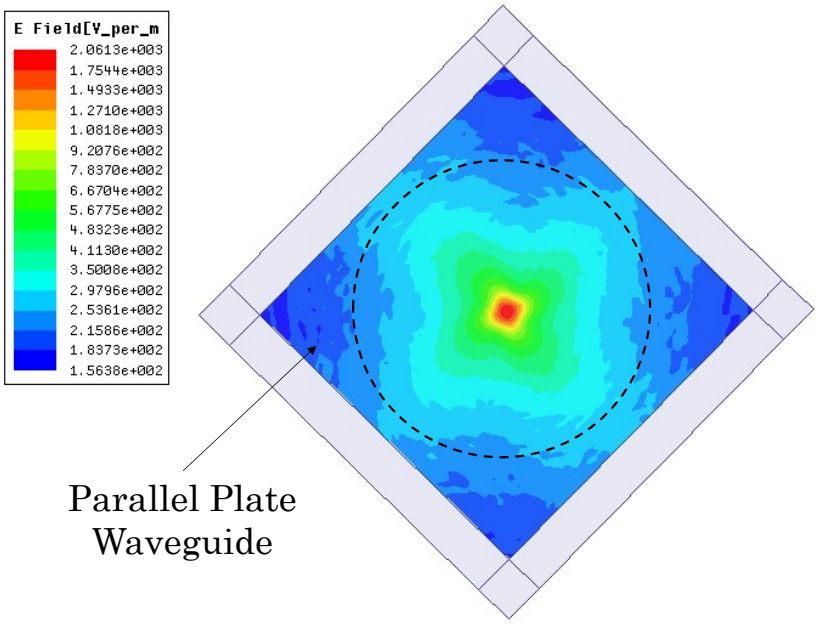

Figure 3.9: Field distribution excited by a cross-slot inside the parallel plate waveguide

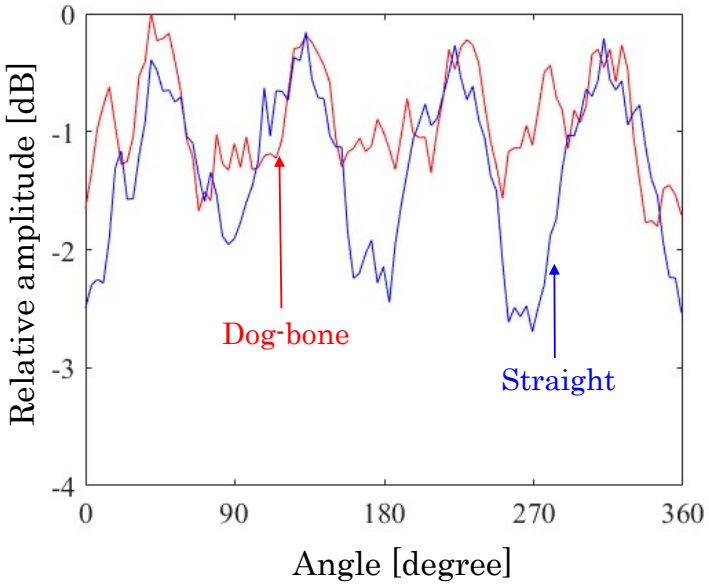

Figure 3.10: Plots of magnitude of E-field along black-dashed line in Fig. 3.9

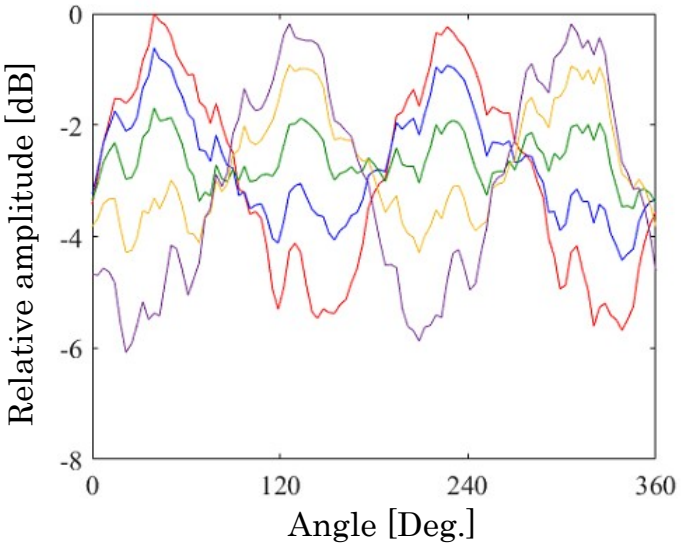

Figure 3.11: Plots of the field along the ϕ direction inside the parallel plate waveguide for various frequencies

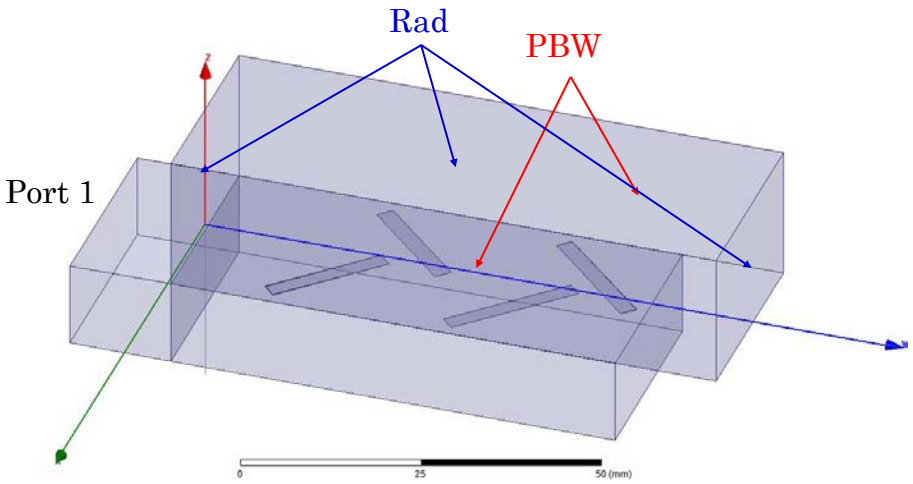

Figure 3.12: Analysis model for radiating elements

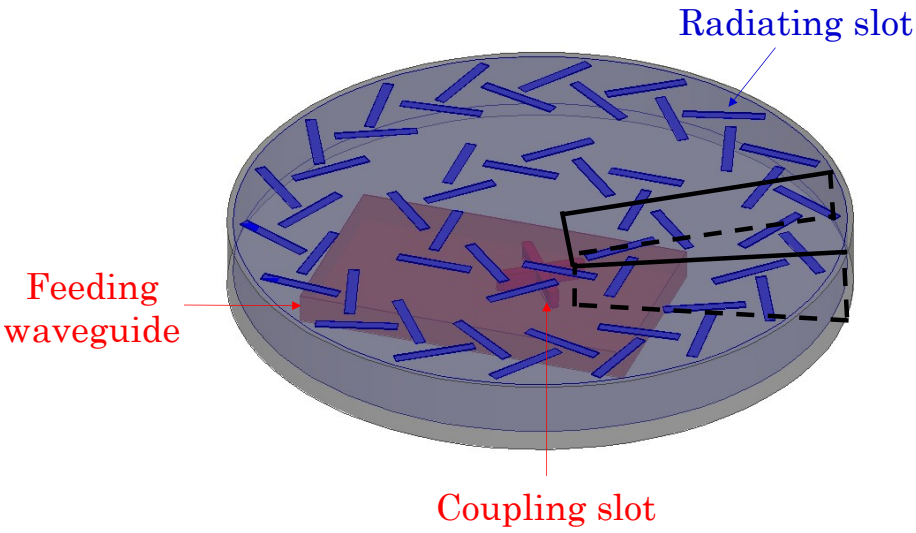

Figure 3.13: Complete radiating part

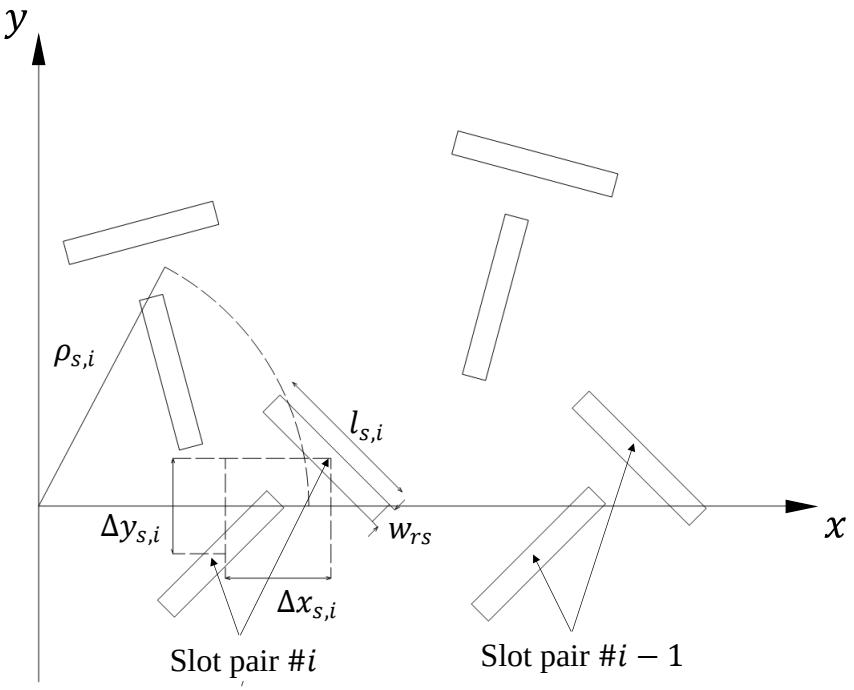

Figure 3.14: Parameters of radiating slot pairs

Figure 3.15: Prototype dog-bone cross-slot fed RLSA

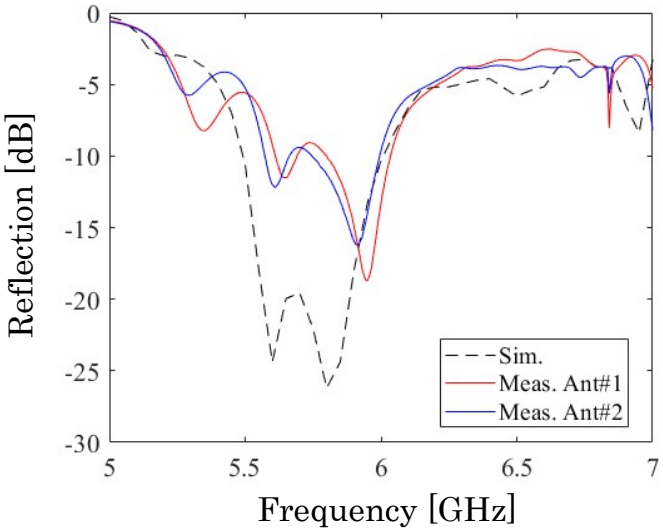

(a) Straight cross-slot

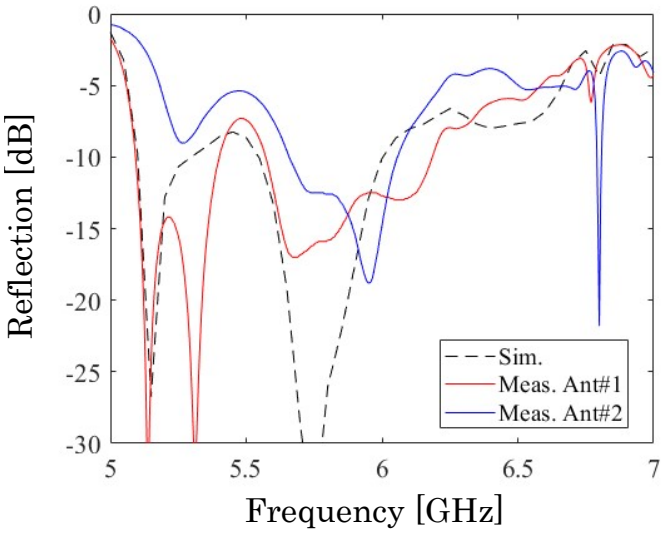

(b) Dog-bone cross-slot

Figure 3.16: Plots of the reflection of each feeding type

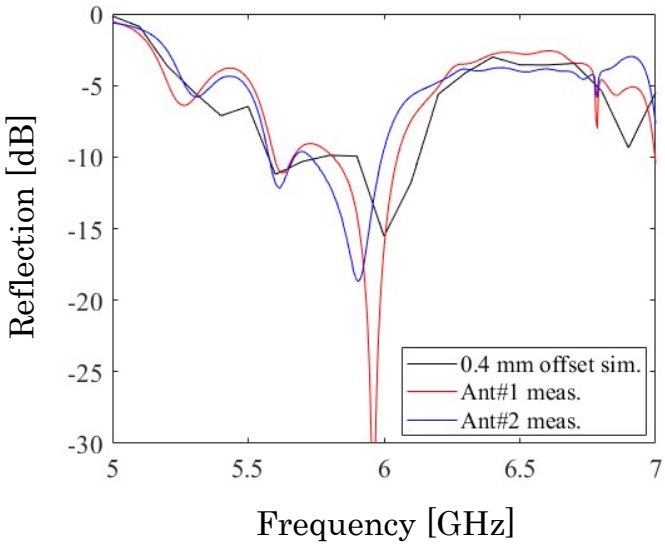

(a) Straight cross-slot

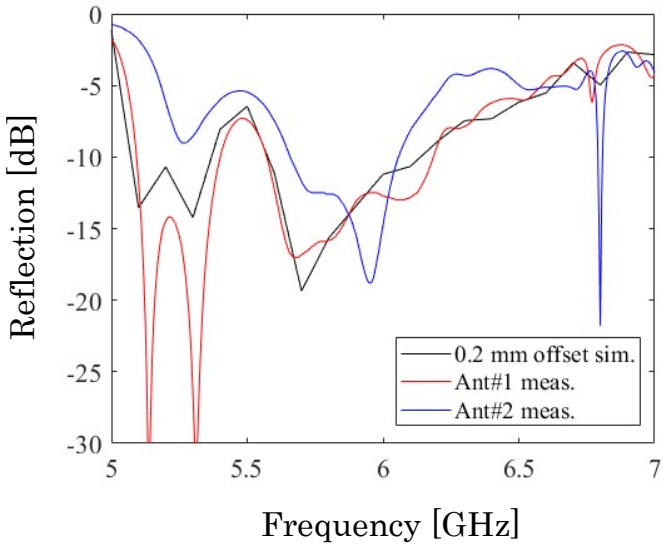

(b) Dog-bone cross-slot

Figure 3.17: Plots of the reflection of each feeding type assuming the fabrication error at the length of the coaxial inner conductor

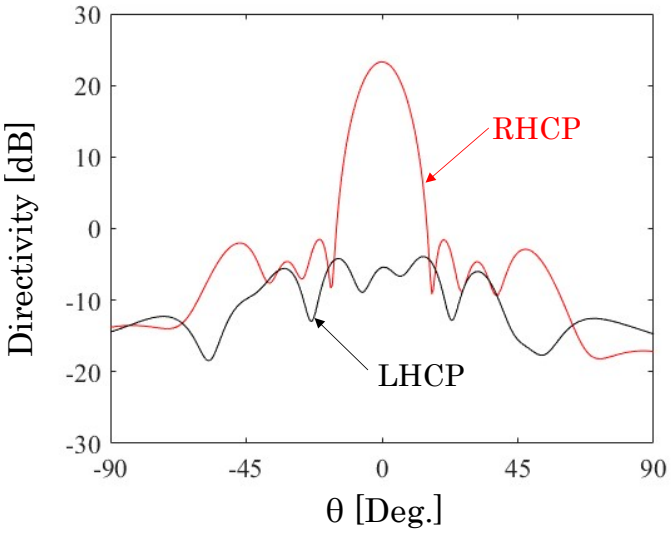

(a) $\phi = 0°$

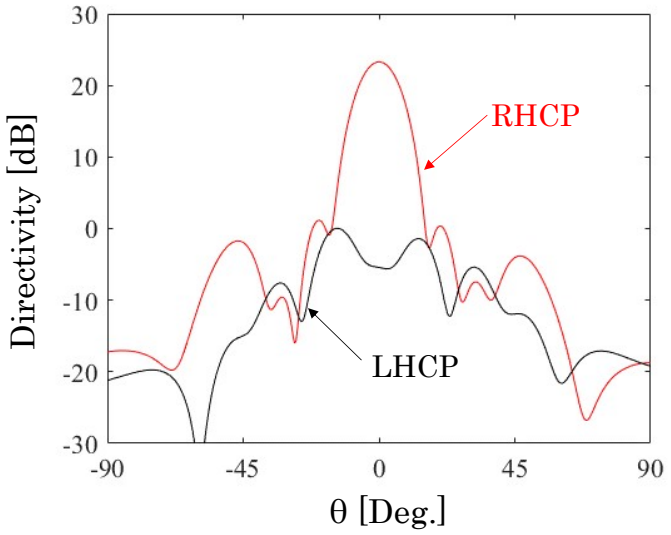

(b) $\phi = 90°$

Figure 3.18: Plots of simulated directivity of the RLSA fed by the dog-bone cross-slot

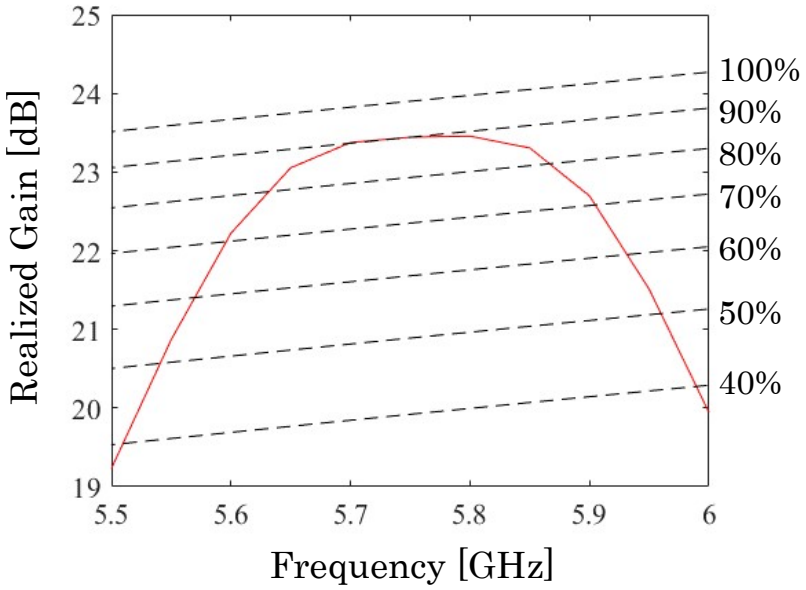

Figure 3.19: Realized gain

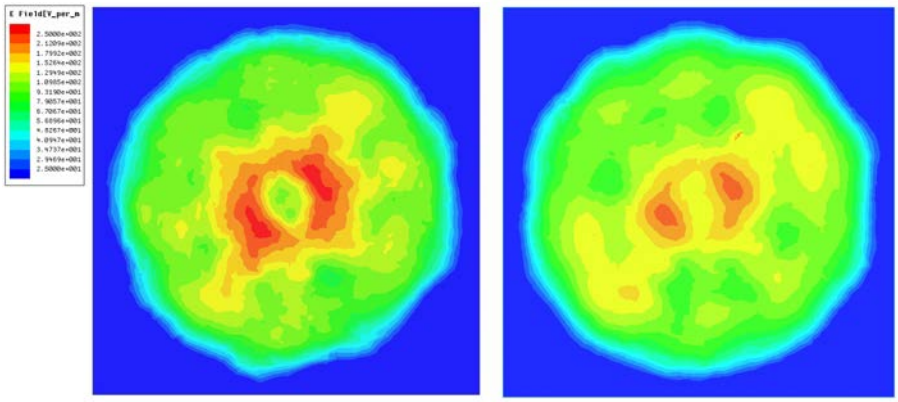

(a) Dog-bone (b) Straight

Figure 3.20: Simulated aperture field distribution for each feeding type

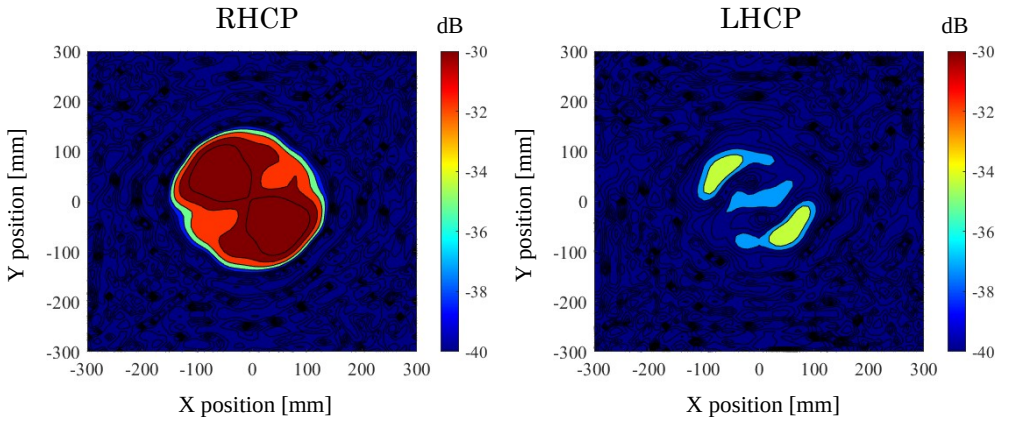

(a) Amplitude distribution

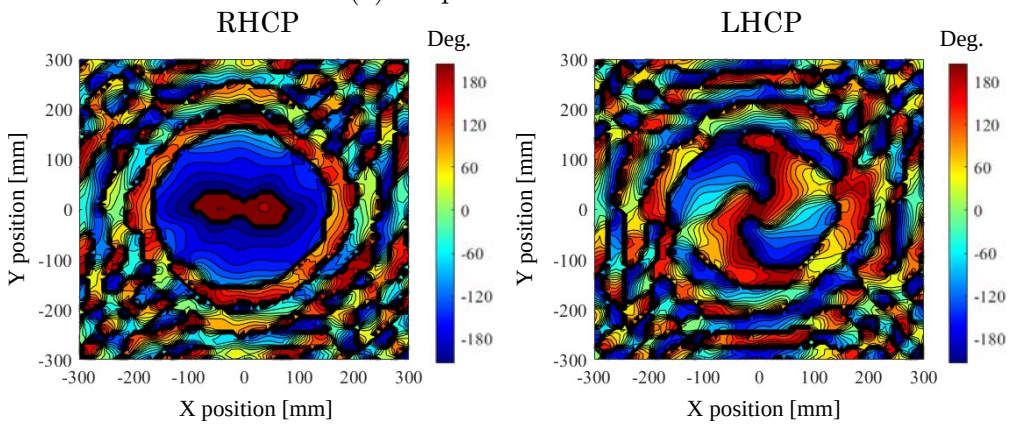

(b) Phase distribution

Figure 3.21: Measured aperture field distribution of the straight cross-slot feeding case at 5.6 GHz

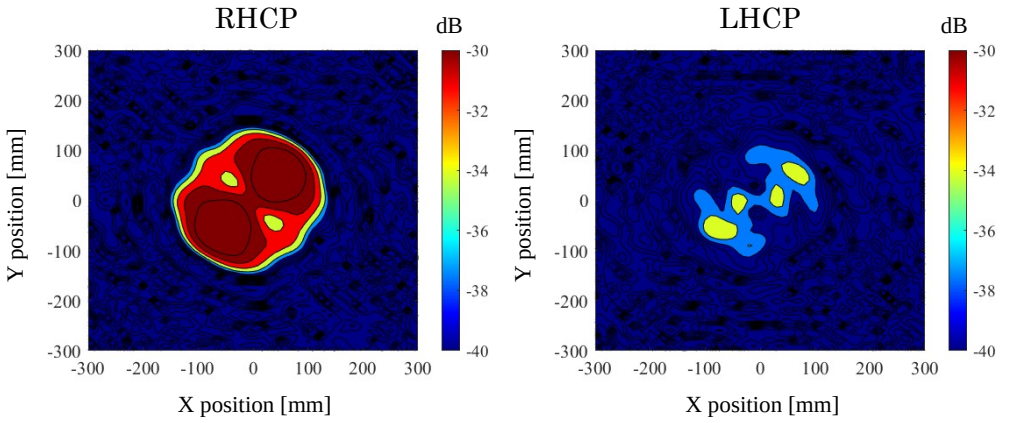

(a) Amplitude distribution

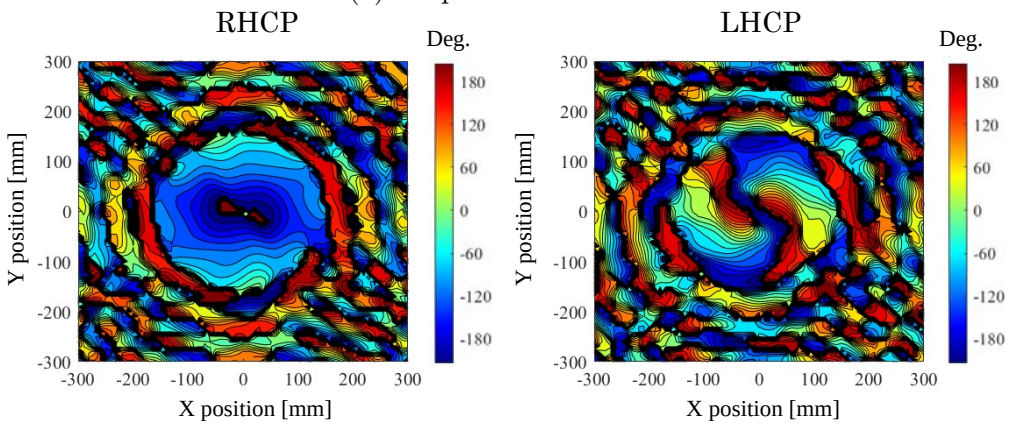

(b) Phase distribution

Figure 3.22: Measured aperture field distribution of the dog-bone cross-slot feeding case at 5.6 GHz

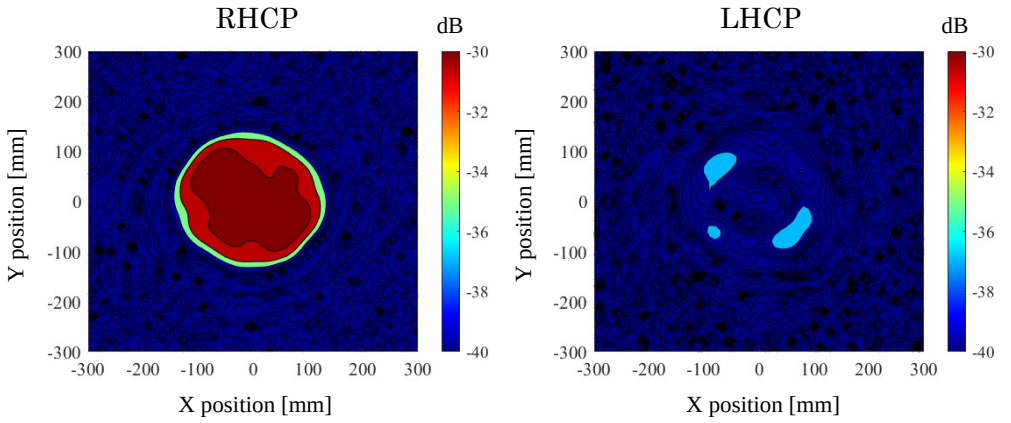

(a) Amplitude distribution

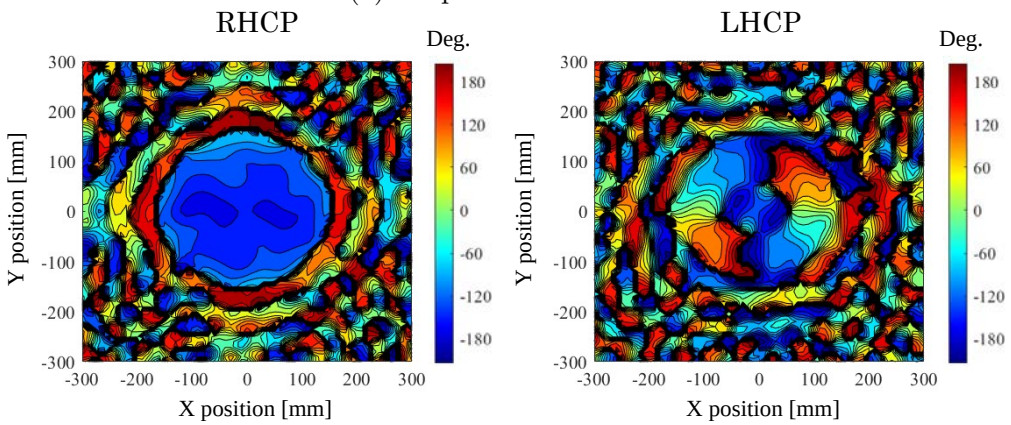

(b) Phase distribution

Figure 3.23: Measured aperture field distribution of the straight cross-slot feeding case at 5.7 GHz

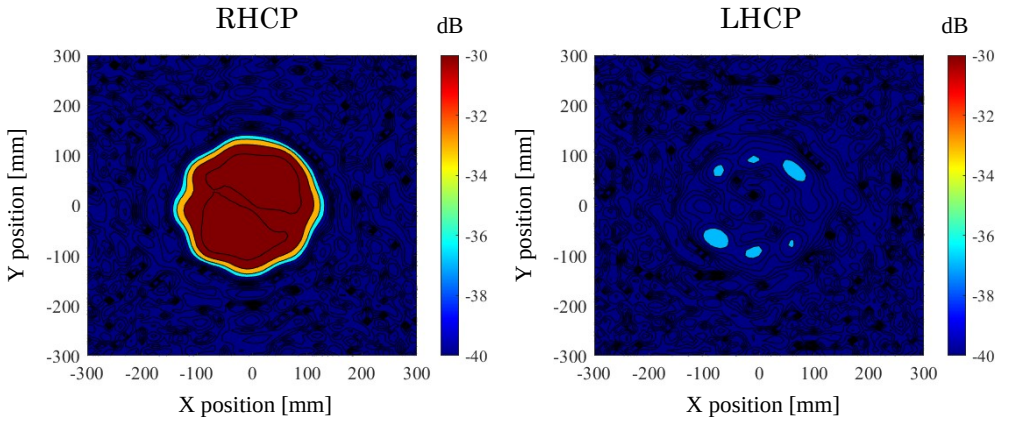

(a) Amplitude distribution

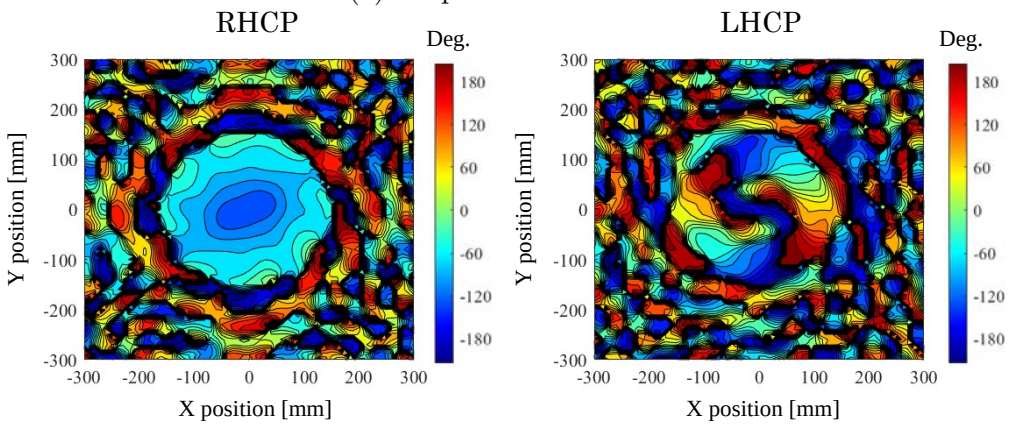

(b) Phase distribution

Figure 3.24: Measured aperture field distribution of the dog-bone cross-slot feeding case at 5.7 GHz

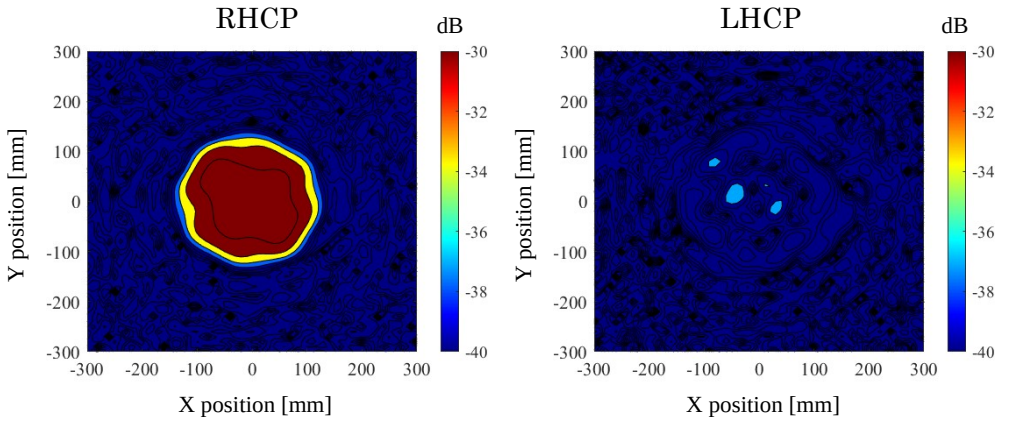

(a) Amplitude distribution

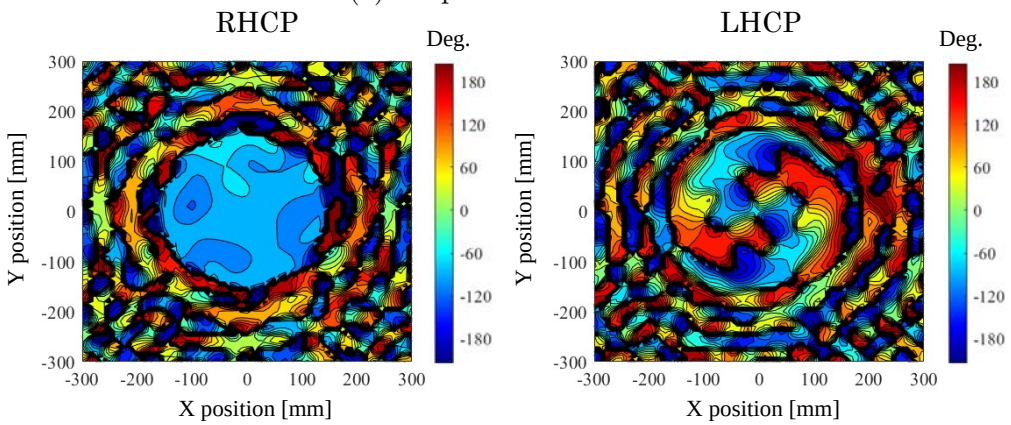

(b) Phase distribution

Figure 3.25: Measured aperture field distribution of the straight cross-slot feeding case at 5.8 GHz

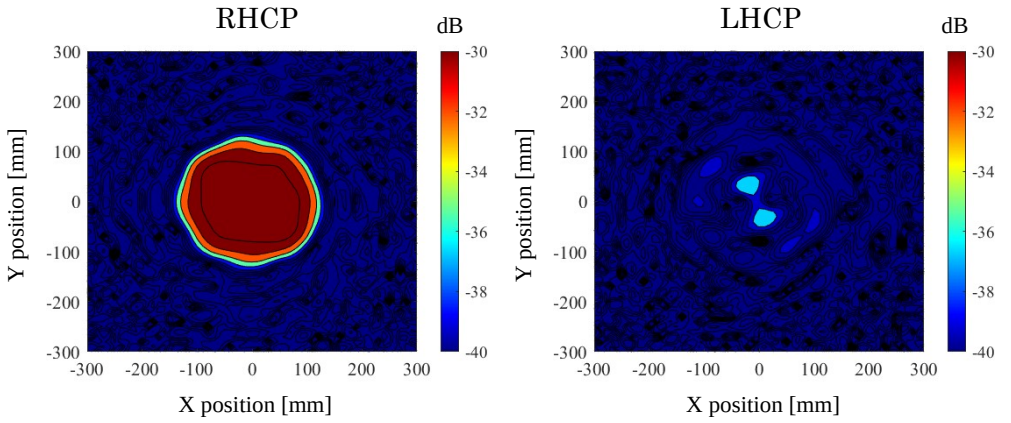

(a) Amplitude distribution

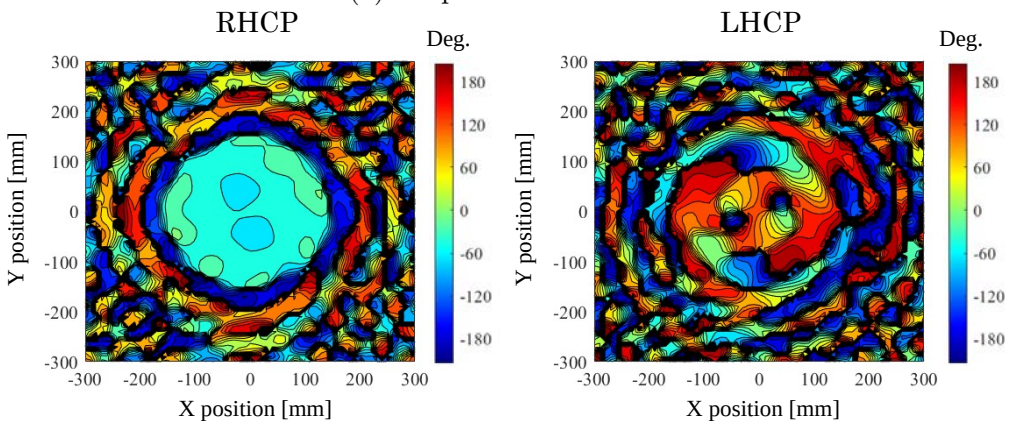

(b) Phase distribution

Figure 3.26: Measured aperture field distribution of the dog-bone cross-slot feeding case at 5.8 GHz

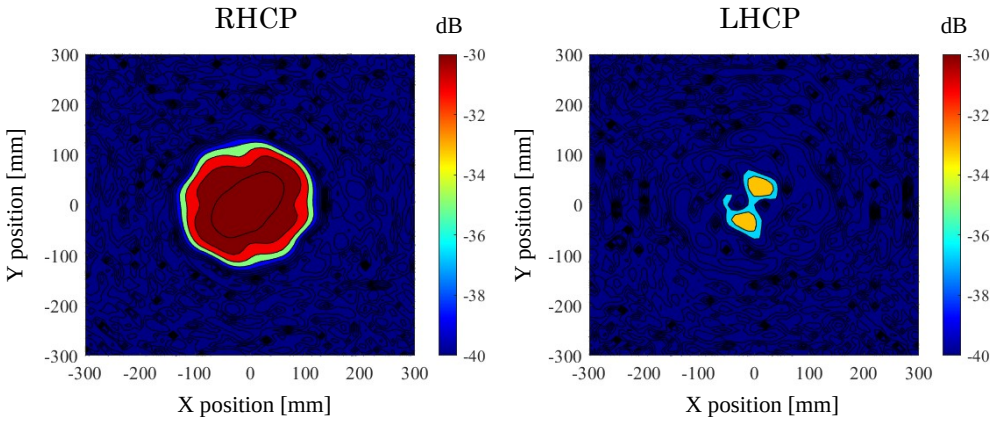

(a) Amplitude distribution

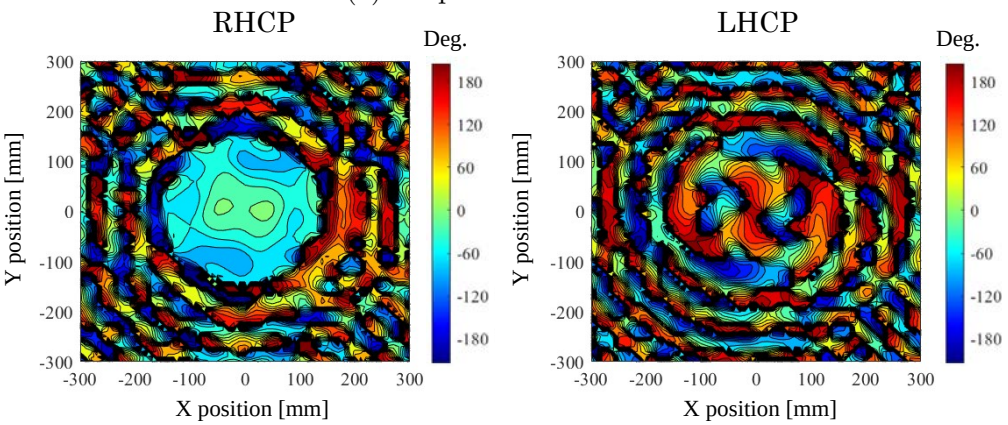

(b) Phase distribution

Figure 3.27: Measured aperture field distribution of the straight cross-slot feeding case at 5.9 GHz

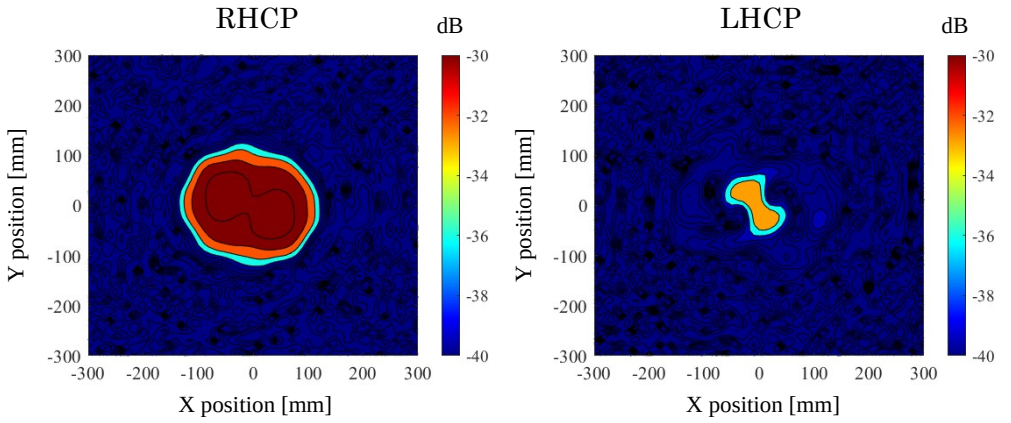

(a) Amplitude distribution

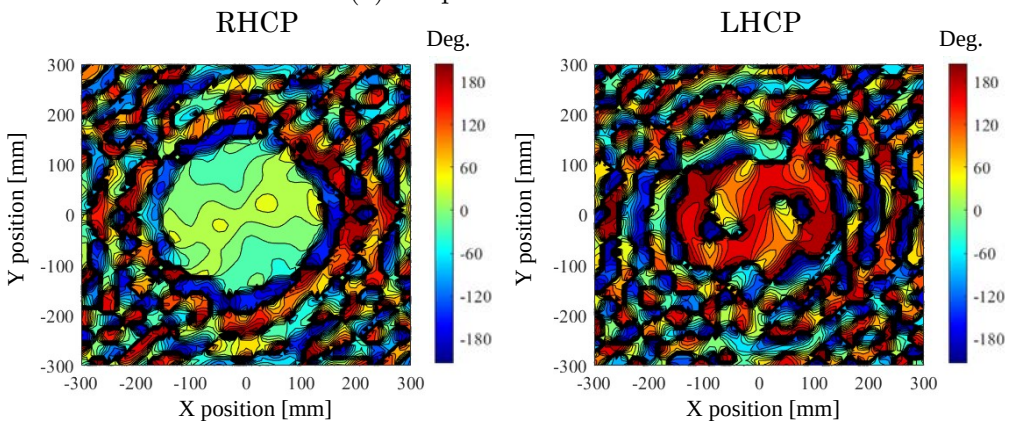

(b) Phase distribution

Figure 3.28: Measured aperture field distribution of the dog-bone cross-slot feeding case at 5.9 GHz

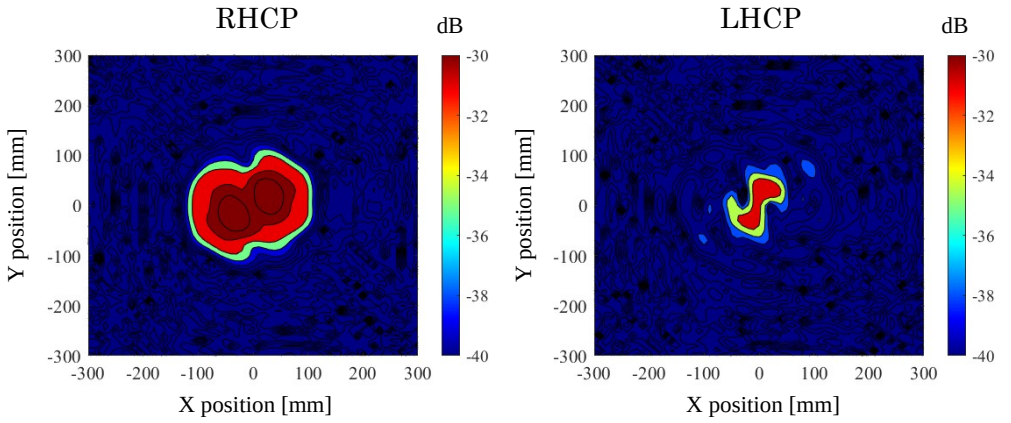

(a) Amplitude distribution

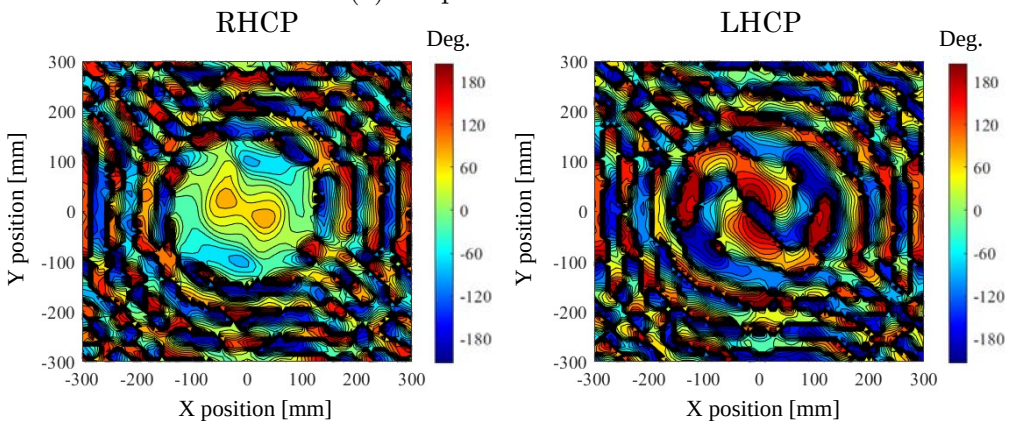

(b) Phase distribution

Figure 3.29: Measured aperture field distribution of the straight cross-slot feeding case at 6 GHz

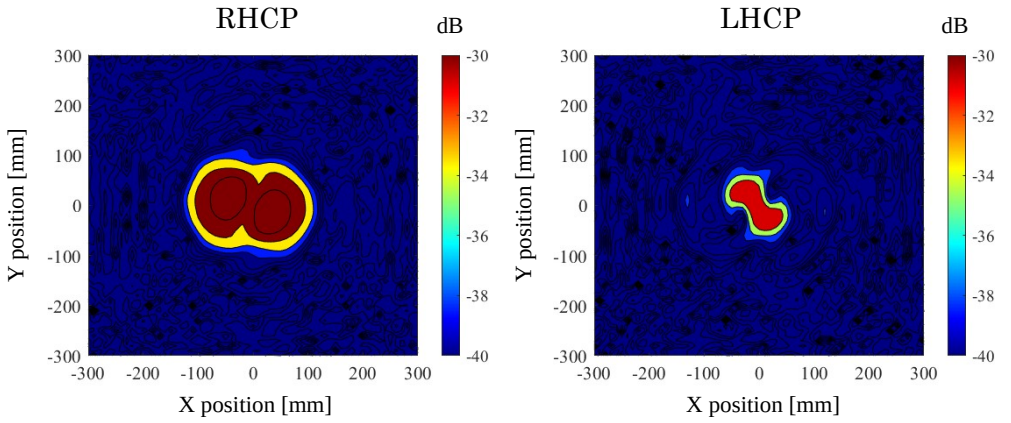

(a) Amplitude distribution

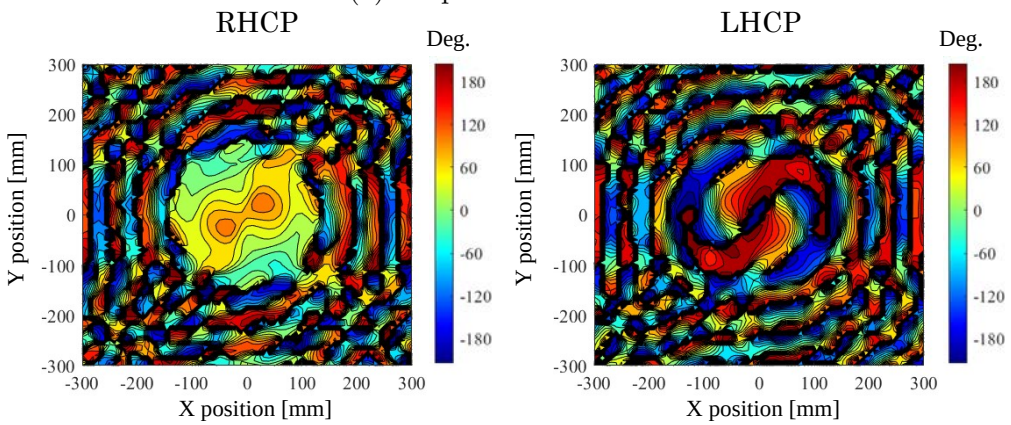

(b) Phase distribution

Figure 3.30: Measured aperture field distribution of the dog-bone cross-slot feeding case at 6 GHz

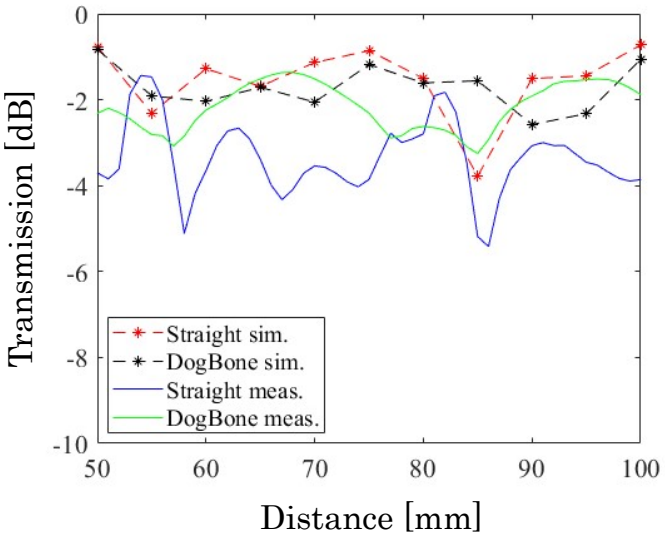

Figure 3.31: Plots of transmission over the distances from 50 mm to 100 mm

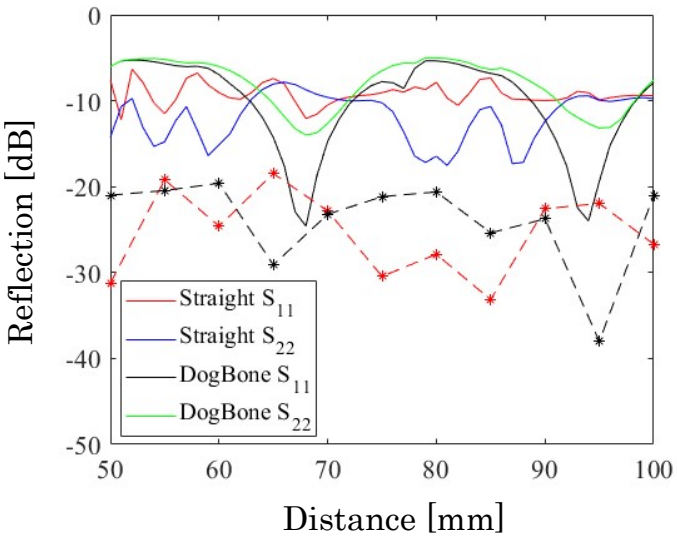

Figure 3.32: Plots of reflection over the distances from 50 mm to 100 mm

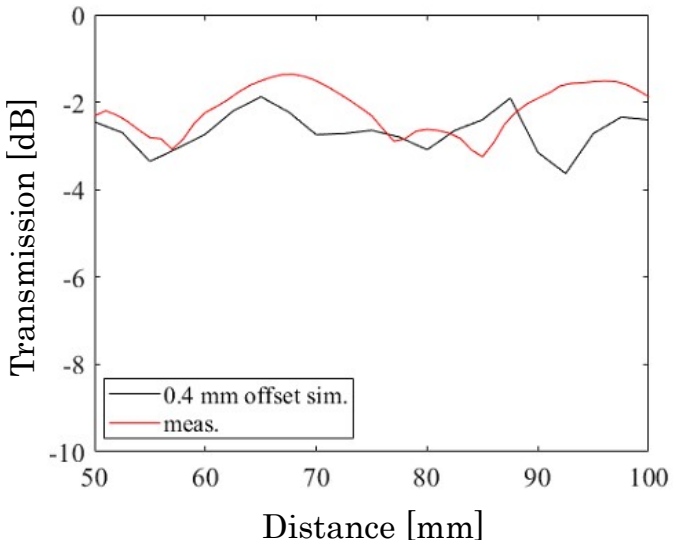

Figure 3.33: Plots of transmission of the dog-bone cross-slot fed RLSA over the distances from 50 mm to 100 mm assuming the fabrication error

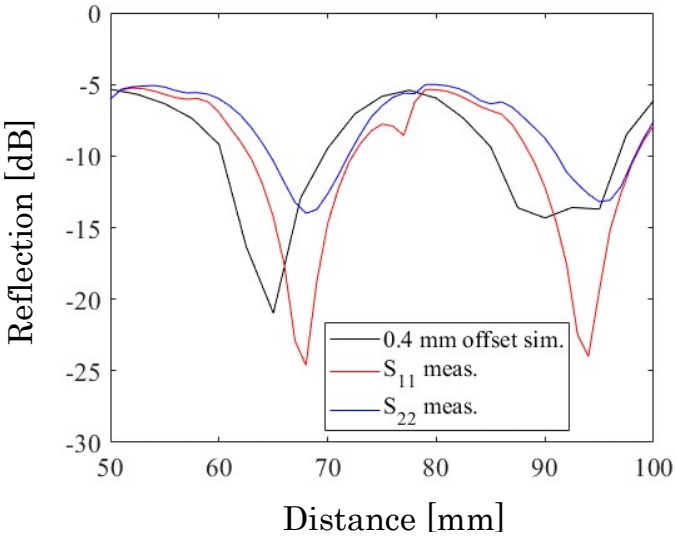

Figure 3.34: Plots of reflection of the dog-bone cross-slot fed RLSA over various distances from 50 mm to 100 mm assuming the fabrication error

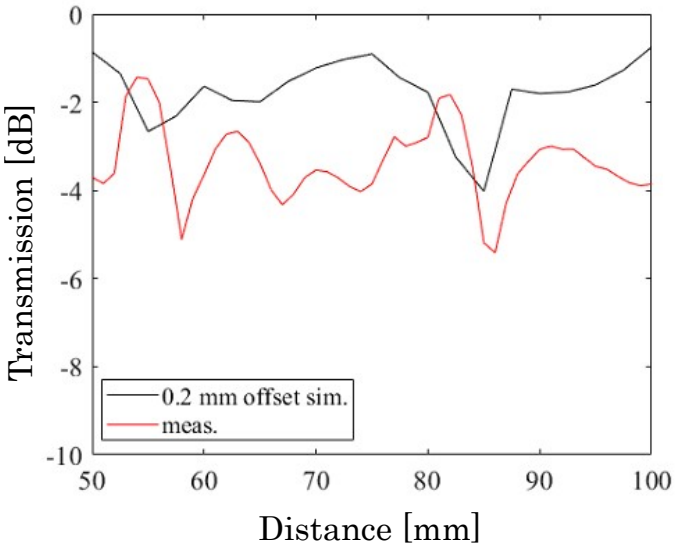

Figure 3.35: Plots of transmission of the straight cross-slot fed RLSA over the distances from 50 mm to 100 mm assuming the fabrication error

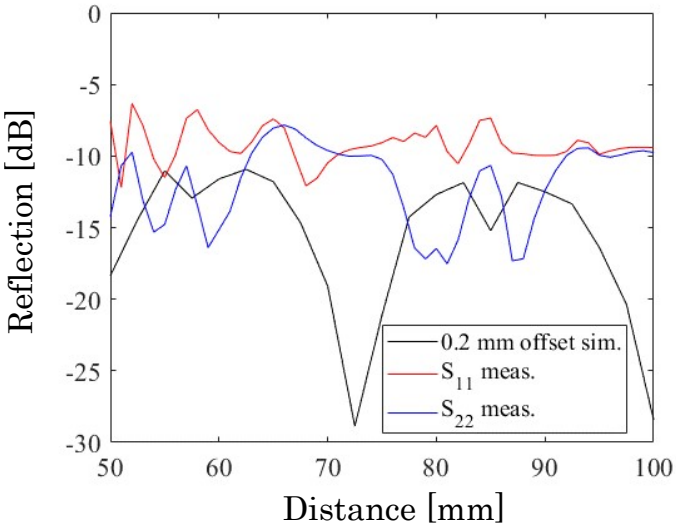

Figure 3.36: Plots of reflection of the straight cross-slot fed RLSA over various distances from 50 mm to 100 mm assuming the fabrication error

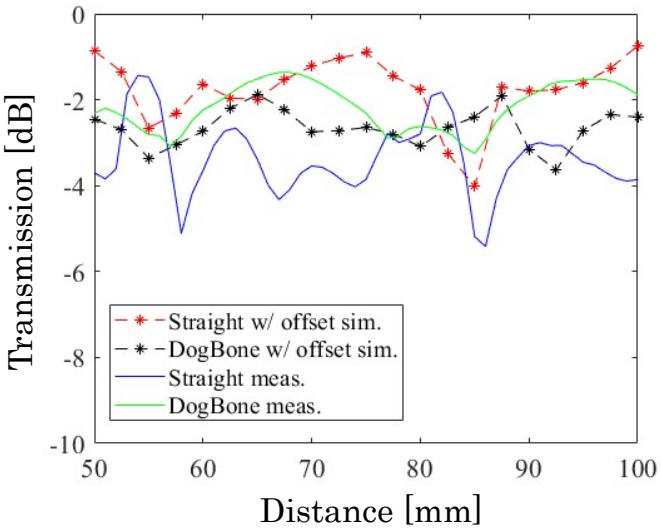

Figure 3.37: Plots of transmission for each feeding type

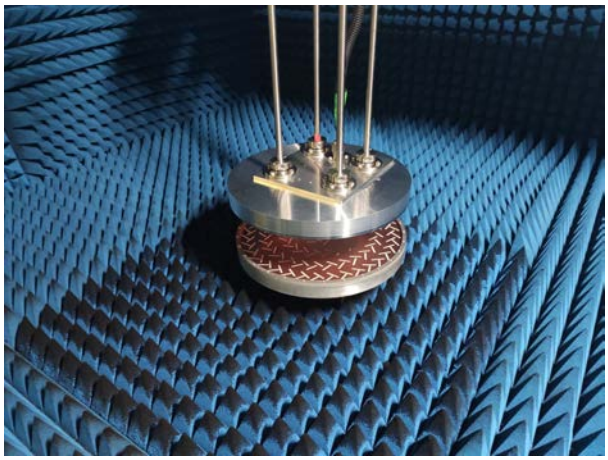

Figure 3.38: Transmission measurement between two identical RLSAs

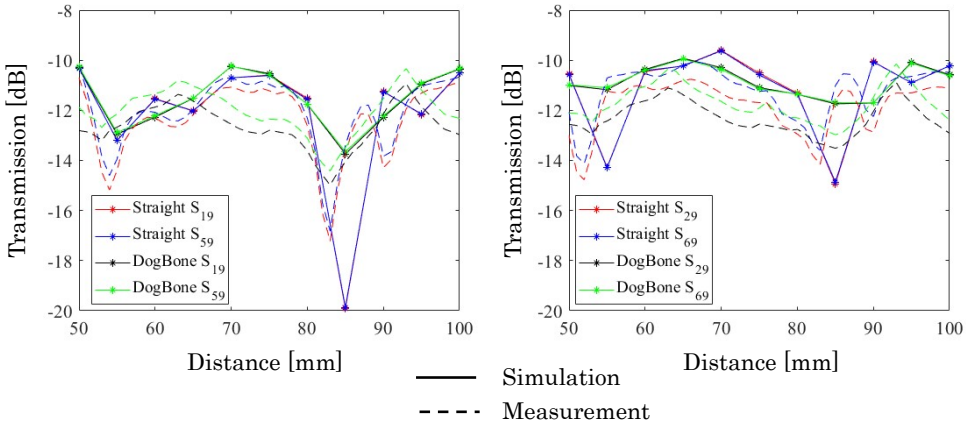

(a) Plots of $S_{19}, S_{29}, S_{49}, S_{59}$

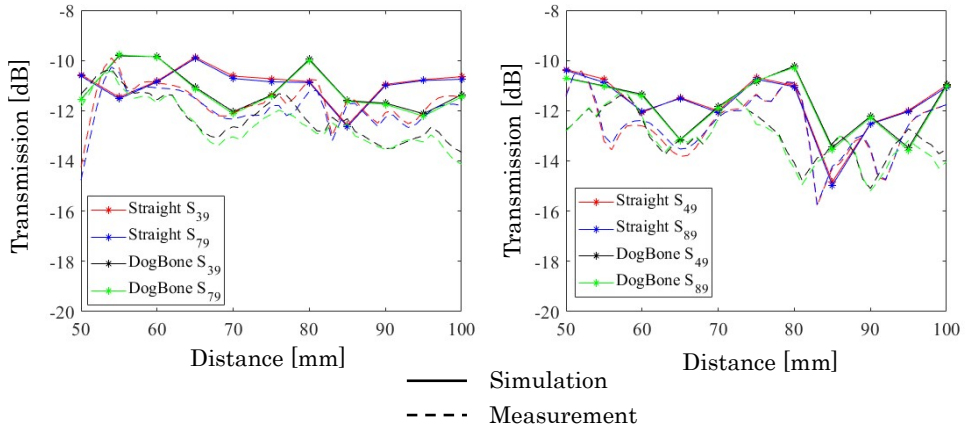

(b) Plots of $S_{39}, S_{49}, S_{79}, S_{89}$

Figure 3.39: Plots of transmission between the cross-slot fed RLSA and the 8-port microstrip fed RLSA over the distances from 50 mm to 100 mm

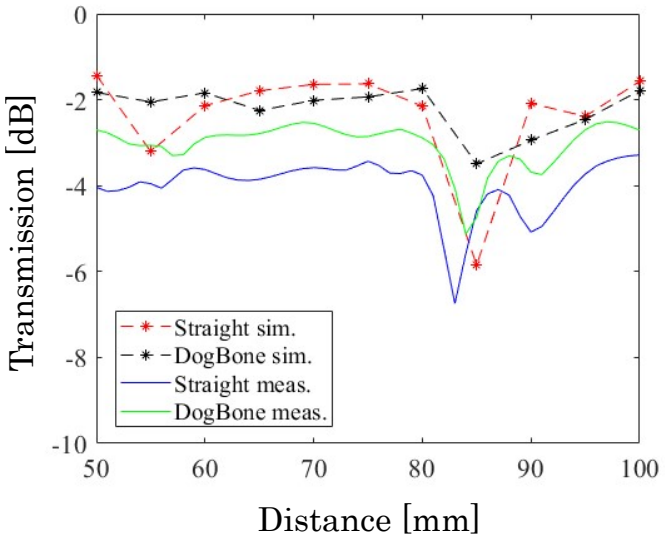

Figure 3.40: Plots of total transmission between the cross-slot fed RLSA and the 8-port microstrip fed RLSA over the distances from 50 mm to 100 mm

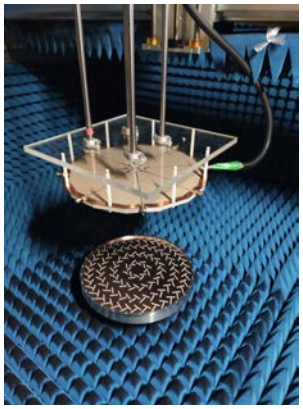

Figure 3.41: Transmission measurement between the cross-slot fed RLSA and the 8-port microstrip fed RLSA

References

[1] N. Shinohara, Y. Kubo, and H. Tonomura, "Mid-distance wireless power transmission for electric truck via microwaves," *Proceedings of URSI International Symposium on Electromagnetic Theory (EMTS)*, pp. 841–843, May 2013.

[2] S. Aldhaher, P. D. Mitcheson, J. M. Arteaga, G. Kkelis, and D. C. Yates, "Light-weight wireless power transfer for mid-air charging of drones," *Proceedings of European Conference on Antennas and Propagation (EUCAP)*, pp. 336–340, Mar. 2017.

[3] T. Ishikawa and N. Shinohara, "Flat-topped beam forming experiment for microwave power transfer system to a vehicle roof," *Wireless Power Transfer*, vol. 2, no. 1, pp. 15–21, Mar. 2015.

[4] A. P. Hu, C. Liu, and H. L. Li, "A novel contactless battery charging system for soccer playing robot," *Proceedings of International Conference on Mechatronics and Machine Vision in Practice (M2VIP)*, pp. 646–650, Dec. 2008.

[5] R. Erfani, F. Marefat, A. M. Sodagar, and P. Mohseni, "Transcutaneous capacitive wireless power transfer (c-wpt) for biomedical implants," *IEEE International Symposium on Circuits and Systems (ISCAS)*, May 2017.

[6] A. Kurs, A. Kalaris, R. Moffatt, J. Joannopoul0s, P. Fisher, and M. Soljacic, "Wireless power transfer via strongly coupled magnetic resonances," *Science Magazine*, no. 317, pp. 83–86, Jul. 2007.

[7] M. Rozman, M. Fernando, B. Adebisi, K. Rabie, R. Kharel, A. Ikpehai, and H. Gacanin, "Combined conformal strongly-coupled magnetic resonance for efficient wireless power transfer," *Energies*, vol. 10, no. 4, Apr. 2017.

[8] K. Tsujimoto, H. Yashiro, E. Fujiwara, N. Tanaka, T. Fujiwara, Y. Takahashi, K. Sudo, M. Ando, H. Matsumoto, K. Hashimoto, and N. Shinohara, "Study of microwave power transmitting antenna for solar power station/satellite," *Asia-Pacific Microwave Conference (APMC)*, TH2C-03, Nov. 2002.

[9] T. Tomura, J. Hirokawa, M. Furukawa, and T. Fujiwara, "Radial line slot array antenna for 5.8-ghz-band beam-type wireless power transmission," *Proceedings of European Conference on Antennas and Propagation (EuCAP)*, T02-A10.2, Mar. 2020.

[10] M. Ando, K. Sakurai, N. Goto, K. Arimura, and Y. Ito, "A radial line slot antenna for 12 ghz satellite tv reception," *IEEE Transactions on Antennas and Propagation*, vol. 13, no. 12, pp. 1347–1353, Dec. 1985.

[11] M. Zhang, K. Toyosaki, J. Hirokawa, M. Ando, T. Taniguchi, and M. Noda, "A 60 ghz-band compact-range gigabit wireless access system using large array antennas," *IEEE Transactions on Antennas and Propagation*, vol. 63, no. 8, pp. 3423–3440, Aug. 2015.

[12] T. Tomura, J. Hirokawa, M. Furukawa, T. Fujiwara, and N. Shinohara, "Eight-port feed radial line slot antenna for wireless power transmission," *IEEE Open Journal of Antennas and Propagation*, vol. 2, pp. 170–180, Jan. 2021.

[13] T. Tomura, J. Hirokawa, M. Furukawa, and T. Fujiwara, "Radial line slot array antenna for 5.8-ghz band beam-type wireless power transmission," *IEICE Technical Report*, vol. 119, no. 295, pp. 87–90, Nov. 2019.

[14] K. Sudo, T. Oizumi, J. Hirokawa, and M. Ando, "Reduction of azimuthal amplitude ripple in the rotating-mode feed to a radial waveguide by using a crossed dog-bone slot," *IEEE Transactions on Antennas and Propagation*, vol. 55, no. 9, pp. 2618–2622, Sep. 2007.

[15] W. C. Brown, "The history of wireless power transmission," *Solar Energy*, vol. 56, no. 1, pp. 3–21, Jan. 1996.

[16] G. Goubau and F. Schwering, "On the guided propagation of electromagnetic wave beams," *IRE Transactions Antennas and Propagation*, vol. 9, no. 3, pp. 248–256, May 1961.

[17] V. H. Rumsey, "On the design and performance of feeds for correcting spherical aberration," *IEEE Transactions on Antennas and Propagation*, vol. 18, no. 3, pp. 343–251, May 1970.

[18] K. Sudo, "Electromagnetic Design of Slots for Rotational Symmetric Operation in Radial Line Slot Antennas," Ph.D. dissertation, Department of Electrical and Electronic Engineering, Tokyo Institute of Technology, 2005.

[19] A. Akiyama, J. Hirokawa, M. Ando, E. Takeda, and Y. Arai, "60ghz band small aperture conical beam radial line slot antennas," *IEICE Transactions on Electronics*, vol. E82-C, no. 7, pp. 1229–1235, Jul. 1999.

[20] C. T. R. et al., "Microwave and millimeter wave power beaming," *IEEE Journal of Microwaves*, vol. 1, no. 1, pp. 229–259, Jan. 2021.

[21] W. C. Brown, "Experiments involving a microwave beam to power and position a helicopter," *IEEE Transactions on Aerospace Electronic Systems*, vol. AES-5, no. 5, pp. 692–702, Sep. 1969.

[22] J. J. Schlesak, A. Alden, and T. Ohno, "A microwave powered high altitude platform," *IEEE MTT-S International Microwave Symposium*, May 1988.

[23] N. Shinohara and H. Matsumoto, "Dependence of dc output of a rectenna array on the method of interconnection of its array elements," *IEEJ Transactions on Electrical and Electronic Engineering*, vol. 125, no. 1, pp. 9–17, Oct. 1998.

[24] X. Yang, W. Geyi, and H. Sun, "Optimum design of wireless power transmission system using microstrip patch antenna arrays," *IEEE Antennas and Wireless Propagation Letters*, vol. 16, pp. 1824–1827, Mar. 2017.

[25] N. Shinohara, Y. Kubo, and H. Tonomura, "Wireless charging for electric vehicle with microwaves," *International Electric Drives Production Conference (EDPC)*, Oct. 2013.

[26] N. Takabayashi, N. Shinohara, and T. Fujiwara, "Array pattern synthesis of flat-topped beam for microwave power transfer system at volcanoes," *IEEE Wireless Power Transfer Conference (WPTC)*, Jun. 2018.

[27] N. Shinohara, "Beam control technologies with a high-efficiency phased array for microwave power transmission in japan," *Proceedings of IEEE*, vol. 101, no. 6, pp. 1448–1463, Jun. 2013.

[28] H. Matsumoto, K. Hashimoto, N. Shinohara, and T. Mitani, "Experimental equipments for microwave power transmission in kyoto university," *Proceedings of International Conference on Solar Power from Space*, Jun. 2004.

Chapter 4

A Parallel Plate Slot Array Antenna for Short-Range Transmission

4.1 Introductory Remarks

A waveguide slot antenna constructed with parallel plate waveguide has a simple structure and small feeding losses. In addition, the parallel plate waveguide antenna structure has the potential for high efficiency and mass produceability. The RLSA, a parallel plate structure antenna, which was discussed in the previous chapter for the potential for wireless power transfer (WPT) was originally utilized in satellite communication [1]. For these reasons, a waveguide slot antenna designed based on parallel plate waveguide structure is expected to be a possible candidate for both wireless communication and WPT applications. The objectives of this study is to investigate a parallel plate waveguide antenna with a series feeding which would be a candidate for short-range transmission and has better performances than those of the previously proposed RLSAs. One issue of a cross-slot fed RLSA is that the aperture field distribution is significantly strong near the region between the innermost slot pairs and the coupling slot while this is not an issue in the parallel plate waveguide antenna with a series feeding. Therefore, it is expected that the proposed antenna have better antenna performance.

We proposed a parallel plate waveguide slot antenna with a dipole layer for linear-to-circular polarization conversion. The basic structure of this an-

tenna which supports linear polarization was proposed in [2]. A dipole layer ,[3], [4] was adopted to realize circular polarization. We originally intended to design this antenna at 5.8 GHz, but due to the fabrication limitations the antenna will be designed and fabricated at 26 GHz. However in recent years the demand of internet usage has been increasing drastically. Together with the idea of internet of things (IoT), the telecommunication tendency is aiming for the usage of high frequency band; one example is the exploration of millimeter-wave bands for 5G applications. Millimeter-wave band attracts significant interests for IoT [5]. This has motivated investigations in millimeter-wave wireless power transmission (WPT) for for future IoT applications [6], [7], [8]. Examples of IoT applications include IoT body area network (BAN) and sensing. IoT BANs have various applications in healthcare monitoring, fitness tracking, defense and wearable sensing [5]. The concepts of millimeter-wave identification (MMID) in sensing applications was investigated in [9].

4.2 Antenna Configuration

The structural detail of the antenna is shown in Fig. 4.2. The feeding part is composed of one substrate layer on a copper plate. coupling slots were etched into the copper layer on the top of the substrate. The post wall structure was employed to form the side walls of the feeding waveguide. This allows the fabrication by printed circuit board (PCB). The radiating part consists of two substrate layers;one is for the parallel plate (radiating) waveguide and the other is to support the dipole layer. In similar to the coupling slots, the radiating slot pairs are on the copper layer over the substrate and dipoles on the top layer are also of copper. All substrates layers were made from poly tetra fluoro ethylene (PTFE), which has a dielectric constant of 2.16 and a loss tangent of 0.001. Copper has a bulk conductivity of 5.8×10^7 S/m. For the sake of assembly, the peripheries of every layers will be covered by aluminium, which has a bulk conductivity of 3.8×10^7 S/m. these values will be used in the design in the following section.

Before moving on to the design methods, we discuss briefly the antenna operation. TE_{10} is excited at the center of the feeding waveguide through WR-420. the traveling mode TE_{10} is then coupled with the coupling slots arranged at the center of the feeding waveguide and the slot spacing is approximately a guided wavelength to excite the magnetic field in phase. The

coupling amount and reflection of the coupling slots are controlled by the capacitive post and inductive post respectively, [10], [11], [12]. a quasi-TEM is excited by these coupling slots and propagates in the parallel plate waveguide. The radiating slots are arranged in pair and each pair is spaced by a quarter of a guided wavelength. The reflection from the two slots in a pair nearly cancel since the round-trip phase different is approximately 180°, [2]. each slot pair is spaced by a guided wavelength to realize in-phase excitation. coupled with the propagating TEM, slot pairs radiate linear polarized fields. An interaction between slot pairs and dipoles converts the polarization into a circular polarization, [3], [4].

The antenna has the feeding circuit at the center and 14×6 radiating elements are positioned on each side, 14×12 elements in total. The design frequency of this antenna is 26 GHz.

4.3 Antenna Design

In this section, we address the design procedure of this antenna in detail. Similar to the previous chapter, the feeding part and the radiating part will be designed separately and the complete antenna structure is the result from combining these two parts. We use electromagnetic simulator software HFSS for the entire design procedure.

4.3.1 Feeding Part

As previously mentioned, TE_{10} is to be excited at the center of the feeding waveguide and coupled with the coupling slots along the feeding waveguide to excite TEM in the radiating waveguide. For this, a coupling slot has to be excited uniformly. Fig. 4.1 show an amount of coupling power required for each coupling slot to realize the uniform amplitude excitation. In this design, we used 6 coupling slot on each side (12 slots in total). Therefore, we have to design the coupling slots with the following specification: slot#6→17%, slot#5→20%, slot#4→25%, slot#3→33%, and slot#2→50% where slot#6 is the closest to the excitation slot. Slot#1 or a matching slot which is a special case is required to couple 100% of power. Fig. 4.5 show an analysis model for a coupling slot and key parameters are indicated in Fig. 4.6. Here, the board wall size of the feeding waveguide is 5.78 mm and the narrow wall size is 1.60 mm. The waveguide is filled with PTFE. Periodic boundary condition (PBC)

is imposed on the size walls of port 3 and 4 to include the mutual coupling effect from adjacent slots. The slot thickness and width are fixed at 18.0 μm and 0.50 mm respectively. The coupling slot is positioned at the center of the feeding waveguide where magnetic field is zero. To allow the coupling to occur, a capacitive wall is utilized. At the same time, an inductive wall is used to suppress the reflection, see [10], [11], [12]. Generally, the width of the capacitive wall and inductive wall is fixed for a design frequency. Also, the slot length SLLM is approximately the same for all coupling slots. Therefore, IWPX, IWPY, CWPX, and CWPY are to be adjusted to realize a desired coupling amount and acceptable reflection. For the fabrication purpose, we use a capacitive post and an inductive post instead of the capacitive and inductive walls as shown in Fig. 4.7-4.8. Note that the model in Fig. 4.7 is for normal elements indicated in Fig. 4.3. The diameters of the capacitive and inductive post are 0.80 mm and 0.40 mm respectively. The model in Fig. 4.7 is applied for slot#6-slot#2. For slot#1 (matching slot) in Fig. 4.3, port 2 in Fig. 4.7 is to be terminated by short circuit and the condition on the side walls of port 3 and 4 is changed to perfect magnetic condition (PMC) as shown in Fig. 4.9. In this case the distance from the matching slot to the short end also needs to be controlled. Fig. 4.10 shows plots of S_{21} which represents the amount of coupling power and Fig. 4.11 shows plots of reflection for various slots. Table 4.1 shows the design parameters of each coupling slot.

Slot#	SLLM	IWPX	IWPY	CWPX	CWPY
6	3.89	1.50	0.67	1.40	1.08
5	3.89	1.50	0.98	1.40	1.10
4	3.89	1.51	1.07	1.41	1.27
3	3.90	1.54	1.14	1.44	1.46
2	3.91	1.60	1.27	1.50	1.81
1	3.91	0.80	2.1	1.26	2.10
Length unit is in [mm]					

Table 4.1: Design parameters of the coupling slot

Each coupling slot is spaced by approximately a guided wavelength to realize the in-phase excitation. Please refer to equation 1 in [11] for the specific slot spacing. Combining all the design slot, we arrive at the model shown in Fig. 4.12. Here, the solid wall is replaced by post wall, [13]. This

structure can be fabricated by PCB. Fig. 4.13 provides plots of the amplitude and phase distribution of the field at a quarter of a guided wavelength over the center of the feeding waveguide and inside the parallel plate waveguide. Furthermore, Fig. 4.14 gives plots of reflection. The results in Fig. 4.13-4.14 confirm the acceptable performance for our design parameters and that the replacement of the solid wall by the post wall maintains the same performance.

4.3.2 Radiating Part

The same approach as the design of the feeding part is used here. In order to excite the radiating element (parallel slot pair) uniformly, we need to design the coupling amount of each slot pair as indicated in Fig. 4.1. Since 6 slot pairs are used, the specification for the amount of coupling power is the same as those mentioned in subsection 4.3.1. Fig. 4.15-4.16 show the analysis model for a radiating slot pair with a dipole. The model in Fig. 4.15 is for normal elements as shown in Fig. 4.4. The height of the parallel plate as well as the substrate for the dipoles is 1.60 mm. They are of PTFE. The thickness and width of each radiating slot and dipole are 18 μm and 0.50 mm respectively. PBC is applied to the side walls of the parallel plate to account for the mutual coupling from adjacent slot pairs. In the same manner, The boundary conditions for the side walls of the dipole layer and external region (vacuum box) are PBC. From the design point of view, the optimum parameters for a dipole indicated in Fig. 4.16 are independent of the parameters of a radiating slot, [3]. These parameters s, θ, and ds mainly control the axial ratio while the length of a radiating slot pair l_1 and l_2), and slot spacing dl effect radiating power and reflection, [2]. As for the matching slot design in Fig. 4.4, the analysis model is slightly modified, see Fig. 4.17. Port 2 is terminated by the short circuit condition and the external region must cover the short end to include the radiation effect from the antenna periphery. PBC on the side wall of the dipole layer and the eternal region is removed. Either perfect matched layer (PML) or impedance boundary (IB) should be applied to the side wall on the left side of the dipole layer. Similar to the matching slot design in the feeding part, the distance between the matching slot and the short end needs to be adjusted so that an acceptable reflection level can be achieved. Fig. 4.18-4.20 show the design results of each radiating element. It is evident that the radiating element each has acceptable reflection (below -20 dB) and axial ratio (below 1 dB). Table 4.2

gives the design parameters of each radiating element.

Slot#	l_1	l_2	dl	s	ds
6	3.27	3.44	1.54	4.05	0.10
5	3.32	3.50	1.51	4.05	0.10
4	3.40	3.58	1.46	4.05	0.10
3	3.50	3.70	1.40	4.05	0.10
2	3.63	3.88	1.30	4.05	0.10
1	3.60	4.30	1.40	3.70	0
Length unit is in [mm]					

Table 4.2: Design parameters of the radiating slot pair

The inclination angle of each dipole θ is equal to 44°. To excite radiating elements in the same phase, each slot pair is spaced by approximately a guided wavelength, a more accurate value can be estimated by including the radiation phase of the slot pair in consideration, please see equation 1 in [11]. Fig. 4.21-4.22 show an analysis model of a one-dimensional array model and its electric field distribution at a quarter of a free-space wavelength over the dipole layer respectively. Plots of the amplitude and phase distribution of electric field components along the center of the array are given in Fig. 4.25a-4.25b in which the black-dashed lines indicate the position of each radiating element. In addition, Fig. 4.23-4.24 show the simulated reflection and axial ratio of the model in Fig. 4.21. The reflection and axial ratio values are within an acceptable range. The full radiating part is the concatenation of the one-dimensional array in Fig. 4.21.

4.3.3 Complete Antenna Structure

The complete antenna is the result of combining the feeding part in subsection 4.3.1 and the radiating part in subsection 4.3.3. To physically hold the feeding and radiating parts together, they will be put in the metal case. The pre-fabrication model is illustrated in Fig. 4.26. The metal case is made from aluminium by milling. The feeding waveguide and the radiating parallel slot pair layer will be attached using laminating techniques. More precisely, The coupling slot layer and the substrate of the radiating slot layer will be bonded together by the roger 3001 bonding film (thermoplastic chlorofluorocopolymer). Roger 3001 has a dielectric constant of 2.28 and dielectric

tangent loss of 0.003. The minimal thickness of the bonding film is 38.1 μm. Considering the dielectric constants of the bonding film and the substrate (PTFE), the equivalent dielectric constant would not differ from that of PTFE. Therefore, it is expected that the bonding film will not significantly effect the antenna performances. Though the dipole layer is not chemically bonded to the radiating slot pair layer, it will be stacked on the top of the radiating slot pair layer and mechanically attached using the aluminium lid shown in Fig. 4.27. To this end, the array size is 78.5×90 mm^2. The antenna dimension including its metal case is $98.5 \times 110 \times 20$ mm^3.

4.4 Results

The full structure of the antenna in Fig. 4.26 was analyzed. Fig. 4.28-4.29 show plots of the reflection, axial ratio, and directivity respectively. The reflection is below -10 dB from 25.5 GHz to 26.5 GHz, which gives about 1 GHz bandwidth, i.e., 3.85% of the center frequency. This value is rather small for a data communication application; however it is more sufficient for a power transmission application. The axial ratio is also within an acceptable range (below 3 dB). Fig. 4.32 provide a plot of the simulated realized gain, which indicates approximately 70% antenna efficiency at the operating frequency. The simulated aperture field distribution is given in Fig. 4.31a-4.31b. Transmission characteristics over distances from 20 mm to 40 mm was simulated. Fig. 4.33 and 4.34 show the transmission and reflection between two designed parallel plate slot antennas. The simulated distance range is chosen to conform with that of RLSAs in the previous chapter. large degradation in the transmission is observed especially at 33 mm. The reason for small transmission at 33 mm might come from the accuracy of the simulation since the simulation model is quite large and the adaptive passes could not meet high accuracy requirement. Though our target is performance improvement especially in terms of transmission. The comparison with the RLSA designed in chapter 3 is difficult because of their operating frequencies.

4.5 Concluding Remarks

A parallel-plate slot array antenna with circular polarization was designed for applications in short-range transmission. Unfortunately, the antenna was

designed at 26 GHz due to the fabrication limitation. The simulation results suggest below -30 dB of return loss and approximately 3.85% bandwidth of the design frequency. Right-handed circular polarization was confirmed by simulation with axial the ratio below 1 dB. The antenna gain is 26.50 dBi and its aperture efficiency is approximately 70%. The single antenna performance suggests the potential for applications in both short-range communication and WPT. However, the simulated transmission is especially small at 33 mm. One of the reasons might come from the accuracy of the simulation. In order to improve the accuracy, meshing techniques will be applied. Furthermore, we will fabricate a prototype and conduct an experiment to verify its performance.

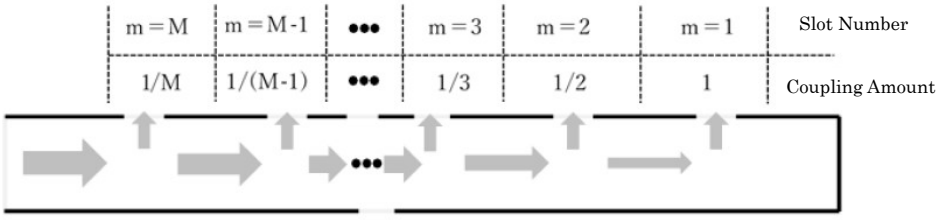

Figure 4.1: Antenna Structure

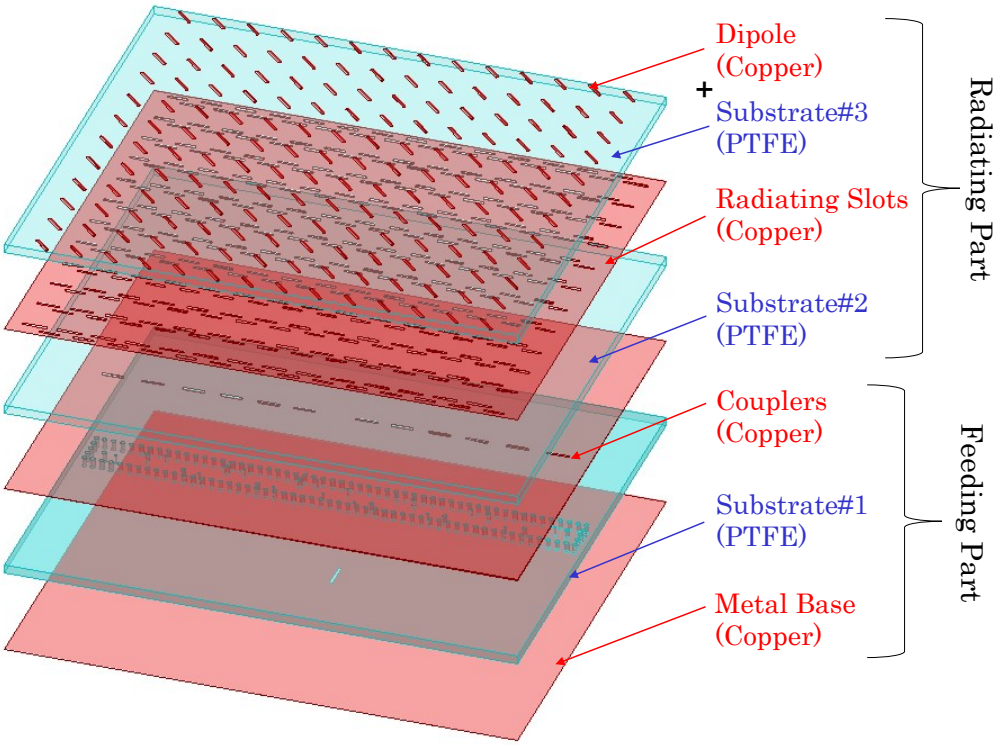

Figure 4.2: Antenna Structure

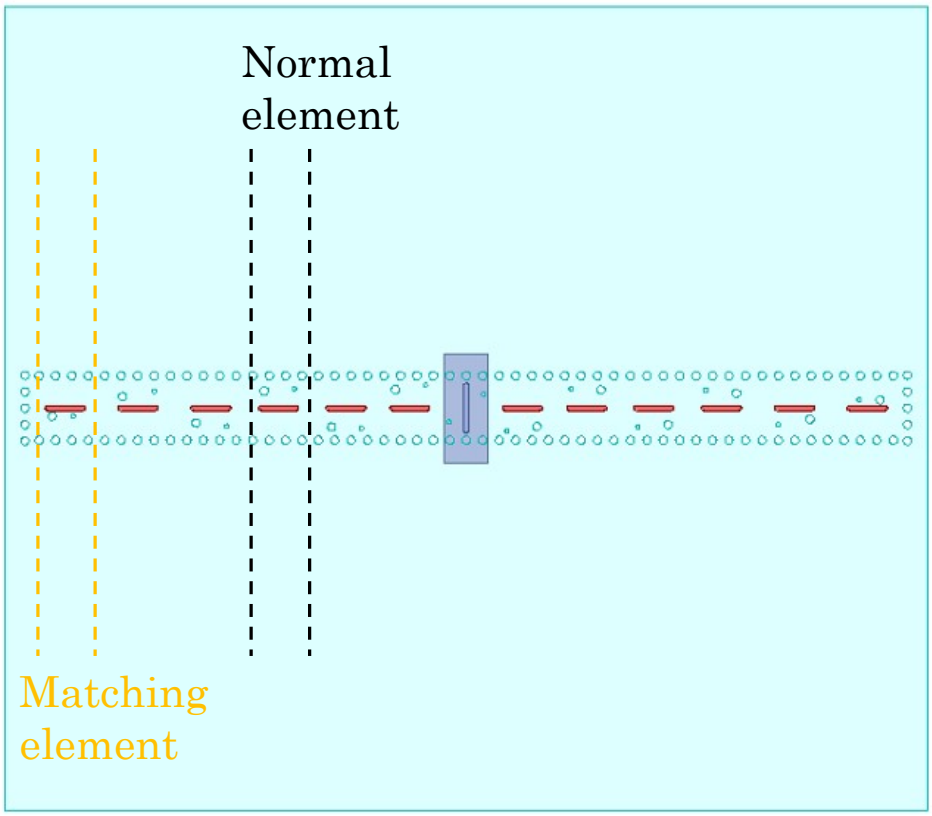

Figure 4.3: Coupling elements

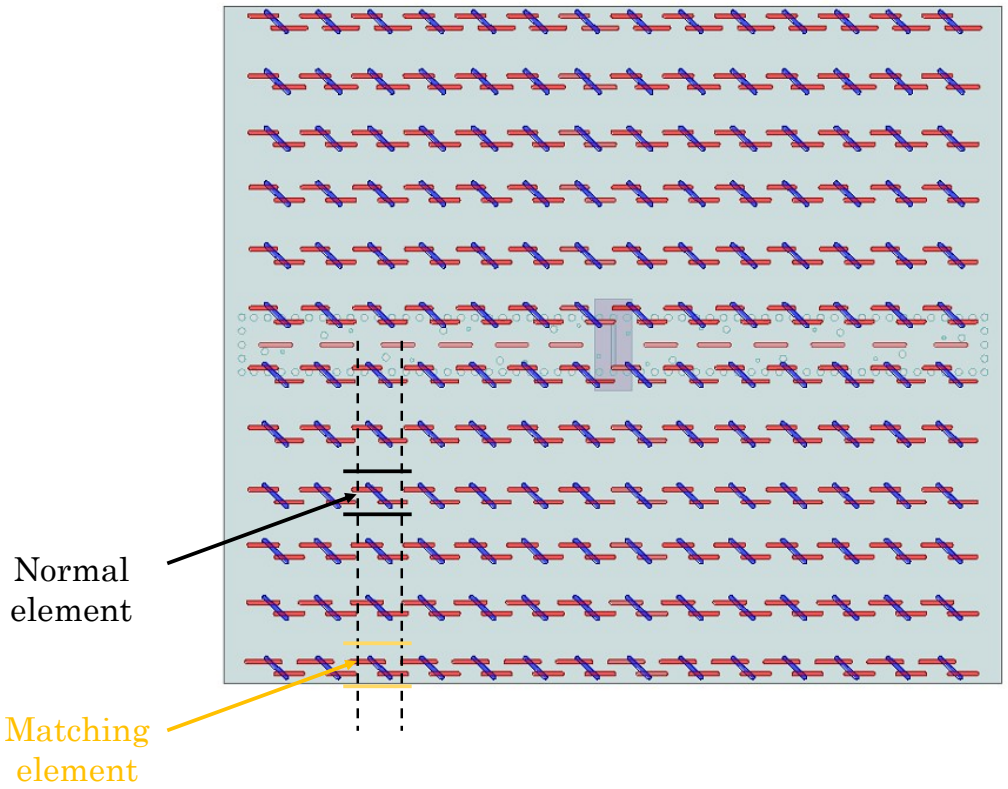

Figure 4.4: Radiating elements

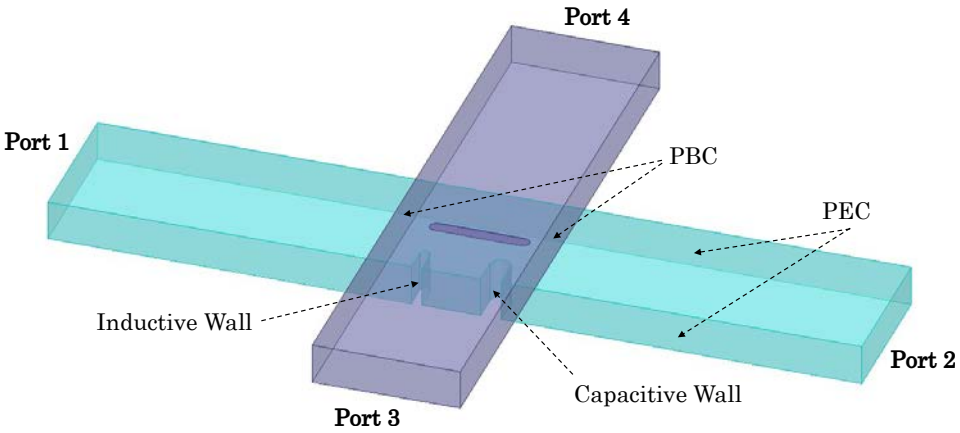

Figure 4.5: Analysis model for a coupling slot with an inductive wall and a capacitive wall

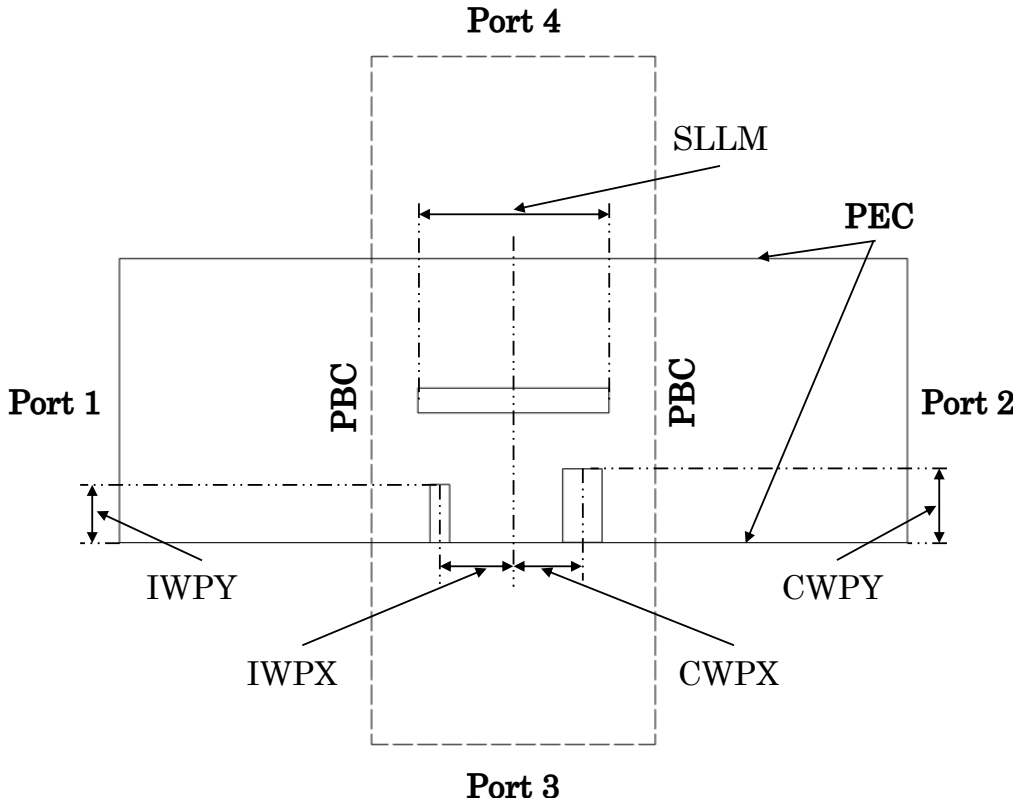

Figure 4.6: Design parameters of a coupling slot with an inductive wall and a capacitive wall

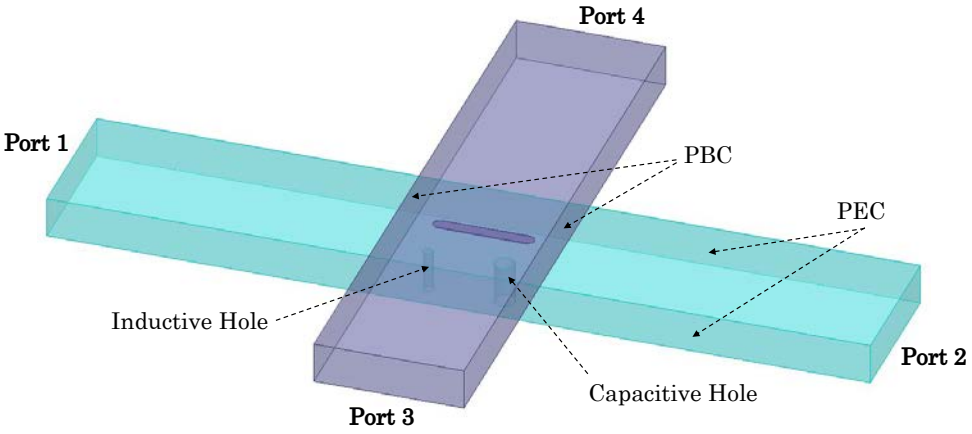

Figure 4.7: Design parameters of a coupling slot with an inductive post and a capacitive post

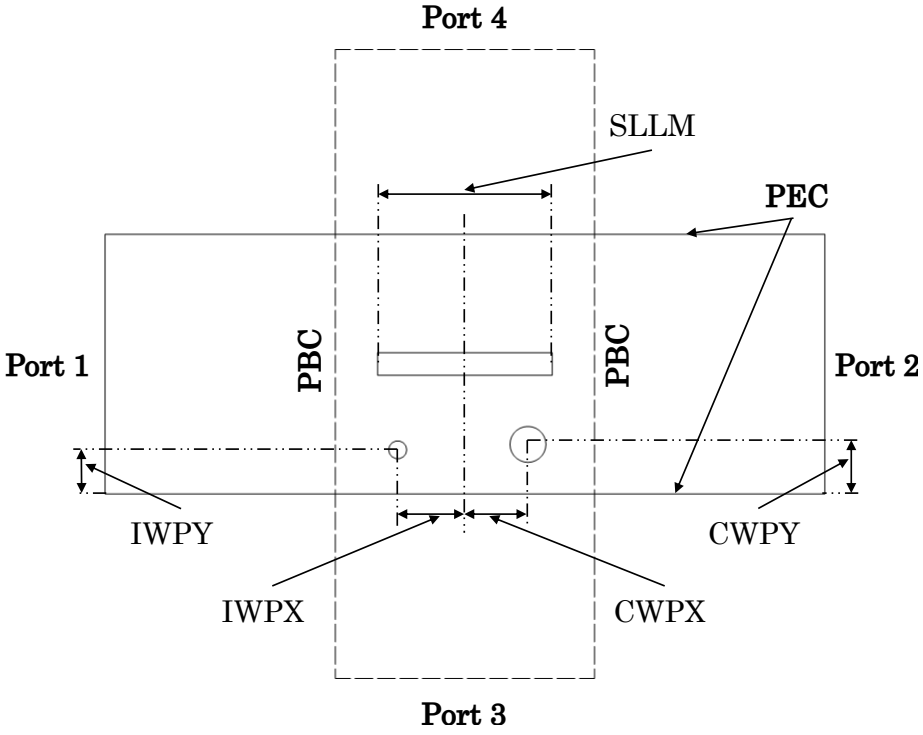

Figure 4.8: Design parameters of a coupling slot with an inductive post and a capacitive post

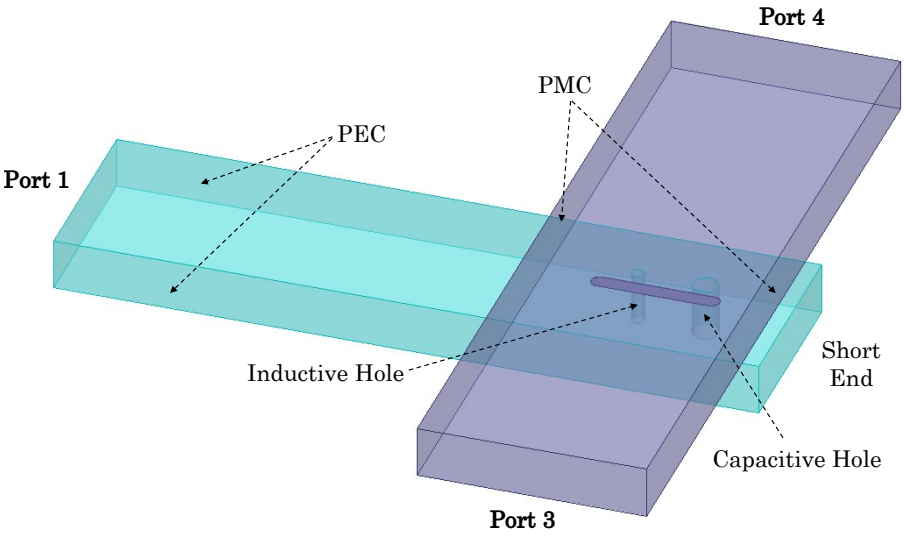

Figure 4.9: Analysis model for the matching slot

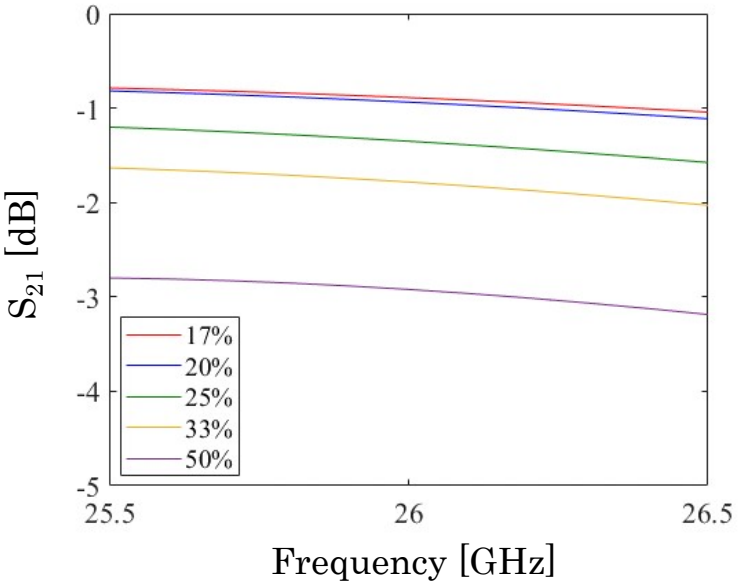

Figure 4.10: Plots of S_{21} showing the amount of coupling power of each coupling slot

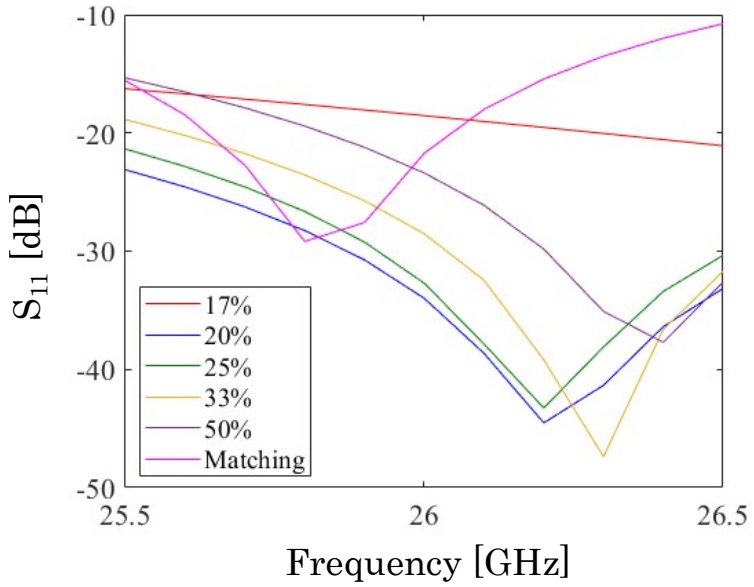

Figure 4.11: Plots of reflection for each coupling slot

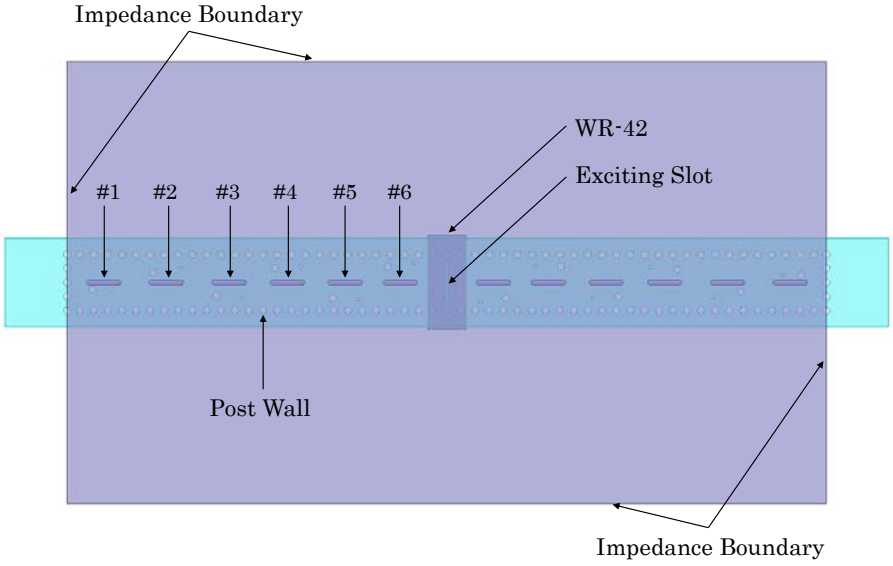

Figure 4.12: Full feeding part

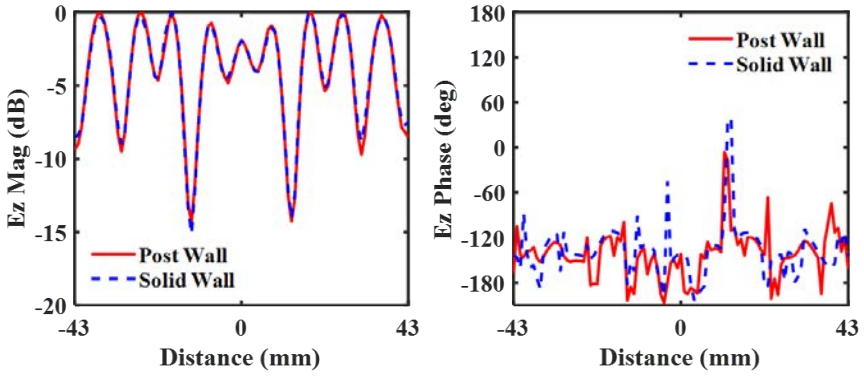

Figure 4.13: Field distribution along the center of the feeding waveguide

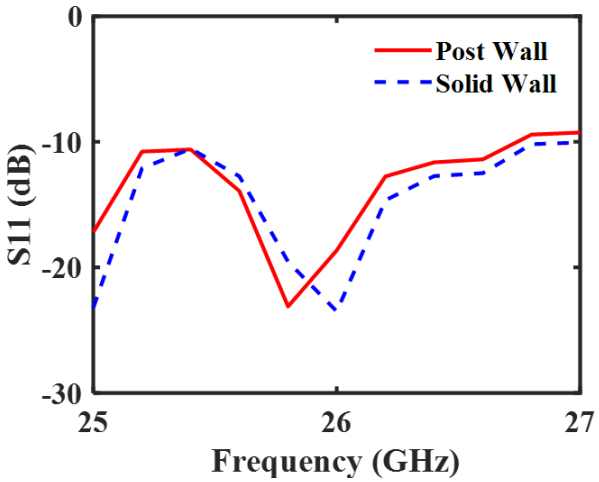

Figure 4.14: Plot of reflection of the feeding part

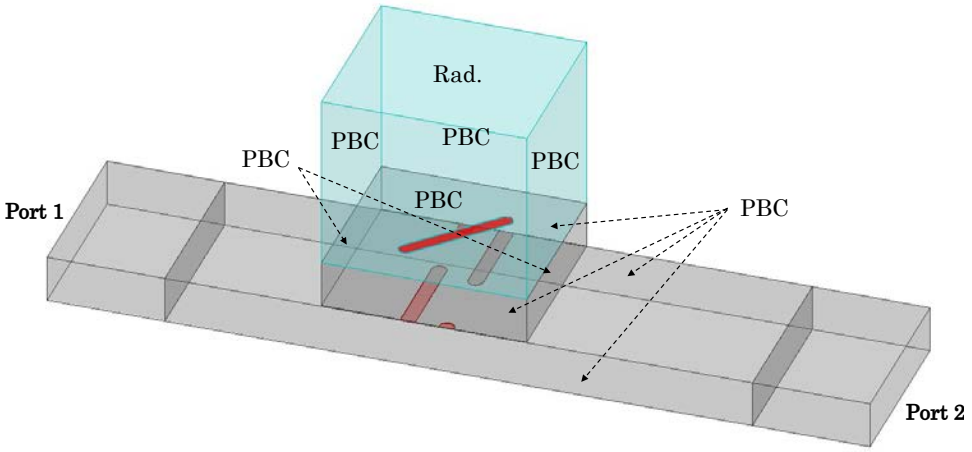

Figure 4.15: Analysis model for a radiating element

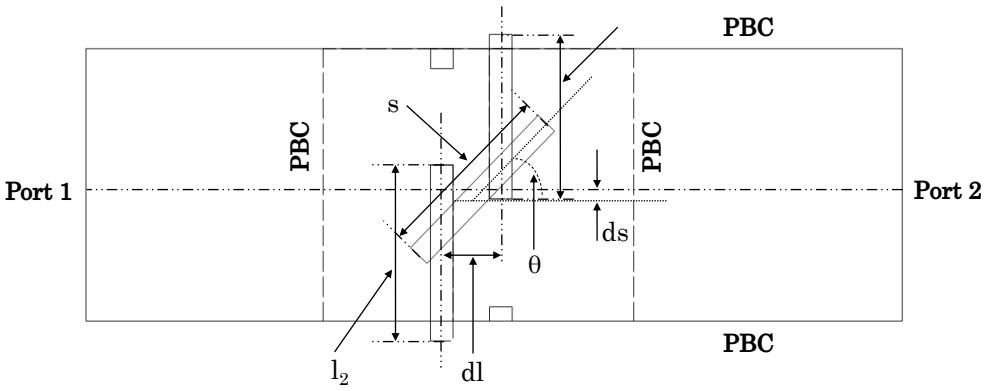

Figure 4.16: Design parameters of a radiating element

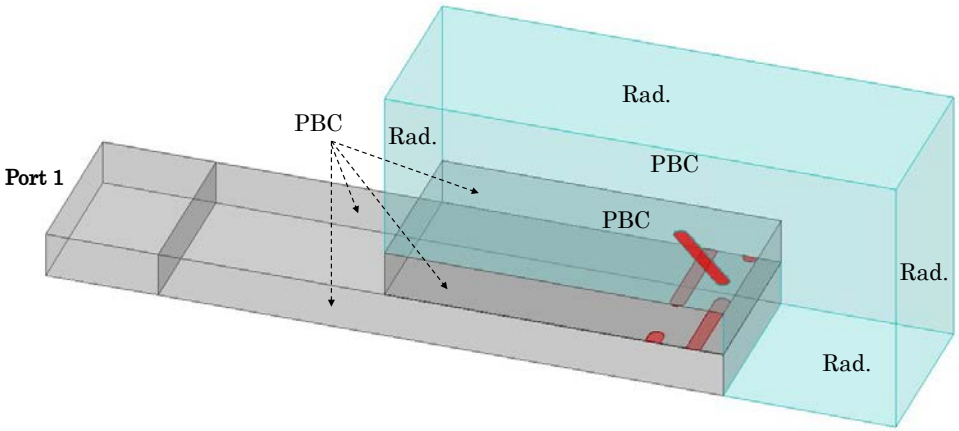

Figure 4.17: Analysis model for the matching slot

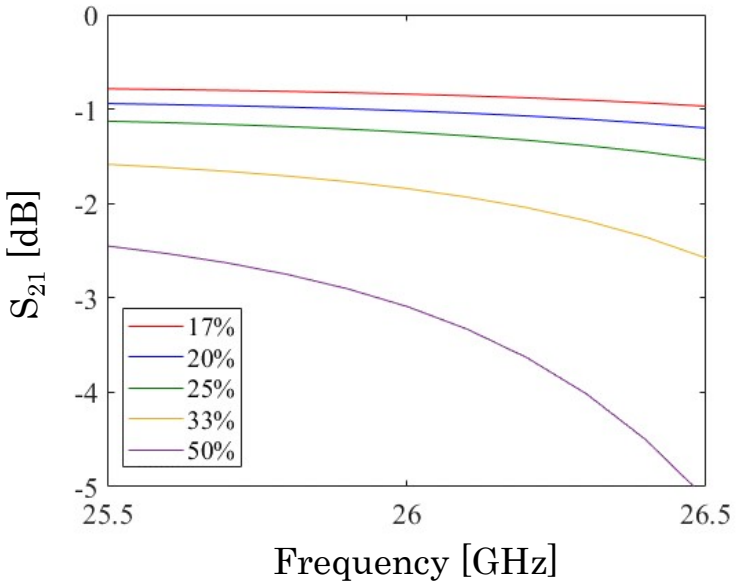

Figure 4.18: Plots of S_{21} showing the amount of coupling power of each radiating element

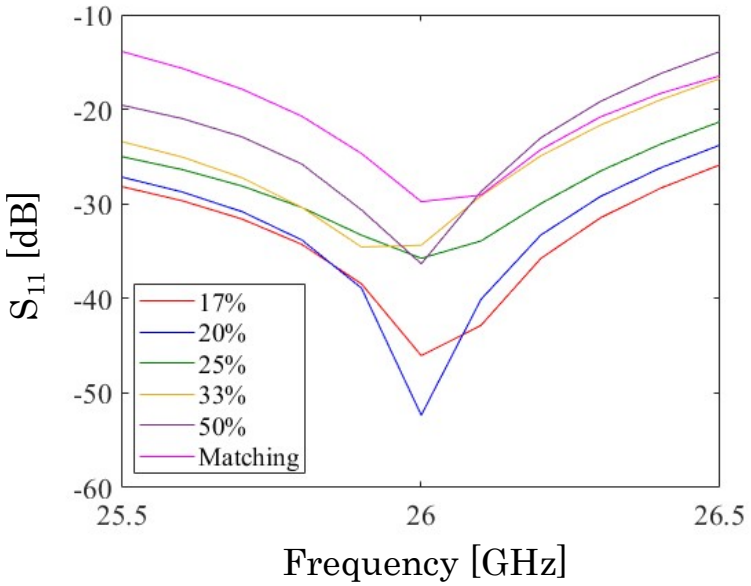

Figure 4.19: Plots of reflection of each radiating element

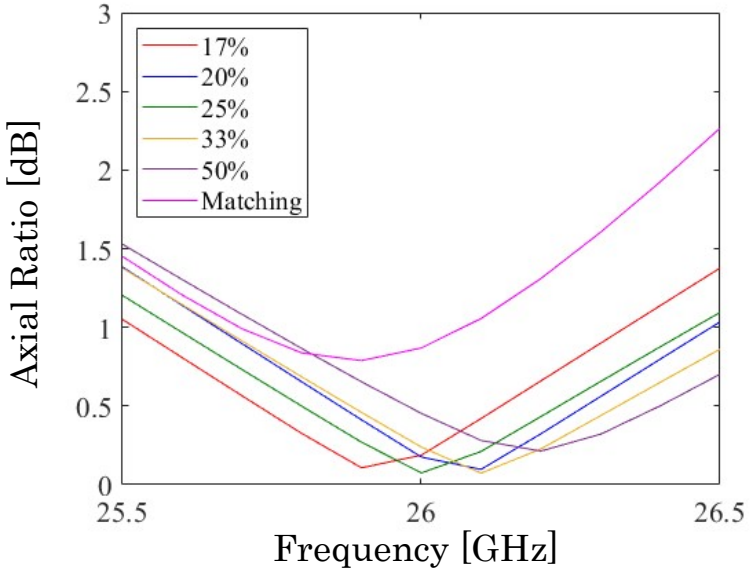

Figure 4.20: Plots of axial ratio of each radiating element

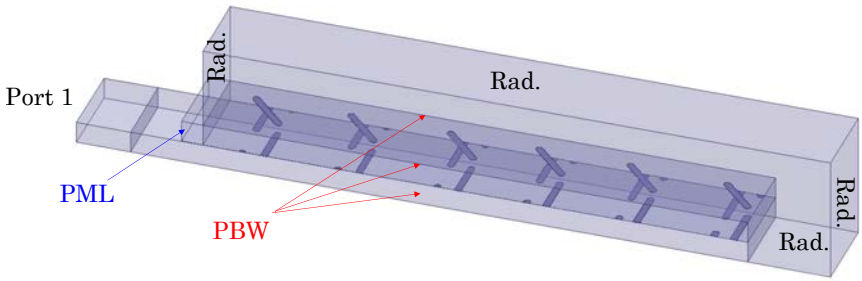

Figure 4.21: Analysis model for a one-dimensional array

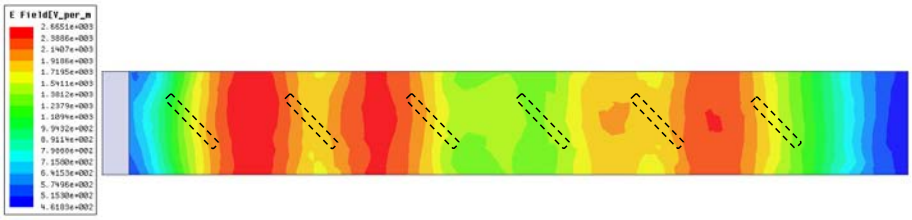

Figure 4.22: Field distribution over the one-dimensional array

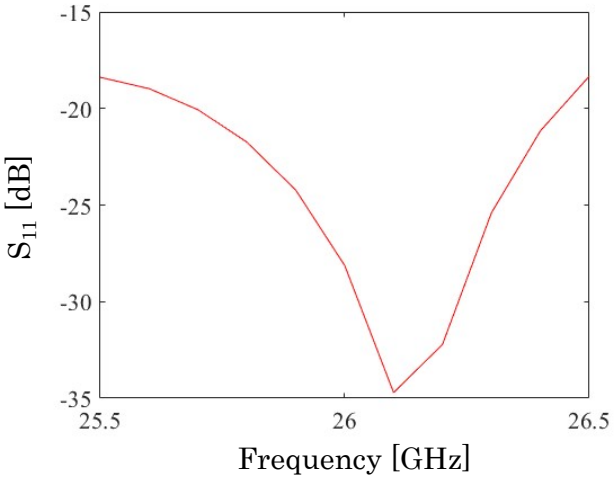

Figure 4.23: Plot of reflection of the one-dimension array

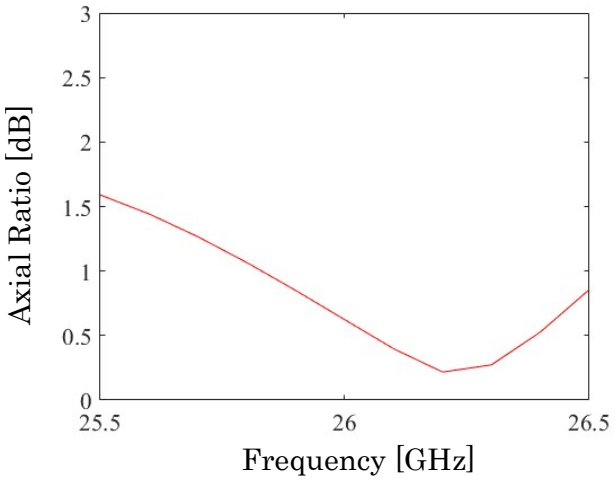

Figure 4.24: Plot of axial ratio of the one-dimension array

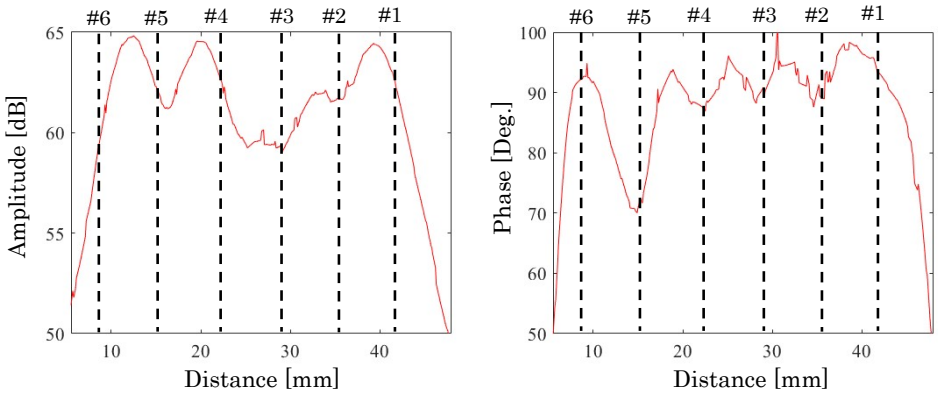

(a) RHCP

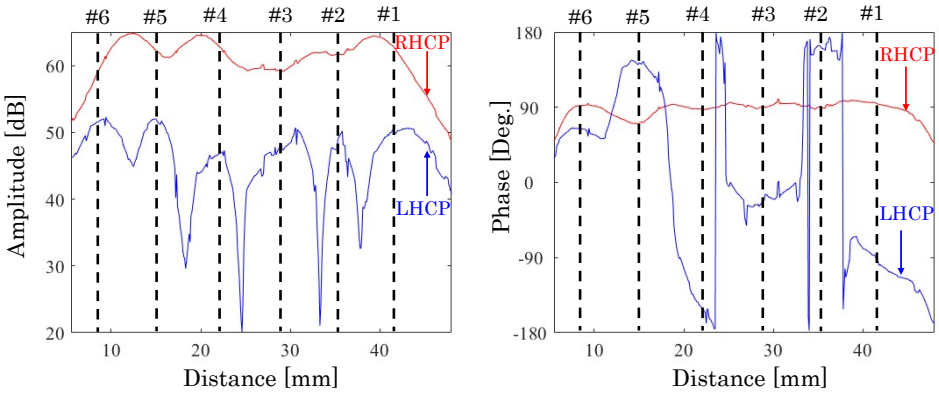

(b) RHCP & LHCP

Figure 4.25: Field distribution along the center of the radiating elements

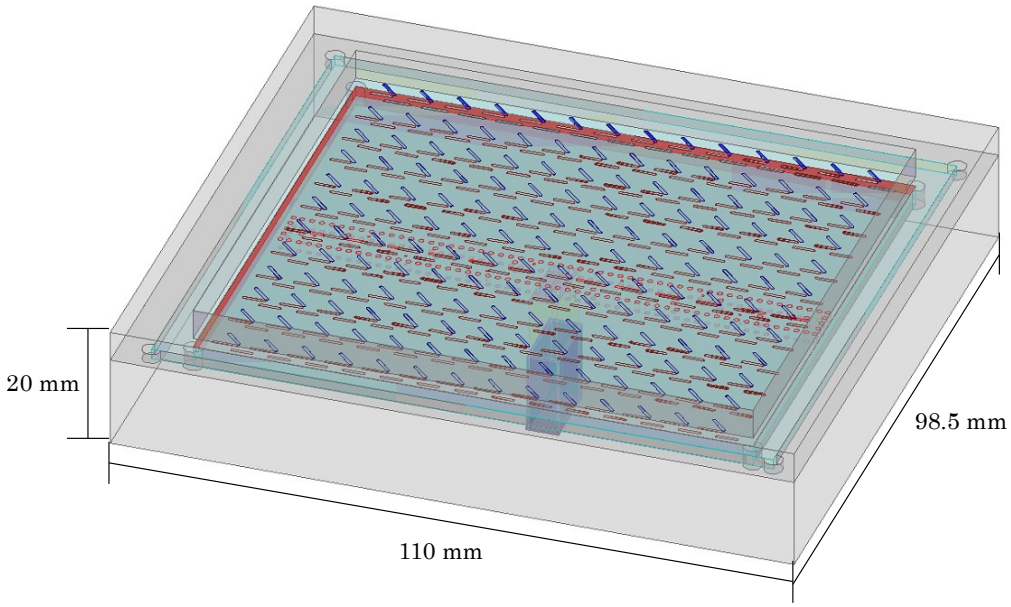

Figure 4.26: Complete antenna structure

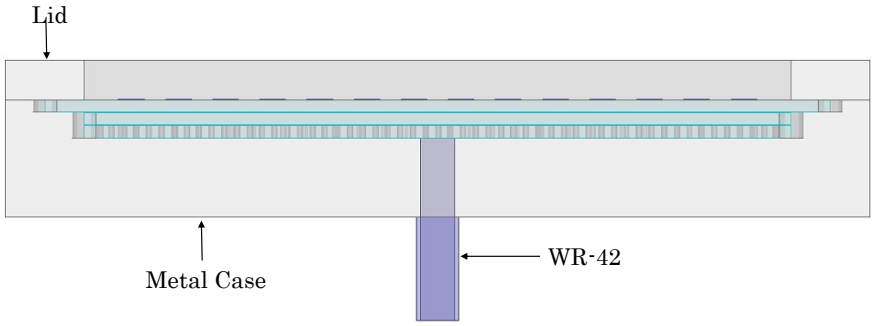

Figure 4.27: Font view of Fig.4.26

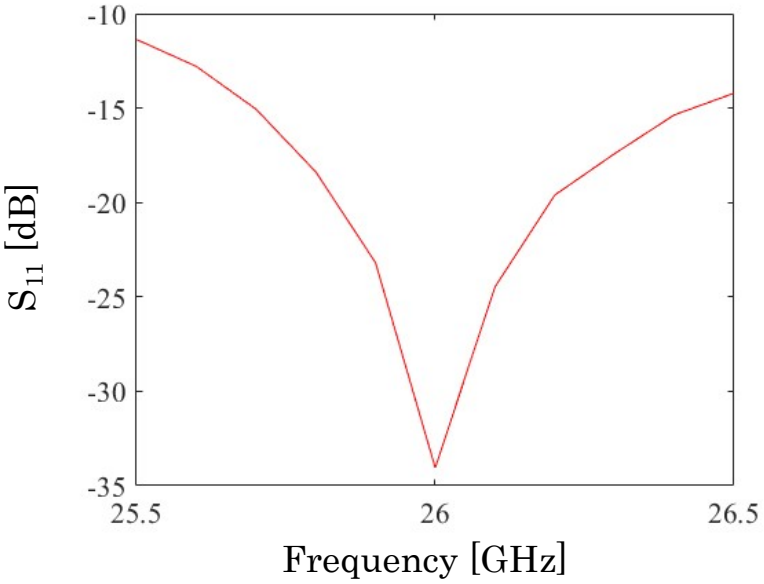

Figure 4.28: Plot of reflection of the full antenna model

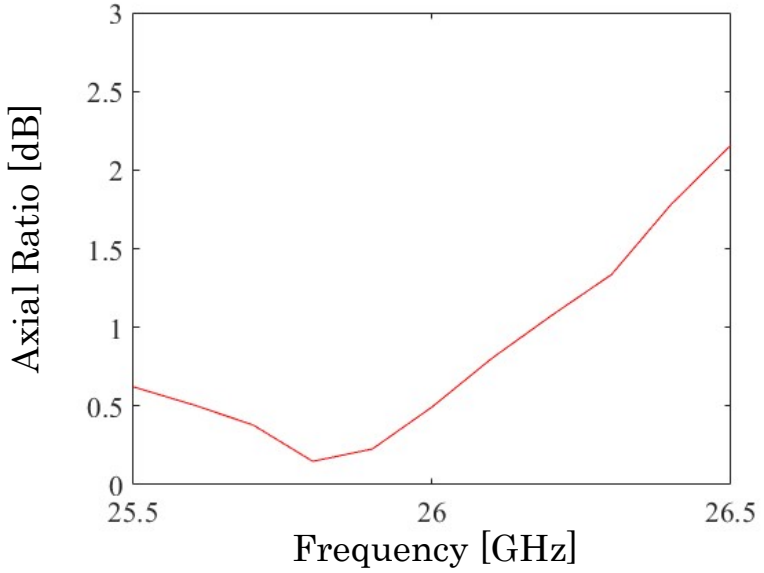

Figure 4.29: Plot of axial ratio of the full antenna model

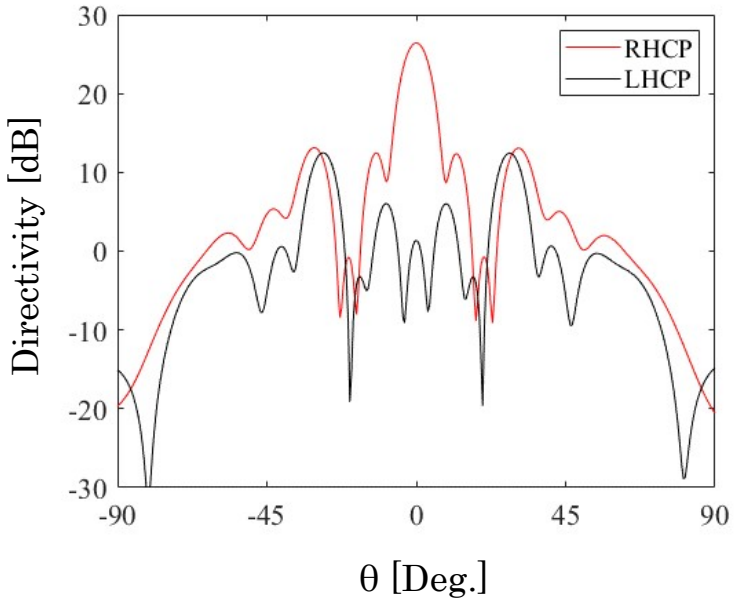

(a) $\phi = 0°$

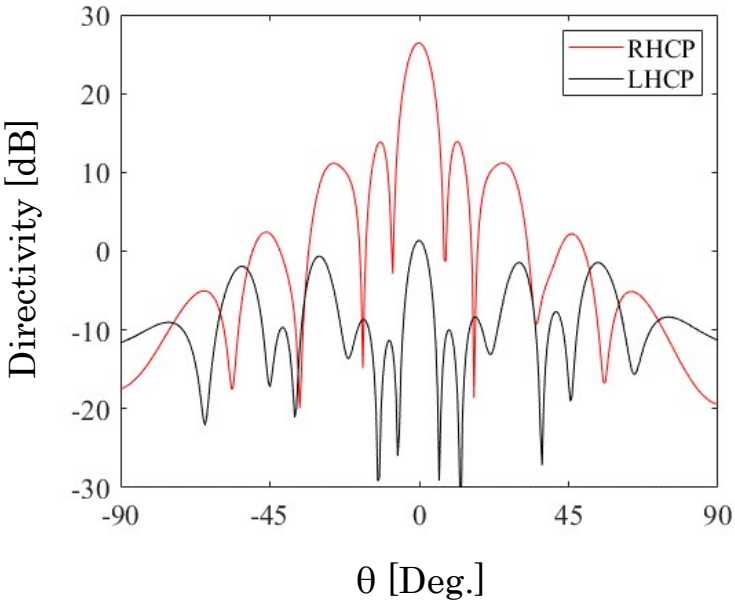

(b) $\phi = 90°$

Figure 4.30: Plots of directivity

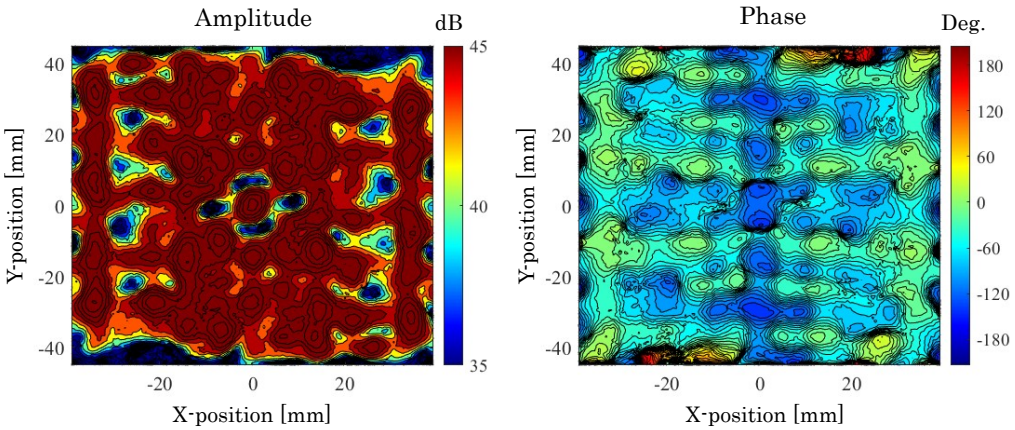

(a) RHCP

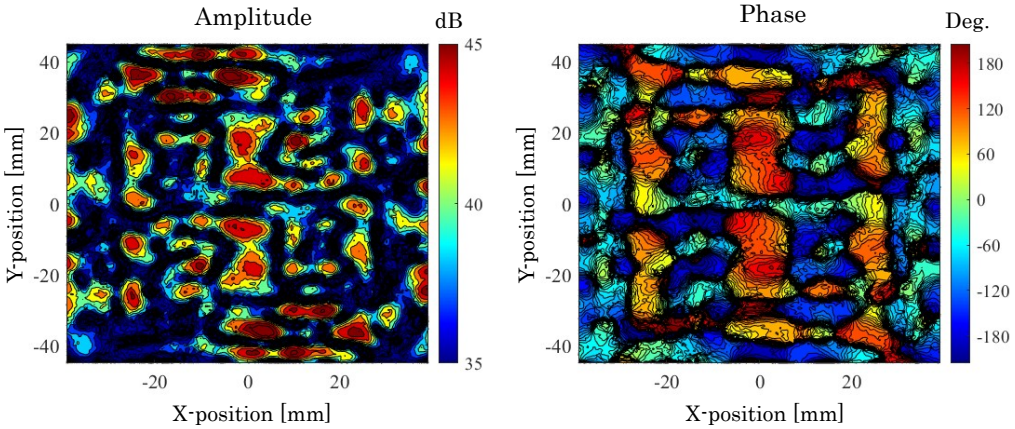

(b) LHCP

Figure 4.31: Aperture field distribution

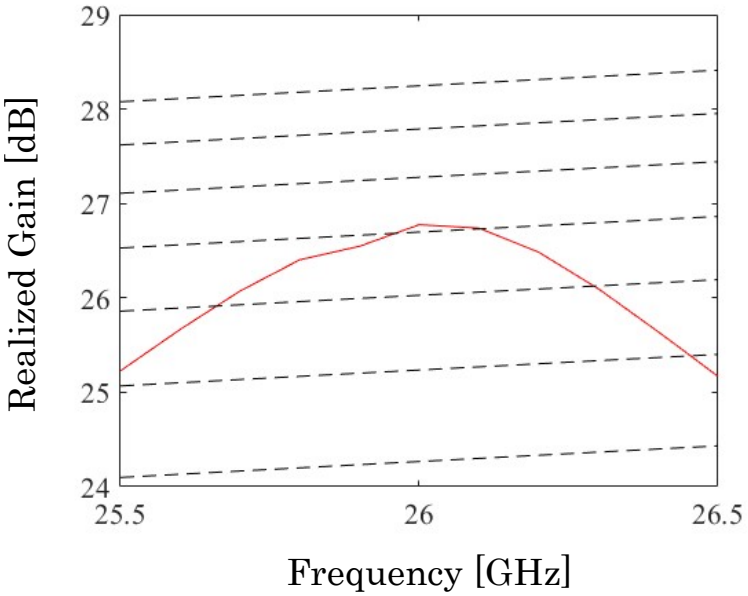

Figure 4.32: Plot of realized gain

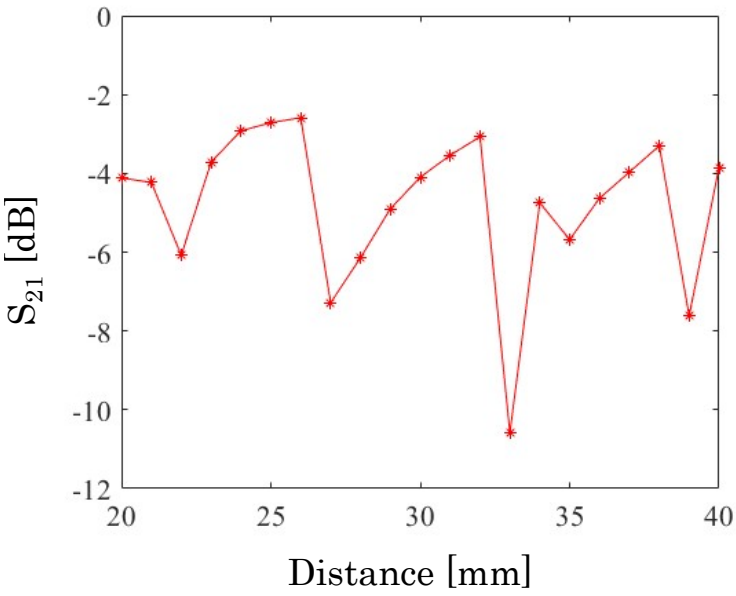

Figure 4.33: Transmission over the distances from 20 mm to 40 mm

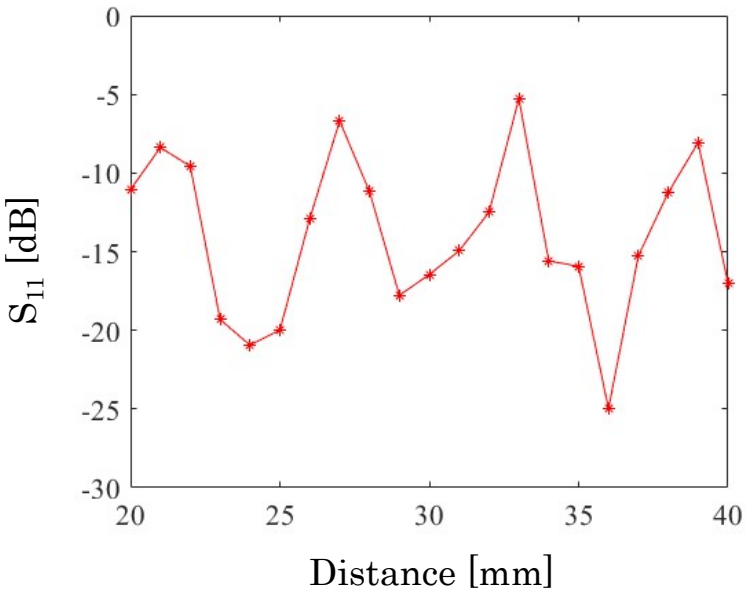

Figure 4.34: Reflection over the distances from 20 mm to 40 mm

References

[1] M. Ando, K. Sakurai, N. Goto, K. Arimura, and Y. Ito, "A radial line slot antenna for 12 ghz satellite tv reception," *IEEE Transactions on Antennas and Propagation*, vol. 13, no. 12, pp. 1347–1353, Dec. 1985.

[2] J. Hirokawa, M. Ando, and N. Goto, "Waveguide-fed parallel plate slot array antenna," *IEEE Transactions on Antennas and Propagation*, vol. 40, no. 2, pp. 218–223, Feb. 1992.

[3] K. S. Min, J. Hirokawa, K. Sakurai, M. Ando, and N. Goto, "Single-layer dipole array for linear-to-circular polarisation conversion of slotted waveguide array," *IEE Proceedings of Microwaves, Antennas and Propagation*, vol. 143, no. 3, pp. 211–216, Jun. 1996.

[4] T. Tomura, Y. Saito, and J. Hirokawa, "8 × 2-element 60-ghz-band circularly polarized post-wall waveguide slot array antenna loaded with dipoles," *IEEE Access*, vol. 8, pp. 85 950–85 957, May 2020.

[5] M. Wagih, G. S. Hilton, A. S. Weddell, and S. Beeby, "Millimeter wave power transmission for compact and large-area wearable iot devices based on a higher-order mode wearable antenna," *IEEE Internet of Things Journal*, Aug. 2021, early access.

[6] T. A. Khan, A. Alkhateeb, and R. W. Heath, "Millimeter wave energy harvesting," *IEEE Transactions on Wireless Communications*, vol. 15, no. 9, pp. 6048–6062, Sep. 2016.

[7] M. Tabesh, N. Dolatsha, A. Arbabian, and A. M. Niknejad, "A power-harvesting pad-less millimeter-sized radio," *IEEE Journal of Solid-State Circuits*, vol. 50, no. 4, pp. 962–977, Mar. 2015.

[8] A. Eid, J. Hester, and M. Tentzeris, "5g as a wireless power grid," *Scientific Reports*, vol. 11, no. 636, Jan. 2021.

[9] P. Pursula, T. Vaha-Heikkila, A. Muller, D. Neculoiu, G. Konstantinidis, A. Oja, and J. Tuovinen, "Millimeter-wave identification—a new short-range radio system for low-power high data-rate applications," *IEEE Transactions on Microwave Theory and Techniques*, vol. 56, no. 10, pp. 2221–2228, Sep. 2008.

[10] Y. Tomori, T. Wang, T. Tomura, and J. Hirokawa, "Design of a circularly polarized slot array on a parallel-plate waveguide fed by longitudinal coupling slots with posts," *International Symposium on Antennas and Propagation (ISAP)*, May 2020.

[11] T. Wang, T. Tomura, and J. Hirokawa, "Design of longitudinal coupling slots with matching walls for a rectangular parallel plate slot array antenna," *International Symposium on Antennas and Propagation (ISAP)*, Oct. 2019.

[12] P. R. Akbar, H. Saito, M. Zhang, J. Hirokawa, and M. Ando, "Parallel-plate slot array antenna for deployable sar antenna onboard small satellite," *IEEE Transactions on Antennas and Propagation*, vol. 64, no. 5, pp. 1661–1671, May 2016.

[13] J. Hirokawa and M. Ando, "Single-layer feed waveguide consisting of posts for plane tem wave excitation in parallel plates," *IEEE Transactions on Antennas and Propagation*, vol. 46, no. 5, pp. 625–630, May 1998.

[14] A. Collado and A. Georgiadis, "24 ghz substrate integrated waveguide (siw) rectenna for energy harvesting and wireless power transmission," *IEEE MTT-S International Microwave Symposium Digest (MTT)*, Jun. 2013.

[15] S. Ladan, A. B. Guntupalli, and K. Wu, "A high-efficiency 24 ghz rectenna development towards millimeter-wave energy harvesting and wireless power transmission," *IEEE Transactions on Circuits and Systems I*, vol. 61, no. 12, pp. 3358–3366, Dec. 2014.

Chapter 5

Conclusion

5.1 Summary of Preceding Chapters

Waveguide slot antennas have been adopted in both data communication and power transmission applications owing to their several advantages of low-loss, slimness, and high-power capability. The objective of this study is to investigate the design of waveguide slot array antenna and propagation in their corresponding non-far region applications.

Chapter 1 presents the importance of waveguide slot antenna and their common features employed in various application in the non-far region.

Chapter 2 discusses the ISI issue in a compact-range communication system using large array antennas. The following summarizes the gist of this chapter

- The main cause of ISI in a compact-range communication system using large array antennas [1] comes from the differences in propagating paths of each transmitted signal especially in large size antennas.

- A method to quantitatively evaluate ISI was proposed since the calculation using commercially available electromagnetic simulator software is often limited by the size of computer memories especially in the case of high frequency and large object simulation. The idea of the proposed method is to utilize the measured aperture near-field distribution of actual antennas which includes imperfections in the fabricated antenna, those which are difficult to account for in the simulation model. The calculation time of our proposed method is greatly determined by the

measurement time of the near-field distribution of the concerning antenna. The reliability of the estimated result was confirmed with the result obtained by direct measurement. The discrepancy between the estimated and measured ISI results is less than 3 dB for distances below 1 m and less than 5 dB for distances over 1 m.

- Our findings suggest that ISI becomes significant for the large array size and at the distances close to the array. In addition, the ideally uniform excitation gives the smallest value of ISI.

- The proposed method can be applied to different types of antennas as long as the antenna aperture distribution is obtained.

Chapter 3 presents a design method to enhance the transmission between RLSAs proposed in [2]. The following summarizes the gist of this chapter:

- We can enhance the transmission by improving the uniformity in the aperture field excitation. This could be done by a coupling slot with a better rotating mode.

- The dog-bone cross-slot was adopted and designed using the eigenmode analysis. A better rotating mode of the dog-bone cross-slot in comparison to the straight cross-slot was confirmed by simulation.

- The improvement on the transmission using the dog-bone cross-slot fed RLSA was confirmed by both simulation and measurement. The improvement on the transmission for RLSAs using the design dog-bone cross-slot were confirmed by simulation and experiment. The simulation over 50-100 mm. distances suggests 66% transmission efficiency and 2 dB reduction in transmission ripples compared to that of the straight cross-slot case, while the measurement over the same range suggests 61% transmission efficiency which is 15% higher than that of the RLSA using the straight cross-slot feeding and 1.5 dB reduction in transmission ripples.

- The discrepancies between the simulation and measurement results caused by the fabrication error at the inner conductor of the coaxial feeder was implied.

- Differences in the transmission using RLSA fed the dog-bone cross-slot and that using the straight cross-slot fed RLSA becomes small at larger transmission distances owing to the beam divergence.

Chapter 4 focuses on the design of a parallel-plate slot array antenna with circular polarization, a candidate for short-distance wireless power transmission and wireless communication. The following summarizes the gist of this chapter:

- A single mode waveguide array with inductive and capacitive posts was designed for the feeding parts and the radiating slot pairs with dipoles for polarization conversion was designed for the feeding part.
- Simulation indicates that the design antenna has reflection below -30 dB, axial ratio below 1 dB, gain of 26.50 dBi, and 70% antenna efficiency.
- Comparison with the RLSAs in chapter 3 is currently difficult due to the operating frequency.

To this end, antenna performances in non-far region application are more susceptible to design or fabrication error than that in far-field region because electromagnetic field variance is likely to be significant. Hence when one designs an antenna for near-field applications, it would require more attention to the antenna excitation and its sensitivity to the design error. Besides, multiple reflections often becomes a problem especially in near-field application.

5.2 Remarks for Future Studies

There are some considerations in which this study did not account for. The following are some thoughts on these which could lead to future improvements.

Chapter 2 suggests that the lowest level of ISI for the current system could be realized by using antennas with the ideally uniform excitation. However possibilities that other excitation schemes, e.g., Gaussian distribution, could lead to a better ISI performance would be interesting for further investigation. A trade-off between the antenna design and ISI as well as other system requirements should be considered whether it is worth actualizing. Another

point is that we assume in the study that the receiving terminal is a receiving probe. A practical receiving terminal, e.g., cellular phone, possesses a different receiving characteristics, but more importantly it is equipped with several signal processing components such as an automatic gain control (AGC), a low-density parity-check (LDPC) code, and etc. Therefore, more accurate ISI estimation is to include the effects of those signal processing components and some modifications to the method are necessary. In addition, if ISI under the presence of actual system components can be estimated, it would allow the reproduction and accurate estimation of BER performance which is the ultimate target of the study. Finally, a more practical and straightforward approach to deal with the ISI issue is to rely on signal processing such as an equalizer.

Chapter 3 addresses mainly the design of the Tx antenna. In an actual microwave power transmission, a major limitation to the overall efficiency is a rectanna [3]. This implies that not only the antenna design but also the RF-to-dc conversion circuit should be carefully considered. In addition, the current antenna design is applicable to the transmission distances below 2. The array size needs to be modified for a longer target distance and higher transmission efficiency.

Chapter 4 presents the design of a parallel plate waveguide array antenna for applications in near-field region. We intended to fabricate the antenna at 5.8 GHz. However, due to the fabrication limitations we have to design it at 26 GHz. The antenna has a gain of 26 dBi and approximately 1 GHz bandwidth which has the potential for both short-distance wireless communication and WPT applications. However, the simulated transmission indicates significant degradation at a distance of 33 mm. The current transmission result could not meet the required accuracy because of the memory capacity of our computer. Therefore we need to apply meshing techniques and verify any change in the result. In addition, a prototype antenna will be fabricated to verify its actual performance. Another consideration is the antenna coverage. The current design approach is expected to be applicable to lower frequencies in microwave bands and depending on the application requirements the antenna should be properly modified similar to that in chapter 3. It is however unfortunate that the antenna cannot be fabricated at 5.8 GHz due to fabrication limitations. One of our future studies would be modifications to the current design that could allow antenna fabrication at 5.8 GHz.

References

[1] M. Zhang, K. Toyosaki, J. Hirokawa, M. Ando, T. Taniguchi, and M. Noda, "A 60 ghz-band compact-range gigabit wireless access system using large array antennas," *IEEE Transactions on Antennas and Propagation*, vol. 63, no. 8, pp. 3423–3440, Aug. 2015.

[2] T. Tomura, J. Hirokawa, M. Furukawa, and T. Fujiwara, "Radial line slot array antenna for 5.8-ghz band beam-type wireless power transmission," *IEICE Technical Report*, vol. 119, no. 295, pp. 87–90, Nov. 2019.

[3] W. C. Brown, "The history of wireless power transmission," *Solar Energy*, vol. 56, no. 1, pp. 3–21, Jan. 1996.

[4] P. D. H. Re, S. K. Podilchak, S. A. Rotenberg, G. Goussetis, and J. Lee, "Circularly polarized retrodirective antenna array for wireless power transmission," *IEEE Transactions on Antennas and Propagation*, vol. 68, no. 4, pp. 2743–2752, Apr. 2020.

[5] T. Ruckkwaen, T. Tomura, K. Araki, J. Hirokawa, and M. Ando, "Experimental evaluation of intersymbol interference in non-far region transmission using a large array antenna in millimeter-wave band," *IEICE Transactions on Communications*, vol. E103-B, no. 10, pp. 1136–1146, Oct. 2020.

[6] T. Ruckkwaen, T. Tomura, and J. Hirokawa, "Short-range transmission improvement by dog-bone cross-slot feed in radial line slot antenna," *IEICE Communications Express*, To be published in Jun. 2022.

List of Publications

Journals

[1] T. Ruckkwaen, T. Tomura, K. Araki, J. Hirokawa, and M. Ando, "Experimental evaluation of intersymbol interference in non-far region transmission using a large array antenna in millimeter-wave band," *IEICE Transactions on Communications*, vol. E103-B, no. 10, pp. 1136–1146, Oct. 2020.

[2] T. Ruckkwaen, T. Tomura, and J. Hirokawa, "Short-range transmission improvement by dog-bone cross-slot feed in radial line slot antenna," *IEICE Communications Express*, To be published in Jun. 2022.

International Conferences

[3] T. Ruckkwaen, T. Tomura, and J. Hirokawa, "Transmission enhancement for radial line slot antennas in non-far region using a feeding slot with better rotating mode," *International Symposium on Antennas and Propagation (ISAP)*, 3C1, Jan. 2020.

[4] ——, "Short-distance transmission enhancement by baffles for a slot pair on parallel plate waveguide," *IEEE International Symposium on Antennas and Propagation and USNC-URSI Radio Science Meeting (APS/URSI)*, TUP-UB.1P, Jul. 2020.

[5] T. Ruckkwaen, K. Araki, T. Tomura, J. Hirokawa, and M. Ando, "Experimental evaluation of intersymbol interference in non-far region transmission using 30-ghz band large array antennas," *IEEE International Symposium on Antennas and Propagation and USNC-URSI Radio Science Meeting (APS/URSI)*, TU-UB.1P.9, Jul. 2019.

[6] ——, "Evaluation of intersymbol interference in non-far region transmission using 60 ghz-band large array antennas," *International Symposium on Antennas and Propagation (ISAP)*, WeP-12, Oct. 2018.

[7] T. Ruckkwaen, M. Ando, T. Tomura, J. Hirokawa, and M. Ali, "Evaluation of field strength distribution by modified edge representation (mer) in compact range communication with shadowing objects," *International Symposium on Antennas and Propagation (ISAP)*, Oct. 2017.

Domestic Conferences

[8] T. Ruckkwaen, T. Tomura, and J. Hirokawa, "Transmission stability on distance in the near-field region in 5.8 ghz band radial line slot antennas using a dog-bone cross-slot feed," *IEICE General Conference*, B-1-61, Mar. 2021.

[9] ——, "The effect of rotational dependence on transmission characteristics of radial line slotted array antennas," *IEICE Society Conference*, B-1-96, Sep. 2020.

[10] ——, "Transmission enhancement by using baffles for slot pair on parallel plate waveguide," *IEICE General Conference*, B-1-74, Mar. 2020.

[11] T. Ruckkwaen, K. Araki, T. Tomura, J. Hirokawa, and M. Ando, "Experimental evaluation of intersymbol interference in non-far region transmission using 60-ghz band large array antennas," *IEICE Society Conference*, B-1-125, Sep. 2018.

[12] T. Ruckkwaen, K. Toyosaki, M. Zhang, K. Araki, J. Hirokawa, and M. Ando, "Mechanism extraction of bit error rate distribution in compact range communication," *IEICE General Conference*, Mar. 2017.